ADVANCED SHIP DETECTION METHODS IN SYNTHETIC APERTURE RADAR IMAGERY

by

Colin Peter Schwegmann

Submitted in partial fulfillment of the requirements for the degree
Philosophiae Doctor (Computer Engineering)

in the

Department of Electrical, Electronic and Computer Engineering
Faculty of Engineering, Built Environment and Information Technology

UNIVERSITY OF PRETORIA

Feb 2018

SUMMARY

ADVANCED SHIP DETECTION METHODS IN SYNTHETIC APERTURE RADAR IMAGERY

by

Colin Peter Schwegmann

Promoter(s):	Dr. W. Kleynhans and Dr. B. P. Salmon
Department:	Electrical, Electronic and Computer Engineering
University:	University of Pretoria
Degree:	Philosophiae Doctor (Computer Engineering)
Keywords:	SAR, Image processing, Pattern recognition, Marine technology

Large area monitoring plays an important role in the Maritime Domain Awareness initiative. To effectively monitor long coastlines and further out at sea, a multitude of monitoring techniques are necessary. One of these techniques, satellite Synthetic Aperture Radar (SAR), can monitor large areas independent of weather or time of day. SAR imagery is particularly useful in the tracking of ships at sea as ships are highly reflective objects and become visible against the dark ocean background. This allows SAR to supplement traditional ship tracking methods such as transponder-based systems as it requires no cooperation to track the ships.

SAR ship detection research is typically focused on high resolution, smaller width imagery. While this imagery is an effective way to detect ships and monitor smaller areas such as single harbors, high resolution SAR imagery cannot provide the necessary coverage to monitor large areas such as national Exclusive Economic Zones (EEZ). Large swath imagery can provide this coverage but comes with reduced resolution which in turn limits the minimum detectable ship size. Current methods applied to high resolution SAR imagery do not necessarily translate well to low-to-medium resolution SAR imagery and so new methods need to be developed to help improve detection performance on these types of imagery.

Two novel SAR ship detection techniques are proposed, both of which are tested against a newly created 46 image, medium resolution SAR imagery dataset. The dataset covers approximately 80% of South Africa's Exclusive Economic Zone using two sensors (Sentinel-1 and RADARSAT-2), three resolutions and four polarizations. The first method extends the conventional Constant False Alarm Rate prescreening method to allow per-pixel thresholding so thresholds can be adjusted for specific areas. The method makes further use of Simulated Annealing to help identify areas of probable ships using an auxiliary transponder dataset. This technique improves the flexibility of previous Constant False Alarm Rate-based methods and provides a mean detection accuracy of 87.51%, a mean False Alarm Rate (FAR) of 5.644×10^{-8} and mean Matthews Correlation Coefficient (MCC) of 0.80. The second method uses unique ship-like, rapidly calculable features known as Haar-like features to describe ships. These features are used to train a cascaded classifier to create a ship discrimination step. The combination of these aspects and an advanced training technique known as AdaBoost creates a method which can be efficiently applied to medium resolution SAR imagery to provide significant false alarm reduction whilst maintaining a high ship detection accuracy which provides the best results of the methods investigated with a mean detection accuracy of 88.71%, mean FAR of 1.940×10^{-8} and a MCC of 0.89. These two methods are evaluated against a range of other ship detection methods using various standardized metrics and multiple test scenarios. Finally, the thesis concludes with an in-depth discussion of the novel methods' advantages and disadvantages and what possible future areas of research may be.

Acknowledgements

To my supervisor and mentor Dr. **Waldo Kleynhans**: Thank you from the bottom of my heart for your guidance throughout this thesis. I could not have done it without you. And thank you for always being the exemplary leader I strive to be one day.

To my co-supervisor, Dr. **Brian Salmon**: I am eternally grateful for your valuable insight into so many topics during this thesis and beyond. I am lucky to have someone who I could wholly rely on to bounce ideas off of.

To my parents **Eugene and Liesl**: Thank you for always supporting me through my studies and life. I could not have asked for better parents or people to be examples.

To my siblings, **Nicole, Lauren, Alicia and Ruan**: You are the reason I never gave up and this thesis is finished because you believed in me.

To all my other **friends and family**: Thanks for sticking around through my crazy absenteeism, my constant moaning and groaning about having to write some more and for being the incredible people you all are.

And finally, to my **Mom and Gran**: I miss you every day and I wish you were here to see what I've done while you've been gone. I know you would both be proud.

"The mind is a labyrinth, ladies and gentlemen, a puzzle. And while the paths of the brain are plainly visible, its ways deceptively apparent, its destinations are unknown. Its secrets still secret. And, if we are honest, it is the lure of the labyrinth that draws us to our chosen field to unlock those secrets. Others have been here before us and have left us signs, but we, as explorers of the mind, must devote our lives and energies to going further to tread the unknown corridors in order to find ultimately, the final solution. We have to see, we have to know...."

Dr. Philip Channard

LIST OF ABBREVIATIONS

AdaBoost	Adaptive Boosting
AIS	Automatic Identification System
ALOS	Advanced Land Observing Satellite
AUC	Area Under Curve
CA-CFAR	Cell-Averaging CFAR
CA-CFAR NF	CA-CFAR Non-flat
CA-CFAR SA	CA-CFAR Simulated Annealing
CFAR	Constant False Alarm Rate
CHAAR	CA-CFAR Haar-like Cascade Classifier
COSMO-SkyMED	Constellation of Small Satellites for Mediterranean basin Observation
DA	Detection Accuracy
DInSAR	Differential Interferometric SAR
EEZ	Exclusive Economic Zone
EM	Electromagnetic
ENVISAT	Environmental Satellite
ERS	European Remote-Sensing
ESA	European Space Agency
EW	Extra Wide
FAR	False Alarm Rate
FN	False Negative
FP	False Positive
GA	Genetic Algorithm
GCP	Ground Control Point
GDAL	Geospatial Data Abstraction Library
GeoTIFF	Georeferenced Tagged Image File Format
GO-CFAR	Greatest-Of CFAR
GPS	Global Positioning System
GRD	Ground Range Detected
GRDH	Ground Range Detected High
GRDM	Ground Range Detected Medium

GS-CFAR	Generalized Switching CFAR
HAAR	Haar-like Cascade Classifier
IMO	International Maritime Organization
InSAR	Interferometric SAR
ITU	International Telecommunication Union
IUU	Illegal, Unreported and Unregulated fishing
IW	Interferometric Wide
KDE	Kernel Density Estimation
LiDAR	Light Detection And Ranging
LOS	Line of Sight
LRIT	Long Range Identification and Tracking
LUT	Look Up Table
MAP	Maximum A Posteriori
MCC	Matthews Correlation Coefficient
MDA	Maritime Domain Awareness
MMU	Minimum Mappable Unit
MMSE	Minimum Mean Squared Error
MMSI	Maritime Mobile Service Identity
MODIS	Moderate Resolution Imaging Spectroradiometer
MVEE	Minimum Volume Enclosing Ellipse
NN	Neural Network
OS-CFAR	Order-Statistic CFAR
PALSAR	Phased Array type L-band SAR
PCA	Principal Component Analysis
PDF	Probability Density Function
PFA	Probability of False Alarm
PR	Power Ratio
PSO	Particle Swarm Optimization
RADAR	Radio Detection and Ranging
RADARSAT	RADAR Satellite
RCM	RADARSAT Constellation Mission
RCS	RADAR Cross Section
ROC	Receiver Operating Characteristic

ROI	Region Of Interest
SA	Simulated Annealing
SAR	Synthetic Aperture Radar
Sat-AIS	Satellite AIS
SCNA	ScanSAR Narrow Band-A
SeaSAT	Sea Satellite
SLC	Single Look Complex
SNR	Signal to Noise Ratio
SO-CFAR	Smallest-Of CFAR
SVD	Singular Value Decomposition
SVM	Support Vector Machine
SWOS-CFAR	Switched Order-Statistic CFAR
TDMA	Time-division multiple access
TN	True Negative
TP	True Positive
VHF	Very High Frequency
VIIRS	Visible Infrared Imaging Radiometer Suite
VMS	Vessel Monitoring System
XML	Extensible Markup Language

TABLE OF CONTENTS

CHAPTER 6 DATASET DESCRIPTION . . . 87

CHAPTER 7 RESULTS AND DISCUSSION . . . 107

CHAPTER 1 INTRODUCTION

1.1 PROBLEM STATEMENT

1.1.1 Context of the problem

Maritime Domain Awareness (MDA) involves the generation of actionable intelligence for any maritime related activities [1]. Monitoring such activities is necessary for each sea-bordering country but is infeasible to do so at a global scale. MDA is therefore an initiative seeking to facilitate collaborations among countries to improve all stakeholders maritime awareness.

A major component of MDA is the understanding and policing of each country's own Exclusive Economic Zone (EEZ). The EEZ is an area of water that extends approximately 370 kilometers from the coast and each sea-bordering country is required to police its EEZ. South Africa's land mass covers approximately 1.2 million square kilometers whereas its EEZ covers more than 1.5 million square kilometers. Due to both its size and unique positioning between two oceans, improvement of South Africa's MDA is an important long term goal for the country.

One of the ways in which an EEZ can be monitored is by using remote sensing techniques. These techniques are provided by two main platforms - airborne and spaceborne. Airborne remote sensing can provide very high resolution acquisitions with short revisit times but only over a limited geographical area. Alternatively, spaceborne remote sensing can monitor very large areas at reduced resolutions at a significantly lower cost per square kilometer than airborne methods. Large areas, such as South Africa's EEZ, could not be monitored regularly using airborne remote sensing techniques whereas spaceborne remote sensing techniques could map this same area within days.

Airborne and spaceborne remote sensing can be supplemented by in-situ measurements to provide the best overall view of the maritime domain. A number of remote sensing sensors are available spanning the entire electromagnetic (EM) spectrum [2] aboard both airborne and spaceborne platforms. Sensors can be passive such as optical or multi-/hyper-spectral sensors or active such as Synthetic Aperture Radar (SAR) or Light Detection and Ranging (LiDAR) sensors. Passive sensors typically rely on sunlight to illuminate the area to be observed whereas active sensors use their own form of EM illumination. Active sensors can therefore be used independent of the time of day. Furthermore, SAR uses specific bands of the EM spectrum which, under most circumstances, do not interact with weather conditions making it an ideal candidate to monitor large areas consistently.

SAR imaging works by measuring the power returned from objects as well as the time it takes to receive a transmitted signal thereby determining distance due to the fixed speed of EM waves (at the speed of light). Objects that are highly reflective will provide a higher amount of return backscatter which allows the discrimination of highly reflective targets such as ships from those with lower backscatter values such as the sea.

The detection of ships within SAR imagery is an open research topic. With the recent influx of free SAR imagery from the European Space Agency's (ESA) Sentinel-1 satellite access to the newest SAR imagery has become a viable means of monitoring large areas. This study aims to develop new methods for ship detection on the newest SAR imagery with a focus on South Africa's coast for improving its MDA. In addition to this the study also aims to develop a deeper understanding of the methods, their parameters and the metrics used to determine performance of ship detectors.

1.1.2 Research gap

Through the literature investigation of this study three main research gaps were identified.

Initial sample selection (ship prescreening) is currently limited by the usage of a single threshold at which entire scenes are processed. Due to their varying nature, SAR imagery is often processed with adaptive threshold methods. This quality should be investigated to identify if more advanced adaptive methods could improve ship detection performance within SAR imagery.

False alarm removal or ship discrimination for low-to-medium resolution SAR imagery has clearly defined limits, in particular with the usage of machine learning for discrimination tasks. Most studies currently focus on high resolution SAR imagery where ships occupy hundreds of pixels. While high resolution SAR imagery is useful to help identify ship classes the initial ship detection task is more simple due to these large ship sizes. Reducing the resolution provides unique challenges and preliminary literature research has identified this as a potential area for additional research into methods that can improve performance despite these limitations. Furthermore, identification of ships over a large area in low-to-medium resolution SAR imagery can guide tasking of higher resolution imagery over a specific area.

The field of SAR ship detection currently lacks a single, accessible dataset that covers multiple sensors, acquisition modes and resolutions. Method comparisons across studies are difficult due to different processing setups (preprocessing, prescreening and discrimination) and datasets that are often unique on a per-study basis. Research has also revealed a lack of coherent and precise descriptions of ship detection performance metrics across studies, further blurring possible comparisons between current and future methods from different authors.

1.2 RESEARCH OBJECTIVE AND QUESTIONS

Recent SAR ship detection has largely focused on the detection of ships at sea in high resolution SAR data. The objectives of this study include the determining of gaps in current literature focused on medium-to-low resolution SAR imagery and the development of new methods to improve on these gaps. Another important topic is the analysis of errors and the metrics by which these are measured. Performance metrics need to be selected that effectively highlight ship detection methods in a meaningful manner, across different datasets and acquisition conditions but also across a multi-sensor dataset which are now more readily acquired. The research conducted here will evaluate the proposed methods in a scientific and reproducible manner in order to select methods that might work best in a general, operational setting.

These lead to the following research questions to be answered in this study:

- What current ship detection method shortcomings can be exploited to improve overall ship detection in medium resolution SAR imagery?
- Can operational ship detection be accomplished by utilizing machine learning and related methods?
- Are the current performance metrics used for ship detection results sufficient to underline performance differences between methods in a meaningful manner across different datasets?

1.3 HYPOTHESIS AND APPROACH

The hypothesis of this study is that current ship detection performance can be improved by applying new image processing and machine intelligence algorithms to SAR imagery. Furthermore, proper performance metric standards are necessary to improve comparisons between methods, especially when used on a large varying dataset.

The study is to be conducted by acquiring SAR imagery and testing current methods followed by proposing new methods in a scientific and reproducible manner. A thorough investigation into the current state-of-the-art algorithms, how they compare to the novel methods presented here and the advantages and disadvantages of the methods presented will also be discussed. The methods will be tested against one another using reproducible and precise metrics. The results and a discussion thereof will be compiled into the thesis as the final objective of this study.

1.4 RESEARCH GOALS AND CONTRIBUTIONS

The research goals of this thesis is to provide a stringent study on the various methods of ship detection in SAR imagery by improving the research connection between remote sensing and machine learning. The thesis will aim to identify the various methods advantages and disadvantages against a systematically created SAR ship dataset and utilize additional MDA transponder data.

The research was expected to generate two published journal articles to remote sensing journals. The first, “Manifold Adaptation for Constant False Alarm Rate Ship Detection in South African

Oceans" will present an extension to a conventional ship detection prescreening algorithm and combine additional sources of data to improve the detection capabilities of current ship detection methods in medium resolution SAR imagery [3]. The second, "Synthetic Aperture Radar Ship Detection Using Haar-Like Features" describes a framework for detecting ships using unique ship-like machine learning features extracted from SAR imagery, trained and classified using advanced machine learning techniques to provide state-of-the-art ship discrimination [4]. In addition to the above, the study was also expected to generate a number of internationally accepted conference papers to identify relevant areas of research including the usage of object saliency [5], H-dome transformations [6] and Gabor wavelet extraction [7] for SAR ship detection. These contributions aim to add to the remote sensing, SAR and machine intelligence research body of knowledge while highlighting the necessity of research into these topics in a South African context.

1.5 OVERVIEW OF STUDY

This study is composed of seven chapters: Chapter 2 provides an introduction and literature review of MDA and ship transponders and where remote sensing is used in the context of MDA. Chapter 3 present an introduction into SAR with a focus on SAR for MDA applications. Chapter 4 provides the literature review of ship detection at the present whilst Chapter 5 introduces two novel ship detection techniques aimed to overcome shortcomings identified in the literature study. Chapter 6 provides an in-depth study of the ship detection dataset used to test the newly developed methods. Chapter 7 analyses the performance of these methods and provides a discussion thereof. Chapter 8 provides a conclusion and discussion of possible future work.

CHAPTER 2 MARITIME DOMAIN AWARENESS

2.1 CHAPTER OVERVIEW

To better contextualize where SAR fits into the greater ship detection picture MDA as a concept needs introduced. This chapter describes what is MDA, what South Africa's role in it is and provides insight into the current and future of solutions used for wide-area maritime monitoring such as transponders and remote sensing.

2.2 MARITIME DOMAIN AWARENESS

Maritime Domain Awareness is the monitoring and understanding of all maritime-related activities [1, 8, 9]. Activities that affect the environment, economic and security aspects of a country's maritime domain require maritime monitoring. All entities are responsible for monitoring their own maritime domains but some specific goals are also included in the MDA initiative, including:

- Identification of potential and verifiable maritime threats.
- Creating a common maritime monitoring goal among governmental, national and international partners.
- Execution of countermeasures.

No single country can monitor all maritime domains and cooperation in many areas is key to the success of MDA [8]. Despite this, countries have a responsibility to monitor and police their own waters. Specifically, countries need to ensure their territorial waters (extending approximately 22 km from the coast) and EEZ (approximately 322 km from the coast) are regulated and monitored constantly.

Countries' EEZs are threatened by a number of maritime-related activities. One major threat is illegal, unreported and unregulated fishing (IUU) [10]. It has been estimated that worldwide economic losses due to IUU fishing amount to between \$10 and \$23.5 billion annually. IUU fishing also poses the highest threat to developing countries, such as South Africa, which are expected to lose approximately \$1 billion due to IUU fishing [10, 11]. Other major problems related to the maritime domain include drug and human trafficking, piracy and terrorism [12].

A number of countries are actively invested in MDA. The United States was one of the first countries to instantiate a national MDA directive [8]. This directive allowed for the creation of support networks with foreign governments to not only improve the United State's maritime knowledge but also that of its maritime partners. A number of maritime partners have used these directives in their own plans for MDA improvement for their own region. Canada, possessing the longest coastline in the world, is also a significant contributor to global MDA relations and has maintained its own MDA directives since at least 2004 [13]. Similar to the efforts from the USA, the Canadian government recognized that to effectively monitor all domains related to maritime security an improved collaboration between itself and other MDA countries was necessary. Finally, another significant global MDA partner is Norway which posses a long coastline thanks to its fjords and Svalbard. It has provided valuable inputs into the European Union's MDA policies [14].

South Africa has been a key supporter of improved MDA on the African continent. It has a long coastline (approximately 3900 km long) and has an EEZ which covers a larger area than that of its land (Figure 2.1). One of the busiest routes between the East and West is the Cape Sea Route, catering for approximately 30% of European and American bound oil from the Middle East [15]. The ocean contributed approximately \$7 billion to South Africa's Gross Domestic Product and approximately 316 000 jobs in 2010 [16]. It has been estimated that the South African ocean economy could rise to 1 million jobs in the future and as such focus on this has taken on renewed interest in an intergovernmental initiative called "Operation Phakisa". This initiative seeks to place more focus on South Africa's "blue economy" by empowering growth in various sectors related to the ocean including Marine Protection Services and Ocean Governance [16], which indirectly calls for improved MDA.

Various solutions are available to MDA countries to perform maritime monitoring. The first is in-situ and on-the-ground measurements. These methods typically work well for smaller marine areas that need to be monitored constantly with real-time updates but are affected by limited range. To monitor

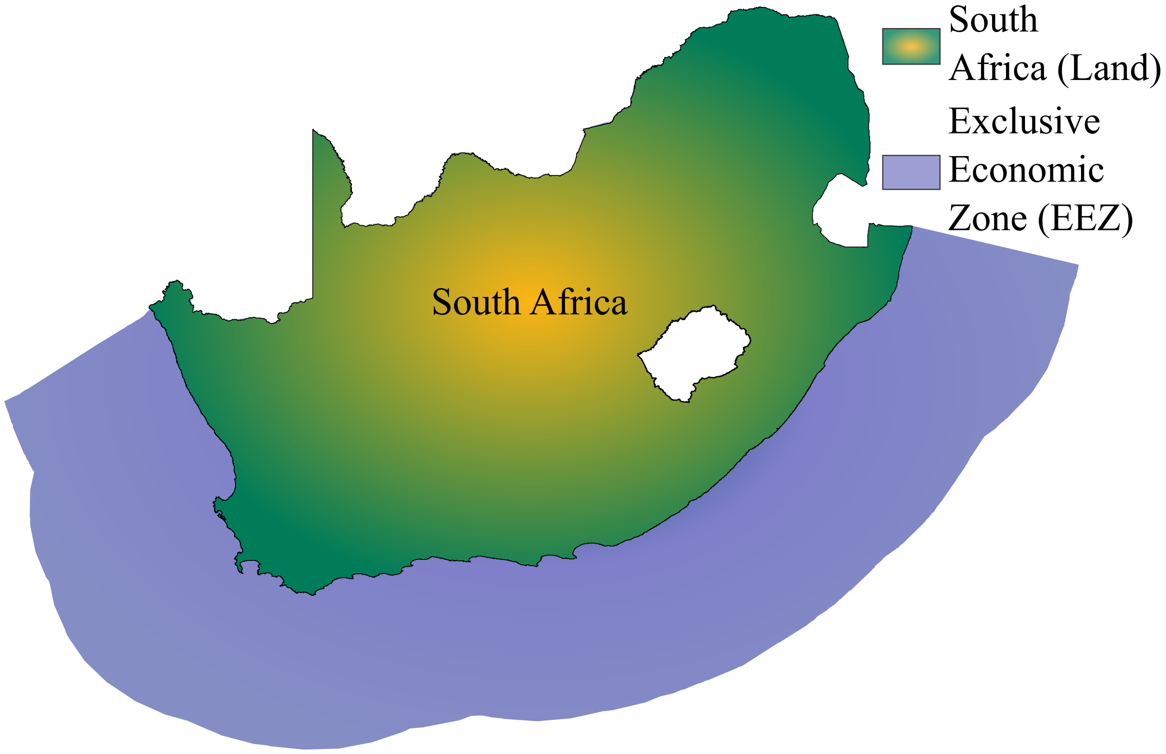

Figure 2.1. Comparison between South Africa's EEZ and its land area. South Africa's EEZ covers approximately 1 500 000 km^2 while its land which occupies approximately 1 200 000 km^2.

large areas, such as the South African EEZ, two different yet related types of solutions exist. The first, transponders, is a means of monitoring ships at sea using their cooperation. A second method, remote sensing, uses a platform such as a satellite which is unconnected to the ocean or ships to monitor areas from a distance.

2.3 TRANSPONDERS

To effectively monitor the oceans a means of tracking the various ships at sea needs to be utilized [17]. Ships are necessary to travel the seas and as such any method that helps to track these ships is necessary for safety, security and enviornmental reasons. Transponders are devices which can help track ships at sea by acting as a tracking device installed onboard the ships. They are installed onto some ships and transmit the ship's position and other details at regular intervals and are received via terrestrial or satellite-based receivers [18].

2.3.1 AIS

The Automatic Identification System (AIS) has become one of the most widely-spread transponder-based tracking systems for MDA [19]. It was first introduced in Sweden in 1993 and was later developed into a ship tracking system. The International Maritime Organization (IMO) mandated that by 1 January 2005, all ships with a gross tonnage over 300 engaged in international travel, all cargo ships with gross tonnage over 500 and all passenger ships are required to carry an AIS transmitter [19, 20].

AIS has two types of transponders, class A (primarily installed on commercial ships) and class B (primarily installed on fishing ships). These transponders use Very High Frequency (VHF) transmission bands and have a Global Position System (GPS) device installed to determine the device's position [20]. These transponders use International Telecommunication Union (ITU) protocols to transmit information such as the ship's Maritime Mobile Service Identity (MMSI), IMO number, position (longitude/latitude), date/time, length, breadth and heading [19].

A technique known as Time Division Multiple Access (TDMA) is used which allows multiple AIS transceivers to allocate transmissions within a limited bandwidth [20]. AIS has two frequencies used for broadcasting which makes provisions for up to 4500 different communication channels every 60 seconds. Transmission interference is mitigated by utilizing bidirectional transmission on both channels. Ships are granted time slots within a 60 second interval and are required to register their next time slot during their current one. AIS allows for adaptable processing which prefers closer ships to more distant ones which is due to the design of AIS as a collision avoidance system.

AIS can be received in two primary manners. The first is via coastal-based receivers which receive transmission signals within Line-of-Sight (LOS) and have near-real time temporal frequency. To track ships further out at sea using AIS satellite-based receivers need to be employed. When AIS messages are received via a satellite and relayed back to a ground station it is known as Sat-AIS. Sat-AIS has a more course temporal frequency but allows for the monitoring of ships globally.

2.3.2 LRIT

Long-Range Identification and Tracking (LRIT) is another ship transponder system. It is similar to AIS but only operates using satellite-based receivers. The IMO introduced the Safety of Life At Sea (SOLAS) resolution which detailed the implementation and enforcement of the LRIT system [20]. LRIT is now mandated for all ships from 2008 onwards and is mandatory installation for all passenger ships, high speed ships and cargo ships with gross tonnage of 300 and over.

LRIT makes provision for member states to request timely reports of ship identity and location. These requests can be made by member state ships or those ships which fall within the member state's coastline. There are two types of reports: on-demand and prescheduled. Both versions are configured in a request/response manner whereby ships on international voyages need to send reports with their identity, position and time/date stamp. Prescheduled reports need to be transmitted at least every 6 hours whereas on-demand reporting has no such limits. Message reporting frequencies can range from a maximum frequency of one report every 15 minutes (96 reports every 24 hours) to a minimum of 1 report every 6 hours (4 reports every 24 hours). Member states can further request reports that inform when a ship is within 1000 nautical miles from its coastline. Similarly, ports can request reports from ships requiring entry.

The primary difference between AIS and LRIT is that LRIT has positional access control. AIS data is broadcast freely and unencrypted so anyone with a compatible AIS receiver can receive AIS messages, decode them and have the positional information of any ships within range. LRIT's member state access list ensures that only groups with the correct permissions can view the information contained within the LRIT messages. This level of security is highly desirable for commercial entities to privately keep track of their assets.

2.3.3 VMS

The Vessel Monitoring System (VMS) is one of the primary ways of tracking fishing ships at sea. In a similar manner to LRIT, VMS transponders transmit the ship's position, name, MMSI and other information to a satellite-based receiver which then relays these messages to the partners associated

Table 2.1. Various types of transponder systems including AIS, LRIT and VMS with details on coverage, message delay and data access, derived from information in [23].

	Terrestrial	Satellite		
Attributes	AIS	SAT-AIS	LRIT	VMS
Coverage	Coastal LOS 85 km	Global	Global	Global
Message Delay	Real-time (minutes)	±6 hours	±6 hours	±6 hours
Minimum Reporting Interval (s)	2	3600	900	1800
Data access	Open	Closed	Closed	Closed

with that fishing ship. VMS supports the ability to log fishing catches so fishing effort can be studied [21].

VMS typically transmits messages to the receiver every 30-120 minutes, depending on the region the ship is in. In much the same way as LRIT, VMS is a closed-access system whereby only registered receivers will receive updated information about the ships pertinent to them. VMS has seen usage in a number of cases, including marine spatial planning for marine protected areas, documentation of fishery track records and analysis of maritime fishing trip efficiency [22, 21].

VMS is of particular interest to countries who use fishing as a means of income. Generally fishing ships that operate within an EEZ are mandated to carry and transmit their fishing catches and ship information using VMS. This allows the fishing authority in any given country to determine the number of foreign flagged fishing ships within the EEZ.

2.4 TRANSPONDERS FOR MONITORING

To understand how effective transponders are at tracking ships at sea we need to first identify each of the advantages and disadvantages of the different methods. Table 2.1 provides an overview of the most important characteristics of the different transponder-based ship tracking methods.

The table shows how conventional AIS can only keep track of ships within LOS from the coast whereas the other solutions all have global coverage. A system overview of these methods work is shown in Figure. 2.2. Despite this greatly extended coverage, the satellite sensors have two difficulties. The first is a message delay and the second is message congestion. For satellite-based transponders the delay between transmission to the client receiving the message can be hours [24] whereas terrestrial AIS can have message delays within minutes. The difference is due to how the data is relayed back as shown in Figure. 2.2. If the nearest data server is in the direction opposite to the satellites orbit direction then delays can be even greater as the data has to be sent to next nearest data server and then processed then forwarded on to the data receiver.

Another significant issue with the original AIS specifications is the system was designed for a fixed number of slots per minute for ships to transmit their message and reserve their next spot. Due to the fact that space-based AIS has a much wider foot print, the number of ships present increases and therefore can cause congestion issues not planned for previously. Studies have shown that this congestion create a limit to the number of ships that are detectable for a given satellite coverage footprint [24]. For instance, an AIS satellite with a coverage receving width of 150 km has a less than 1% chance of receiving all information for all ships in that area if that specific area has more than 3000 ships within it [24]. Various techniques can be used to reduce this problem but even then delays in reporting frequency and other issues occur which cannot be readily fixed without additional satellites or using alternative frequency AIS modes and similar solutions [24].

Finally, the single biggest issue with transponder-based systems is that they can be turned off, sabotaged or damaged. If a transponder system is not transmitting its location then the ship cannot be tracked using a transponder and as such transponder tracking is known as “cooperative tracking” [25]. This means the ships need to cooperate in sending their positional information, in a timely and correct manner. In some instances even if the ships do send their position information this information can be falsified [26]. Despite these shortfalls transponder-based tracking is widely used for ship tracking [18]. These methods can be supplemented using a wide-area non-cooperative method such as remote sensing.

2.5 REMOTE SENSING

The observation of the Earth’s features using a platform unconnected to the area of observation is known as remote sensing. Airborne- and satellite-based instruments are used to infer characteristics of objects on the Earth’s surface using their geophysical properties for identification [2]. These instruments emit and receive EM radiation which is then analyzed to provide interpretations of the

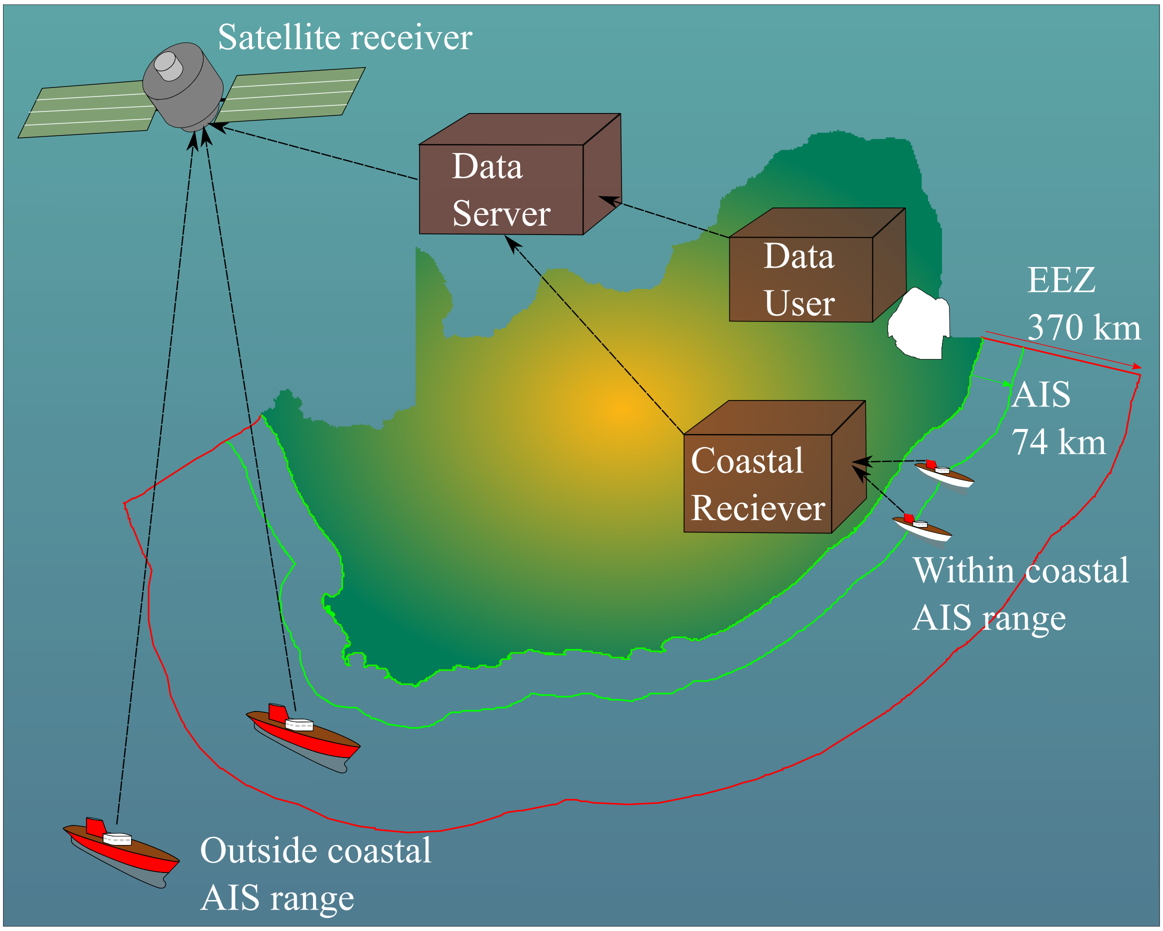

Figure 2.2. Transponder systems and their ranges. Coastal AIS coverage extends approximately 74 km from the coastline whereas the EEZ extends approximately 370 km from the coastline [20, 24]. Ships outside the coastal AIS range can relay their positional information to a satellite in a similar manner to LRIT and VMS.

physical situation not in direct contact with the observer [2]. This provides the observer with the ability to monitor areas which may be inaccessible to them or to observe larger areas than could be done using ground-based in-situ measurements.

Satellite-based remote sensing provides a means of monitoring large ocean areas which can improve a country's MDA [17, 27, 3]. The techniques for MDA observation range from optical satellites and LiDAR to radar at various wavelengths.

2.5.1 Electromagnetic Radiation

Remote sensing sensors uses emitted and reflected EM radiation to observe large areas using either passive or active EM instruments. Passive instruments use the reflected radiation from the Sun to observe an area by measuring how much of the Sun's EM radiation is reflected or absorbed. Active instruments transmit their own pulses of EM energy and the interaction of these pulses with the objects is then used to discriminate amongst targets.

EM radiation is divided into a number of bands known as the EM bands [2, 28]. Each band relates to different aspects of the EM spectrum such as visibility and associated power/frequency. An example of the distribution of different EM wavelengths, their associated instruments and names is shown in Figure 2.3.

The applications of these bands vary from land cover applications using the electro-optical Moderate-resolution imaging spectroradiometer (MODIS) [29] and L-band SAR sensors [30] to C-band ocean [31] and LiDAR-based sea ice measurements [32]. This study will give a general overview of the different sensors used to improve MDA but will focus on the application of SAR imagery for ship detection.

2.5.2 Remote sensing and monitoring for MDA

The first civilian remote sensing platform for ocean monitoring SeaSAT [2] launched in 1978 and provided the first SAR-based sensor to the remote sensing community. Since then, remote sensing of the maritime platform has grown to make use of most of the EM bands for maritime monitoring [2, 32, 29, 30]. Two types of EM sensors are of particular interest to MDA, namely passive and active sensors:

Passive sensors Spectral sensors use the EM radiation from the Sun to observe maritime areas passively and can be airborne or spaceborne [28]. Depending on the instruments aboard the platform, the sensor can make use of multi-/hyper-spectral, infrared or visible EM radiation to observe different properties of the ocean [2, 28]. These sensors are of particular interest to oceanographers for environmental purposes [28].

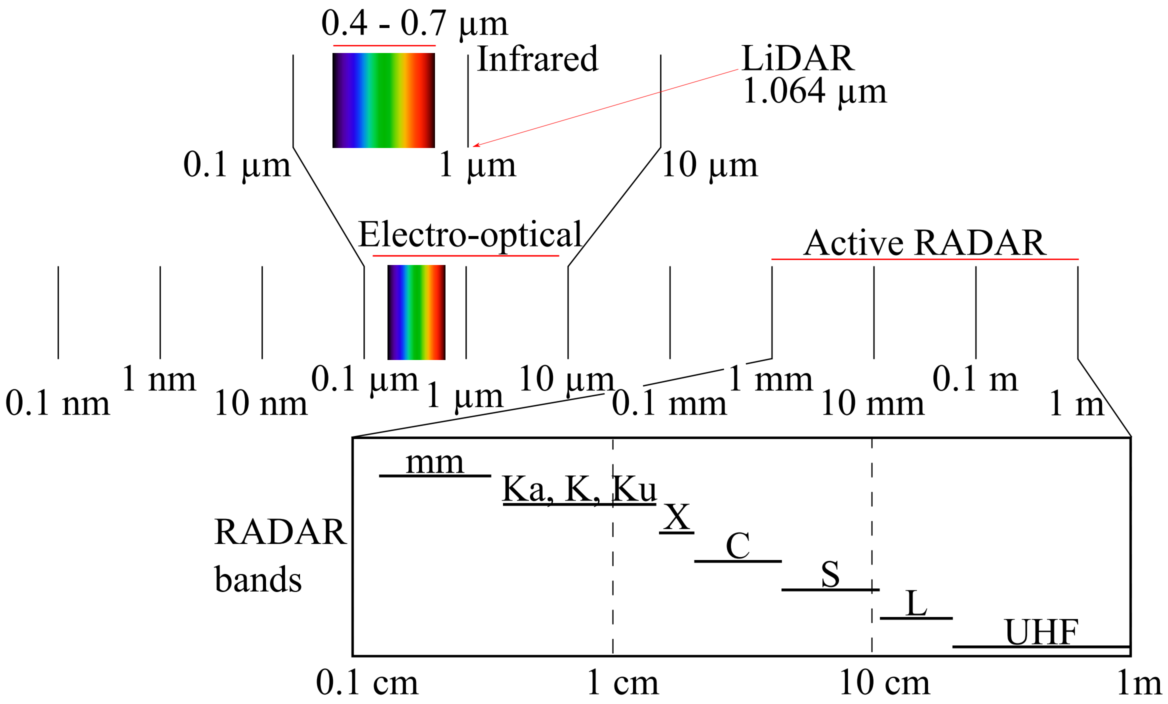

Figure 2.3. The various EM bands and their wavelengths ranges for the EM sensor instruments. This graph shows the most common EM spectra used for remote sensing including the electro-optical, LiDAR and radar bands.

Active sensors Radio detection and ranging (radar) is an active remote sensing technique which transmits EM pulses of energy in the 1 mm – 1 m range and measures the time taken for these pulses to return to determine distance to the target [18, 2, 33]. Radar remote sensing can be terrestrial-based [34] or satellite-based [2] depending on the footprint required to monitored. Some radar EM bands, such as C-band SAR, are useful for monitoring large ocean areas as they do not interact with clouds which can be a problem for Electro-optical EM sensors [18, 2, 31]. Often the radar wavelength is chosen based on what specific application is necessary. For instance, LiDAR uses the same principle as radar but emits EM waves with wavelengths of approximately 1.064 µm to measure structures such as sea surface ice [32].

2.5.3 Spectral- vs radar-based remote sensing

Table. 2.2 presents the most pertinent differences between Spectral-, LiDAR- and radar-based remote sensing. These are general concepts but in some cases there may be sensors that do not follow this table such as the Visible Infrared Imager Radiometer Suite (VIIRS) day/night band spectral sensor [35]

Table 2.2. Comparison between Optical/Spectral imaging, LiDAR and radar based remote sensing instruments. Note these are general observations that occur and in some cases are not always true (e.g. High precision interferometric SAR needs to take weather into account).

Attributes	Spectral	LiDAR	radar
Supported Platforms	Spaceborne & Airborne	Airborne	Spaceborne & Airborne
Measurement technique	Passive	Active	Active
Measurement type (primary)	Chemical	Geophysical	Geophysical
Measurement spectrum	Visible & Infrared	Infrared	Microwave
Acquisition time	Day	Day & Night	Day & Night
Weather Dependence	Impeded by cloud cover	Impeded by cloud cover	Weather-independant
Bands of Operation	10 (Multi) to 1000 (Hyper)	Single	Single
Polarimetry	Not Applicable	Not Applicable	Available
Interferometry	Not Applicable	Not Applicable	Available

or multi-band SAR [36]. The major advantage of radar-based imaging is that it can monitor areas using active EM waves which allow it to circumvent problems such as cloud cover or lack of night-time acquisitions. Another reason is ships further out to sea are larger and hence are of metal construction which is highlighted well using active sensors [18]. Optical imagery can be hampered by these factors which play a significant role in identifying targets for MDA and as such radar-based remote sensing was chosen as the focus of this study above that of optical imagery.

2.6 CONCLUSION

MDA is an important part of any country's agenda and specifically those bordering on the sea. This chapter introduces what it is, how it seeks to improve all sea-bordering countries maritime domain knowledge and which are the important members of the MDA initiative. South Africa long coastline and large EEZ contributes to the requirement of improving its maritime monitoring capabilities.

It was shown that to improve maritime ship monitoring two main methods are employed, namely transponder-based systems and remote sensing systems. Transponder-based monitoring is the most widely used method for ship tracking. By installing a transponder on a ship it can be monitored at various distances depending on whether the receiving is done via land or satellite receivers. Despite its ubiquity, transponder-based systems have some disadvantages such as LOS issues, congestion or closed data-access policies. The biggest disadvantage transponder-based systems have is that they require the cooperation of the ship to work correctly. If the ship turns off the transponder then the ship cannot be tracked.

To supplement transponder-based monitoring, remote sensing monitoring techniques can be used. In the ideal situation all sources of data, remote sensing or otherwise, would be combined to get the best possible MDA picture. Often, however, selections of which sensors to implement need to made due to man-power, time and budgetary constraints. To this end the remote sensing instruments with the biggest initial impact need to be chosen. Given the long coastline that South Africa possesses, the probability of cloud cover and likelihood of night-time illicit activities, the remote sensing method selected for research in this thesis was radar-based imaging. More specifically, the thesis focus on SAR-based observations from spaceborne platforms. This has the acceptable combination of large swaths, revisit times and most recently low-cost per square kilometer due to free access to SAR imagery.

CHAPTER 3 SYNTHETIC APERTURE RADAR

3.1 CHAPTER OVERVIEW

This chapter will give a general overview of SAR, how SAR imagery is formed and discuss some of its parameters. This chapter will also introduce SAR variants as well as some sources of errors including those common to maritime applications. Finally, an introduction into a few of the most prominent SAR satellites will be given with focus on satellites for MDA.

SAR is an active remote sensing technique which can penetrate cloud cover and illuminate large scenes during any time of day [2, 18, 33]. SAR sensors operate on airborne or spaceborne platforms, but for the purpose of this work it is assumed that any reference to SAR herein is referencing spaceborne SAR. This is due to the wider area that can be covered at a reduced cost per area. Due to the fact that radar is an active sensing technique SAR imagery provides a view of the Earth that is independent of the Sun's illumination which benefits MDA greatly by allowing observations to take place during the night time when illicit activities are difficult to see far out in the ocean (see Figure 3.1).

3.2 SAR PRINCIPLES

SAR is a form of radar that is used to image objects within a given scene. SAR uses the relative motion of the platform to synthesize a longer antenna than would typically be physically possible. The SAR platform transmits successive radar pulses and measures the time and power of the returned echos. The platform moves a given distance between the transmission and receiving of a radar pulse and this distance determines the synthetic length of the SAR sensor's antenna. Generally, the longer the radar antenna aperture the better the SAR resolution. The location of the SAR sensor's antenna also changes with respect to the object in time thanks to the Doppler effect [37]. Signal processing utilizes this time delay and Doppler frequency separation to form SAR images which are independent of the distance to the targets and yet can have sub-meter resolution, even from spaceborne platforms. SAR is also a side-looking technique in that SAR images are taken facing the left or right, depending on the configuration of the SAR platform. The side-looking nature of SAR is necessary to separate objects using radar principles and provides a unique perspective on surface objects. The side-looking nature also brings about its own artifacts unlike those in conventional optical imagery and these need to be understood to properly analyze SAR imagery [2].

The power signals returned from objects in SAR imagery are often referred to as backscatter. SAR sensors provide radar backscatter measurements which are influenced by the structure and roughness of objects on the surface. Objects within these images that are specular reflectors, such as ships, will return a higher backscatter compared to diffuse reflectors, such as the ocean. Finally, smoother objects such as a calm ocean area will have a higher backscatter compared to turbulent ocean areas [18]. Figure 3.2 gives a general overview of some of the terms used in SAR image processing.

3.2.1 SAR Imaging

SAR imaging is the process of converting the raw signals from two directions to create a SAR image. Raw SAR data is a record of signal energy in the range and azimuth directions. The range direction is the direction perpendicular to the platform's flight path whereas the azimuth is all components parallel to the flight path of the SAR sensor. Imaging objects in the range direction uses the time/distance principle of radar. The SAR antenna transmits EM pulses at regular intervals known as the pulse repetition frequency (PRF) to separate targets using their delayed responses. Targets closer in the range direction will reflect these pulses before those further away. This time delay between near and far range targets allows SAR imagery to separate targets in the range direction. Given the time taken t for an EM pulse traveling at the speed of light c to return to the transmitting instrument, the slant range distance x_r to the target will be

$$x_r = \frac{ct}{2}, \tag{3.1}$$

where the factor of $\frac{1}{2}$ accounts for the distance traveled there and back by the EM pulse [37].

To separate targets in the azimuth direction SAR imaging relies on the assumption that targets are at

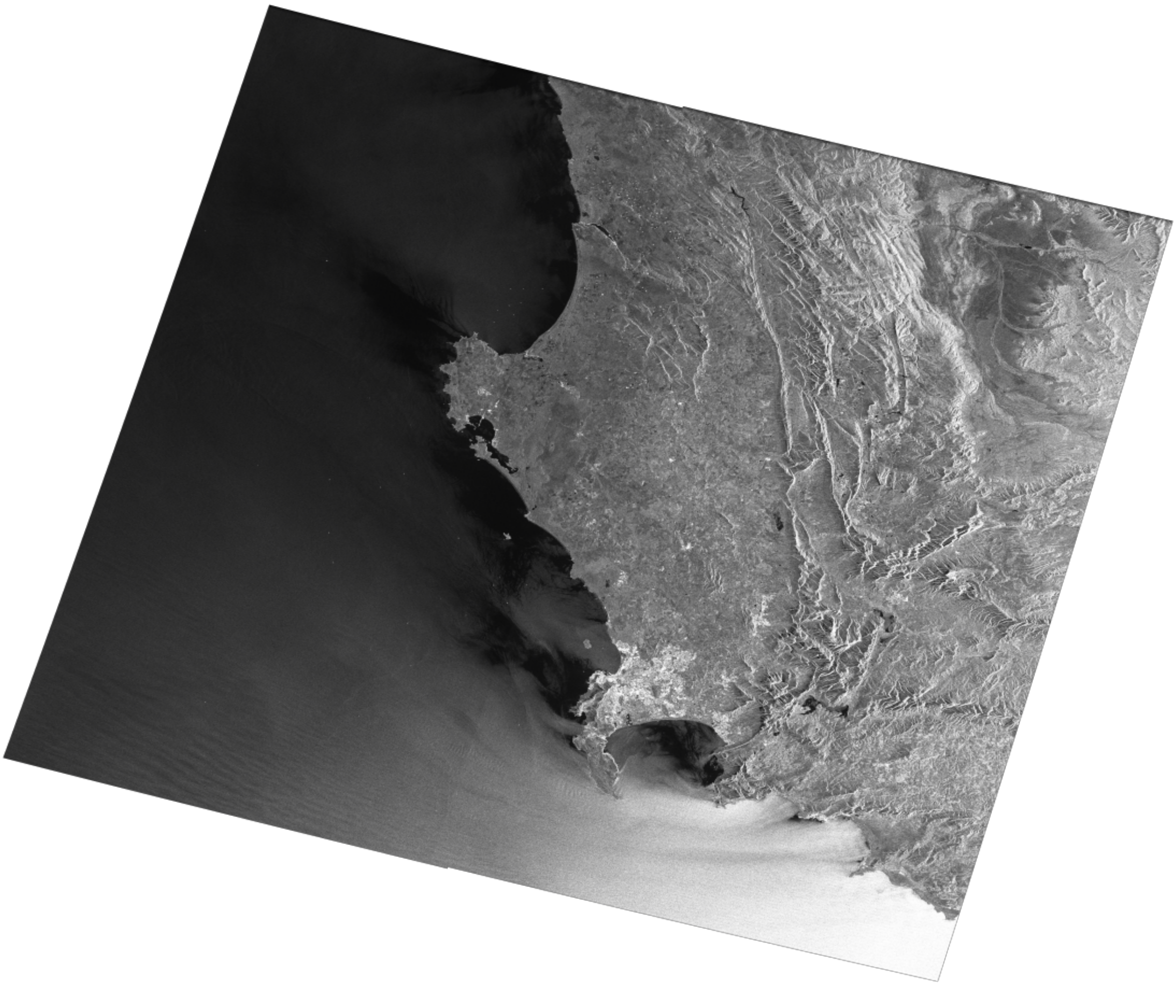

Figure 3.1. A SAR satellite image over Cape Town, South Africa (33.9249° S, 18.4241° E). The image comes from the Canadian satellite RADARSAT-2 and was imaged on the 5th October 2014 at 04:06 AM. The image was taken in a dark setting yet the scene is clearly illuminated and covers an area of $300\,\mathrm{km} \times 300\,\mathrm{km}$. Notice how the mountain areas tilt towards the bright (nadir) position along the right of the image. Furthermore, areas around the bay have dark areas of ocean area surrounded by brighter areas of water. These are all effects of SAR imaging that will be discussed in this chapter.

different angles with respect the flight path of the antenna which causes the targets to have slightly different relative speeds. This difference in speed causes a shift in the observed frequency of a transmitted signal due to the Doppler history effect [37]. By noting the difference in frequencies observed at the antenna from those transmitted, SAR imagery is able to separate targets moving parallel to the flight of the antenna. Given a target reflecting EM pulses with original frequency f_s, moving

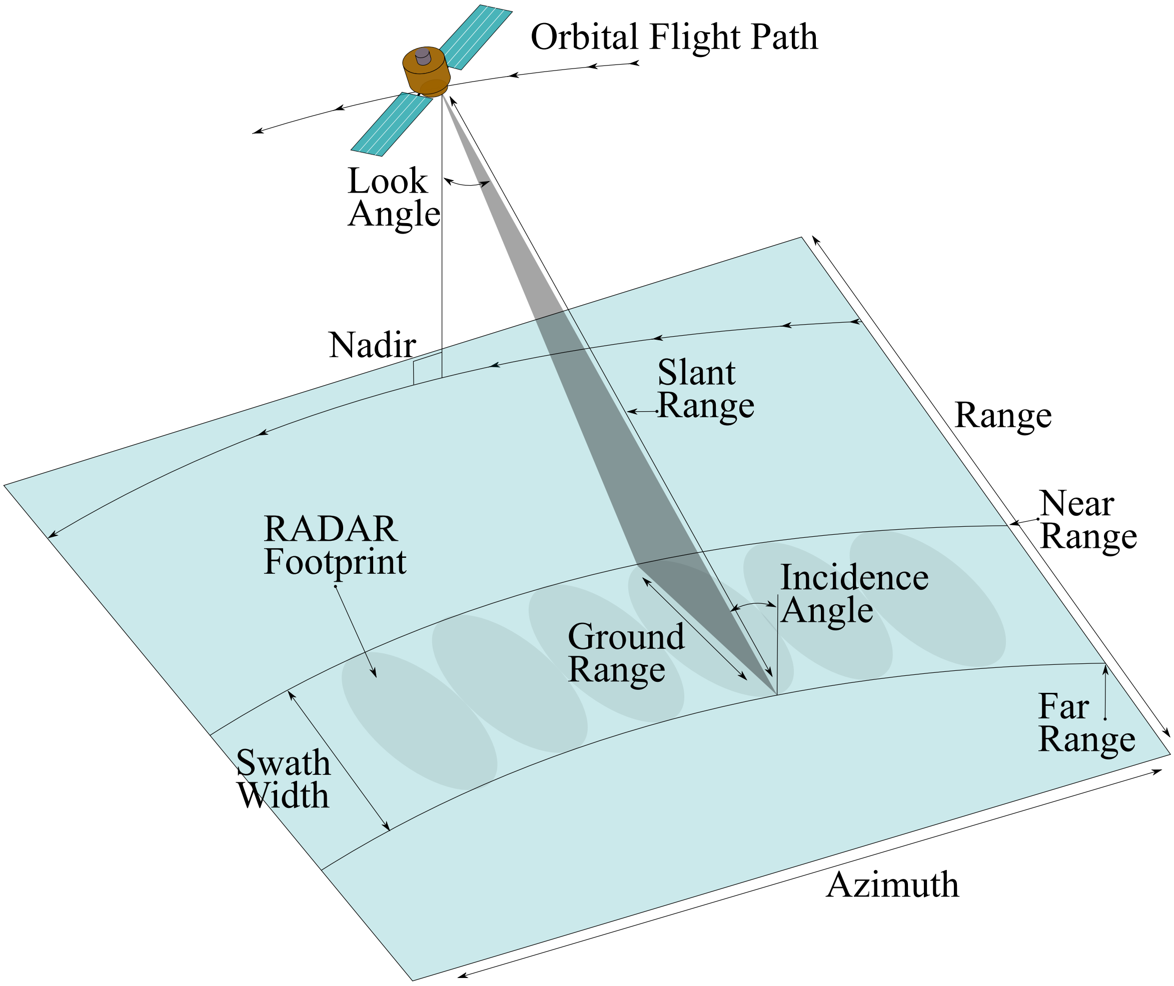

Figure 3.2. SAR imaging principles and common terms.

away from the antenna with a velocity of v, the observed frequency f_o will be

$$f_o = \sqrt{\frac{1-\left(\frac{v}{c}\right)}{1+\left(\frac{v}{c}\right)}}f_s. \tag{3.2}$$

When a reflecting target is moving towards the antenna the observed frequency will be

$$f_o = \sqrt{\frac{1+\left(\frac{v}{c}\right)}{1-\left(\frac{v}{c}\right)}}f_s. \tag{3.3}$$

This indicates that targets moving away will have a lower observed frequency whereas ones approaching the antenna will have a higher frequency. Using this shift in frequency due to the Doppler effect to resolve targets in the azimuthal direction was previously known as Doppler beam sharpening (frequency domain) but is now referred to as SAR processing (time domain) [37, 38].

3.2.2 Incidence Angle, Ground Range and Slant Range

One important distinction of SAR is that it is a side-looking remote sensing technique. The side-looking aspect is necessary in order to provide separate targets in the azimuth direction with a higher resolution compared to real-aperture radar [37].

The angle made between the nadir and radar beam direction is known as the look angle. The look angle of space-based SAR platforms typically varies between $20^\circ - 40^\circ$ and varies from the near to the far range of the platform as shown in Figure 3.2. A related term, the incidence angle, is the angle between the radar and the surface normal. When assuming a flat Earth area and a low altitude then the incidence angle is equal to the look angle of the platform. Due to the effect of the curvature of the Earth and height of the platform in spaceborne SAR, look angle and incidence angle cannot be considered the same. In this case, we refer to incidence angle as the local incidence angle which may vary from resolution cell to resolution cell [37].

The incidence angle of the platform determines the angle at which the objects on the surface are measured. For range measurements, the distance to the target is the direct line of sight from the platform to the object as calculated in equation (3.1) for a given local incidence angle. This range is known as the slant range yet most literature and SAR imagery work is done on the ground range which is size of the across track beam on the ground. Given a local incidence angle of an object of θ and a slant range distance of x_r, the ground range distance x_g is

$$\begin{aligned} x_r &= x_g \sin\theta, \\ x_g &= \frac{x_r}{\sin\theta}. \end{aligned} \tag{3.4}$$

This projection from ground to slant ranges can cause artifacts that are only applicable to side-looking imaging. These effects are generally caused by differing heights of objects compared to one another but are less of a problem for maritime applications.

The monitoring of an area can be highly dependent upon the resolution of the imaging platform used. For maritime domain awareness, all aspects of the resolution of the data plays an important role in defining the limits of the system, where and how often the platform can monitor a specific maritime area and what data can be reasonably expected so that sensible comparisons across acquisitions can be made. In addition to this, the range and azimuth resolutions are often different and therefore require different techniques to extract meaningful data.

3.3 RANGE RESOLUTION

Range resolution refers to the minimum separable distance between two targets in the across-track distance. Assuming two targets separated in the slant range the time difference between each pulse Δt (and therefore target's echo) can be defined as

$$\Delta t = \frac{2x_r}{c}, \tag{3.5}$$

where, as in equation (3.1), the 2 accounts for the round-trip time of the pulse. Due to the fact that two targets can only be separated if the leading edge of the second target is received after the trailing edge of the first target, we can assume that the smallest separable time difference is equal to the effective length of the pulse τ such that $\Delta t = \tau$ [37]. Using equation (3.4) we can then define the slant x_r and ground range x_g in terms of effective time length as

$$x_r = \frac{c\tau}{2}, \tag{3.6}$$

$$x_g = \frac{c\tau}{2\sin\theta}. \tag{3.7}$$

It is important to note that ground range resolution is therefore dependent on the local incidence angle and can vary due to local slopes in an image.

To properly image an area using SAR an effective level of signal needs to be returned compared to noise in the system. A high Signal-to-Noise Ratio (SNR) is required to effectively image an area in SAR. A high SNR in SAR imaging can be achieved using either high power peak transmission signals or long pulse durations. Power on a spaceborne platform is a finite resource and thus continually transmitting with high peak power is not feasible. Therefore, to achieve high SNR long pulse widths are required but this has an adverse effect on resolution according to equation (3.7). To circumvent this high SNR/high resolution trade off, SAR sensor designers employ signal modulation techniques.

To understand how signal modulation can improve range resolution we need to convert the problem into the frequency domain. Effective pulse width is typically defined in terms of system bandwidth such that

$$\tau = \frac{1}{B} \tag{3.8}$$

where B is the system bandwidth measured in hertz [37, 39]. To achieve a large bandwidth which is a small effective time length a chirped signal is used. A chirp is a signal whose frequency is varied linearly while the pulse is being transmitted. Assuming the frequency f_0 is changed by Δf then from [37, 39] system bandwidth can be defined as

$$\begin{aligned} B &= |\,(f_0 + \Delta f) - f_0|, \\ &= |\Delta f|. \end{aligned} \tag{3.9}$$

Here B is independent of the physical pulse length τ_p thus allowing a long τ_p which improves SNR while simultaneously allowing wide bandwidth B. A high B decreases effective time length τ thereby improving range resolution. It should be noted that while the time difference returns from targets much smaller than τ cannot be separated in time, they can be separated in the frequency domain [37]. If the frequency is modulated using chirping then the returns from two targets will have different frequencies and thus can be separated using a matched filter.

Finally, using the above including equations (3.7), (3.8) we can define the resolution in the slant range Δx_r and ground range Δx_g as

$$\Delta x_r = \frac{c}{2B}, \tag{3.10}$$

$$\Delta x_g = \frac{c}{2 \sin \theta B}. \tag{3.11}$$

where Δ_r and Δ_g refer to the smallest distance in meters targets are separable in range by the SAR imaging.

3.4 AZIMUTH RESOLUTION

Azimuth resolution is the ability of the sensor to distinguish targets in the along track direction. Two targets in the azimuth direction are separable because they have different angle relative to the velocity vector of the platform [37]. This difference in angle causes a difference in Doppler frequencies which can then be filtered in order to separate targets.

Assuming target that is moving towards the antenna with velocity v, with original frequency f_s and observed frequency f_o and given that $c >> v$, we can reformulate equation (3.3) as

$$\begin{aligned}
f_o &= \sqrt{\frac{1+\left(\frac{v}{c}\right)}{1-\left(\frac{v}{c}\right)}}\sqrt{\frac{1+\left(\frac{v}{c}\right)}{1+\left(\frac{v}{c}\right)}}f_s, \\
&= \sqrt{\frac{\left(1+\left(\frac{v}{c}\right)\right)^2}{\left(1-\left(\frac{v}{c}\right)\right)\left(1+\left(\frac{v}{c}\right)\right)}}f_s, \\
&= \sqrt{\frac{\left(1+\left(\frac{v}{c}\right)\right)^2}{1-\left(\frac{v^2}{c^2}\right)}}f_s, \\
&\approx \left(1+\frac{v}{c}\right)f_s, \qquad (3.12)
\end{aligned}$$

because $\frac{v^2}{c^2}$ tends to zero when $c >> v$. The shift in Doppler frequency is the difference between the observed and original frequency multiplied by two to account for the shift on the way and back to the platform [39, 40]. Using equation (3.12), the Doppler frequency observed at the antenna f_D is

$$\begin{aligned}
f_D &= 2\left(f_o - f_s\right), \\
&= 2\left(\left(1+\frac{v}{c}\right)f_s - f_s\right), \\
&= 2\left(f_s + \frac{v}{c}f_s - f_s\right), \\
&= \frac{2vf_s}{c}, \qquad (3.13)
\end{aligned}$$

which provides a means of separating targets based on their observed shift in frequencies. Assuming two targets are the same range distance of X_R, we can define the velocity of the platform v in terms of the target's relative velocity to the platform v_{rel} as

$$v = \frac{yv_{\text{rel}}}{X_R}, \qquad (3.14)$$

where y is the azimuth distance between the two targets [39, 37]. The original frequency f_s of the transmitted pulse can be defined in terms of the transmitted wavelength λ such that $f_s = \frac{c}{\lambda}$. Using this and equations (3.13) and (3.9) the resolution in the azimuth direction can be defined in terms of the

Doppler bandwidth as

$$\begin{aligned} f_D &= \frac{2\frac{y v_{\text{rel}}}{X_R}\frac{c}{\lambda}}{c}, \\ &= \frac{2 y v_{\text{rel}}}{\lambda X_R}, \\ y &= \frac{\lambda X_R}{2 v_{\text{rel}}} f_D, \\ \Delta y &= \frac{\lambda X_R}{2 v_{\text{rel}}} \Delta f_D, \\ &= \frac{\lambda X_R}{2 v_{\text{rel}}} B_D. \end{aligned} \tag{3.15}$$

Finally, the SAR sensor has a radar beam width (footprint) Φ_y which is defined as $\Phi_y = \frac{\lambda}{L_y}$ where L_y is the length of the antenna in the azimuth direction [39]. If the target remains within this beam-width for a time τ_D, this Doppler time can be defined in terms of the above terms such that

$$\begin{aligned} \tau_D &= \frac{y}{v_{\text{rel}}}, \\ &= \frac{X_R \Phi_y}{v_{\text{rel}}}, \\ &= \frac{X_R \lambda}{L_y v_{\text{rel}}}. \end{aligned} \tag{3.16}$$

As the bandwidth is the inverse of the time (see equation (3.8)) and by using equations (3.15) and (3.16), we can define the final azimuth resolution as

$$\begin{aligned} \Delta y &= \frac{\lambda X_R}{2 v_{\text{rel}}} \frac{1}{\tau_D}, \\ &= \frac{\lambda X_R}{2 v_{\text{rel}}} \frac{L_y v_{\text{rel}}}{X_R \lambda}, \\ &= \frac{L_y}{2}. \end{aligned} \tag{3.17}$$

This is one of the fundamental properties of SAR imaging from space and shows that the achievable azimuth resolution is approximately equal to half the length of the antenna in the azimuth direction. It is independent of wavelength and distance to the target. This counter-intuitive result can be explained by the fact that a smaller antenna has a larger footprint on the surface ($\Phi_y = \frac{\lambda}{L_y}$) which means a longer synthetic array is in effect allowing a longer observation time for each point. This increase in observation time increases the Doppler bandwidth which accounts for a finer surface azimuth resolution. An important point to note is that the radar antenna cannot just be reduced to any desired resolution as a number of factors such as PRF/sampling frequency, antenna pattern and so forth.

3.5 RADIOMETRIC RESOLUTION

Radiometric resolution is the average spread of the variation for every resolution cell within the SAR image. It determines the ability of the sensor to distinguish two targets based on their normalized return value. The radiometric resolution $\mathcal{Y}$ can be defined in terms of mean and standard deviation image intensity μ and σ such that

$$\mathcal{Y} = 10\ln\left(\frac{\sigma+\mu}{\mu}\right), \tag{3.18}$$

where lower values for $\mathcal{Y}$ mean improved radiometric resolutions [41]. The variation in each resolution cell of the SAR image is determined by a few well-known effects that are prevalent in SAR including concepts such as speckle noise, thermal noise and signal degradation.

In practical terms the radiometric resolution determines the finite number of quantization levels a radar return is recorded at. Most SAR products are released as unsigned 16-bit images which can allow for a radiometric resolution of 65536 different levels of brightness. In most situations this radiometric resolution is enough to allow for meaningful comparisons between images but can hinder applications such as interferometry and polarimetry [41].

3.6 TEMPORAL RESOLUTION

Temporal resolution refers to the rate at which a specific area can be monitored (i.e. the days between acquisitions of that area). The orbiting nature of SAR satellite platforms means that there are two different types of temporal resolutions when referring to SAR imagery, namely repeat and revisit times. Repeat frequency refers to how often the satellite can monitor the exact same area with the exact same imaging conditions for any given position on Earth. Revisit frequency refers to how often the satellites can image a given area for varying imaging conditions, such as altered look angle or ascending/descending acquisition. Repeat times are an estimate of the time between exact imaging conditions necessary for some types of SAR processing (such as interferometry). Revisit times give an estimate of time it would take to image a given area for operational monitoring that do not require continual acquisition. Typical repeat times can vary from 6 days for the Sentinel-1 A/B to about 34 days for Environment Satellite (ENVISAT). Revisit times are reduced because the exact same positioning is not required and some studies show that given the combination of two satellite constellations

(COSMO/SkyMed and RADARSAT Constellation Mission (RCM)) a mean revisit time of 7 hours can be achieved [42].

3.7 SAR FORMATS

The amount of data the sensor receives is vast and techniques to process this data into usable SAR imagery takes considerable processing [43]. To understand which data is processed by any given algorithm the three main types of SAR data formats need to be discussed.

SAR signals are stored inside RAW data files as two dimensional tables physically related to the sensor (antenna direction and satellite track) but do not represent imagery [44]. SAR satellite providers do allow the distribution of RAW SAR data in order for end-users to process the data in a specific manner. It should be noted that much research has gone into the compression of RAW SAR data in order to provide faster and more efficient transfer of data [43, 44].

When the RAW SAR signals are received on the ground they are compressed using pulse compression algorithms such as the Range-Doppler Algorithm, Chirp Scaling Algorithm or Range Mitigation Algorithm [43, 44, 40]. Single-Look Complex (SLC) data stores the processed RAW signals as a complex matrix where each element (pixel) has an associated amplitude and phase information typically stored using 16-bit values. The single look refers to the fully available signal bandwidth for a given imaging mode with no adjustments made to the data such as multi-look processing. The amplitude data of SLC is of great importance to many remote sensing applications and the phase information allows height estimation using interferometric processing. It should be noted that SLC data is often processed in the slant range and additional processing is required in order to relate SLC results to ground range pixels [43, 44, 40, 45].

While SLC imaging may contain the most information for researchers it contains a lot of speckle noise and is often elongated in the one imaging direction thus making visual interpretation tricky. Two common manners in which speckle is reduced in SAR imagery is by multi-look filtering and adaptive image filtering such as Lee, Frost or Gamma filters [46, 47]. Multi-looking splits the bandwidth of the azimuth spectra into L segments called looks and then incoherently averages these as separate images. This process reduces speckle but comes at the expense of reduced image resolution. Furthermore, in some products the range and azimuth resolutions are different and need to be sampled differently to obtain a square pixel. SAR satellite providers often distribute a single image with only amplitude data where the pixels are both square and converted into the ground range for simpler interpretation. This data is is often labelled a multi-looked or a Ground Range Detected (GRD) product.

3.8 POLARIMETRY

Polarimetry is the measurement of applying transverse wave principles to SAR EM waves. In particular, the interaction of the geometrical orientation of the transmitted radar signals is measured to determine how the object affected the orientation of the signal. SAR imagery can be created for various combinations of these orientations to provide a multiple views of the same area. Targets on the Earth's surface will have distinctive signatures depending on the polarization that interacts with the target. For instance, volume scatters will have polarization properties that differ from those of surface scatterers and thus by imaging areas using different polarizations further classification of these types of targets in an area can be identified.

SAR sensors transmit EM waves as either Vertical (V) or Horizontal (H) polarizations and are received using either Vertical or Horizontal filters. Typically the transmit and receive channels are denoted next to each other so a EM wave sent out as Vertical and received as Vertical is denoted as a VV wave, similarly for VH, HV, and HH waves. Satellite-based SAR sensors can allow for three types of polarization structures - single, dual and quad-mode polarizations. Single refers to SAR antenna transmission and receiving that contain the same polarization such as HH or VV. Dual polarized SAR platforms can send a signal in one orientation (H or V) and receive in both H and V or vice-versa. Quad polarized SAR imagery are generated by platforms that send both H and V signals and receive in both H and V channels.

One way in which SAR polarimetry can be viewed is by noticing that a target alters the polarization upon reflection [37]. This alteration can be summed up by using a matrix of transformation terms which defines the transformation of the transmitted signal to the scattered signal. For a given transmitted EM signal, $\mathbf{E}^{\text{tr}}$, the scattered EM signal $\mathbf{E}^{\text{sc}}$ can be defined as

$$\begin{aligned}\mathbf{E}^{\text{sc}} &= \mathbf{S}\mathbf{E}^{\text{tr}},\\ &= \begin{bmatrix} S_{hh} & S_{hv} \\ S_{vh} & S_{vv} \end{bmatrix} \mathbf{E}^{\text{tr}} \end{aligned} \tag{3.19}$$

and $\mathbf{S}$ is known as the scattering matrix that describes the transformation of $\mathbf{E}^{\text{tr}}$ into $\mathbf{E}^{\text{sc}}$. This scattering matrix is a function of various SAR properties including the transmission frequency and SAR viewing geometry and can be used to synthesize how the target would respond to arbitrary polarization conditions. Decompositions of the scattering matrix generate alternative views of the scene, allowing areas such as vegetation or man-made structures to be highlighted better depending on decomposition parameters. Applications of SAR polarimetry play large roles in MDA in areas such as sea ice identification, coast wind field measurement, oil spill detection, ship detection and classification [37].

3.9 INTERFEROMETRY AND DIFFERENTIAL INTERFEROMETRY

Up until this point SAR signals have been treated as real-valued sampled data but the EM wavelengths associated with SAR are complex composing of amplitude and phase information. The phase difference between two pixels acquired under slightly different sensor positions can provide a wealth of information [48]. Interferometric SAR (InSAR) is a technique which extracts phase differences from two SAR images acquired over the same geographical area at different sensor positions or times. Differences in the interferogram can be due to a number of factors: distance from the SAR sensor to the target; topography and dielectric properties of the surface; frequency used in the two images; satellite orbital parameters; atmospheric effects and system noise. Within the interferogram a number of patterns which represent areas of equal phase are created which are called fringe patterns. Any interference with the backscatterer on the ground can affect the fringe pattern.

The most critical parameter for SAR interferometry is the baseline which is the offset between the two sensors. Two types of SAR interferometry are derived from the two baseline configurations - spatial and temporal. Spatial baselines are two SAR observations separated in distance and occur when two SAR satellites are in a single-pass configuration thereby needing only a single pass of the area to be able to generate interferometric information. Temporal baselines occur when two SAR observations are separated in time and are referred to as repeat-pass interferometry. Smaller baselines allow for more precise identification of SAR height differences whereas larger baselines can cause decorrelation of the phase measured by the variance in phase difference or coherence. In both cases a number of stringent requirements are placed on the imaging parameters including the baseline distance or precise co-registration so both images pixels' match to a given level of error typically less than 0.1 pixel.

Let us assume two SAR complex images are acquired where the first is the master and the second is known as the slave image. For repeat-pass interferometry, the phase difference between the two co-registered images is called the interferometric phase ϕ and is calculated as

$$\phi = \Delta\phi_{\text{range}} + \Delta\phi_{\text{topo}} + \Delta\phi_{\text{phase shift}} + \Delta\phi_{\text{atm}} + \Delta\phi_{\text{dielectric}} + \Delta\phi_{\text{phase noise}} + 2n\pi \tag{3.20}$$

where $\Delta\phi_{\{\text{effect}\}}$ refers to the various effects that can alter the interferometric phase including the range distance, surface topography, shift in phase from master to slave image, atmospheric effects, dielectric properties of backscatterer and phase noise. The final term in (3.20) refers to the ambiguity associated with InSAR processing because the phase wraps around 2π such that any phase value is an n multiple of $\phi \in [0, 2\pi]$. To solve for n requires a technique known as "phase unwrapping" [48]. In most InSAR literature all except the first term in (3.20) are accounted for and by using the measured ϕ from the two phase images as well as the relationship $\Delta\phi_{\text{range}} = \frac{4\pi}{\lambda}\Delta D_0$ the surface displacement ΔD_0 can be calculated given the wavelength of the system. This shows us how interferometric SAR processing can be used to calculate height displacements using SAR which has a number of important applications such as the measurement of earthquakes, landslides, subsidence, structural stability and glacial motion analysis.

Given a series of phase images over the same area offset by a baseline, multiple interferograms can be created and the differences between these interferograms allows for Differential Interferometric SAR (DInSAR) processing. These techniques can map the change in displacement over time which is another good indications of surface stability or movement [49].

3.10 SAR ACQUISITION MODES

SAR imaging from an airborne or spaceborne platform can be undertaken using various configurations (see Figure 3.3). The manner in which a SAR acquisition is taken determines many of the properties of the image such as swath width and pixel resolution. Three main configurations for SAR imaging from space are discussed next.

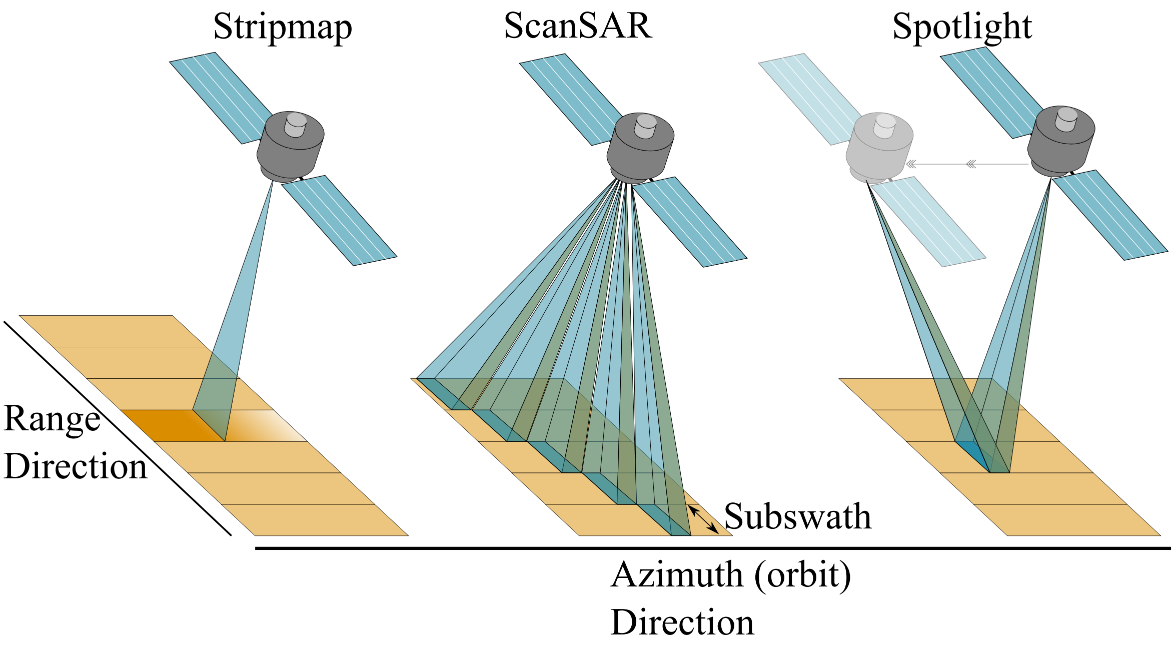

Figure 3.3. The three main acquisition modes for SAR imaging from space. ScanSAR mode is an extension to Stripmap mode by creating a number of subswaths, each a stripmap of their own. The Spotlight imaging mode provides the highest resolution imaging but comes at the cost of reduced swath width.

Stripmap When SAR satellites operate in stripmap mode the imaging swath is varied by changing the look angle of the antenna. Stripmap mode limits the satellite to a fixed narrow swath and generally can be found on historical satellites due to the fixed antenna position.

ScanSAR Modern SAR satellite platforms now make use of the ScanSAR principle. In ScanSAR imaging additional antenna swaths are created by artificially steering the elevation of the antenna differently for each swath. For each elevation angle, the SAR sensor imagines the swath in the same manner as Stripmap imaging but the end of a given swath another nearby (overlapping) one is created by changing elevation of the antenna. Each swath created in this manner is called a sub-swath and multiples of these sub-swaths are combined to create a SAR imaging with similar resolution to Stripmap imaging but with a much larger swath widths.

Spotlight Spotlight SAR imaging provides a much finer azimuth resolution than the other modes by electronically steering the antenna beam so that a single area on the Earth is illuminated during the platform passover. This allows for a number of benefits over Stripmap imaging, including the providing views of an area at multiple angles in a single pass and imaging multiple smaller scenes compared to strips of Earth in Stripmap.

3.11 SAR IMAGE ERRORS AND ARTIFACTS

Due to the unique side-looking nature of SAR imagery, a number of side-effects and sources of error can become apparent as seen in Figure 3.4. These range from effects due to wavelength and coherence all the way to SAR processing and topographical scene effects. This section will discuss the most pertinent errors in SAR imagery with specific focus and examples for errors most likely to occur within MDA applications.

3.11.1 Speckle

Within SAR imagery an SLC or ground-range image contains a single resolution cell of a fixed resolution in range and azimuth direction. For the most part these resolution cells are larger than the wavelength of the SAR sensor. This means that within a given resolution the smaller wavelength may interact with many reflectors within a resolution cell. This causes multiple returns per resolution cell and these wave returns can interfere with one another constructively or destructively. The interference causes a stronger or weaker return in that resolution cell which can manifest as salt and pepper-like noise termed speckle. Speckle is the primary imaging error in SAR imagery and many filters and research has been conducted to reduce the effect of speckle [44, 2]. A cutout on Figure 3.4 shows an example of what speckle looks like over MDA SAR imagery.

3.11.2 Range and azimuth ambiguities

When errors in processing either of these directions occur ambiguities arise. For an example of azimuth and range ambiguities in SAR MDA imagery, see Figure 3.4, Figure 3.5 and Figure 3.6.

Ambiguities in the range direction occur when two radar signals from different pulses are received at the same time. Range ambiguities appear as similarly bright or darker versions of the object but separated in the range direction, sometimes by many kilometers. This makes automatically filtering out these effects a difficult task. The separation distance is affected by a number of factors and generally is

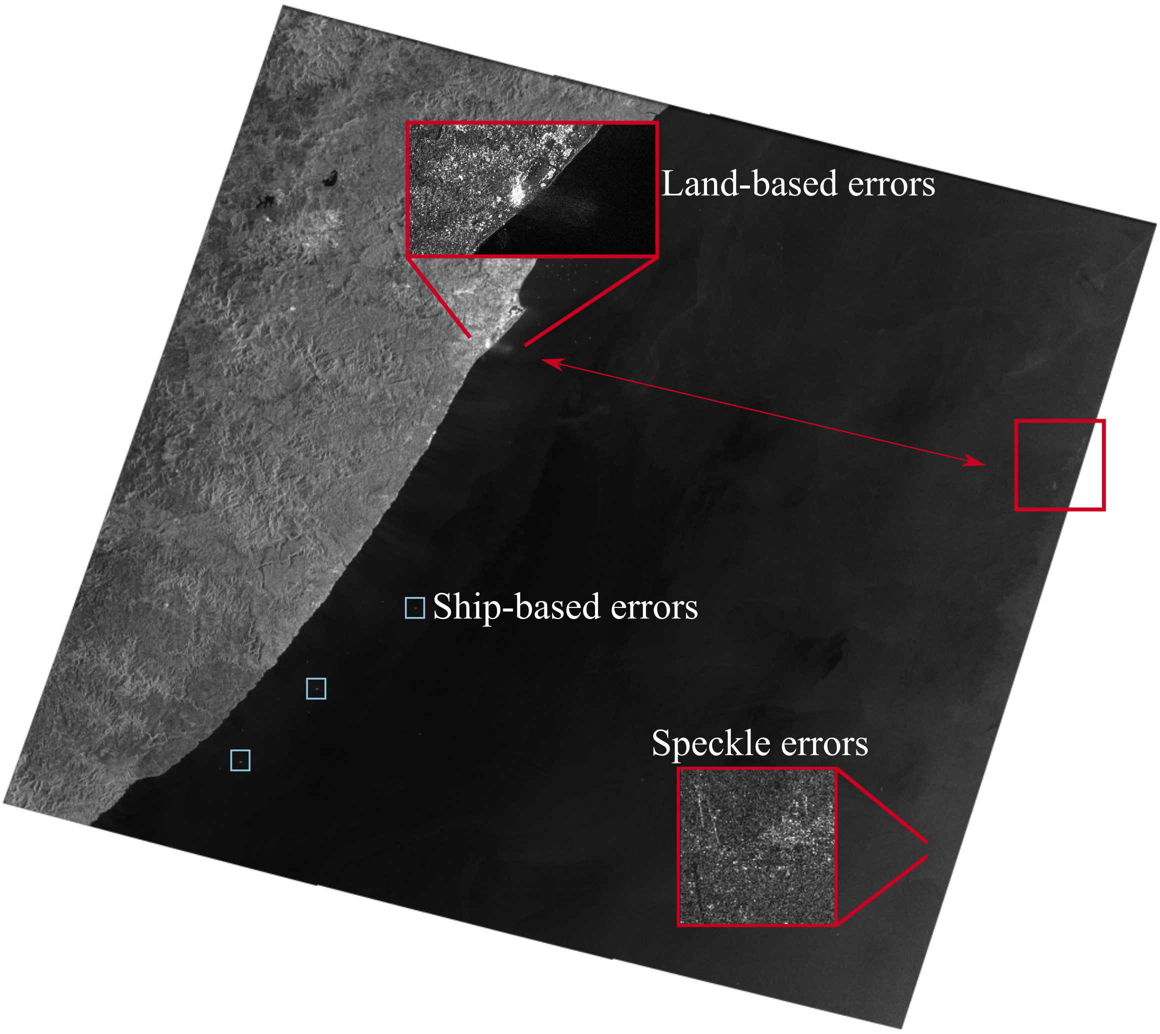

Figure 3.4. A SAR satellite image over Durban, South Africa (29.8587° S, 31.0218° E). It is a RADARSAT-2 SCNB image and was acquired on the 2nd August 2016 at 03:11 AM. The image contains a number of errors unique to SAR imagery. Figure 3.5 and Figure 3.6 show the land- and ship-based errors in more detail.

not accounted for in SAR image preprocessing. Figure 3.4 and Figure 3.5 show examples of these types of ambiguities.

Ambiguities in the azimuth direction are caused by overlapping SAR signal returns with multiple associated Doppler frequencies. The local Doppler frequency is estimated per pixel and is used for the generation of azimuth resolution in SAR. For the general case, the mean value of the azimuth signal can be shifted from zero due to the movement of the platform and thus this can cause a shift in Doppler frequency. This shift needs to be accounted for azimuth errors occur that appear as ghosts. See Figure

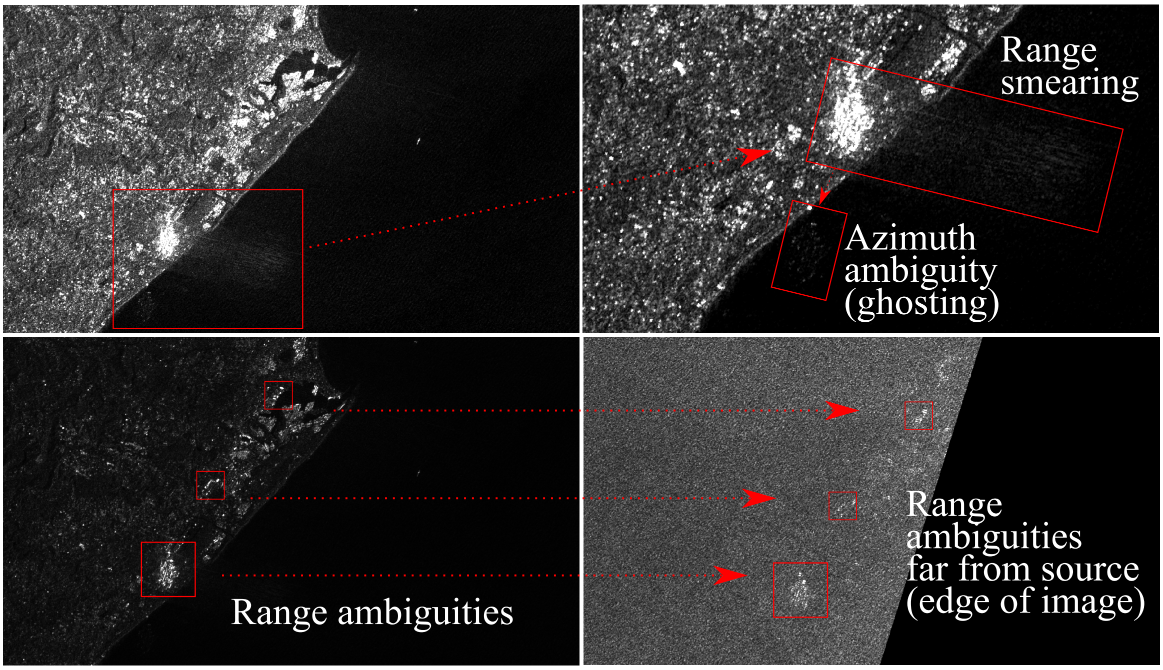

Figure 3.5. This figure shows highlighted areas views of the top left and top right (red) portions of Figure 3.4. This includes azimuth and range ambiguity errors.

3.4, Figure 3.5 and Figure 3.6 for examples of these kinds of errors.

General processing to remove ambiguities is a difficult class of problems still under investigation, specifically in high resolution SAR imagery [50] but also in medium resolution imaging using explicit means such as repeat pass discrimination [51]. More specifically for ship detection most studies filter out the vast majority of ambiguities using size-based filtering [52, 53]. The various satellite providers distribute their SAR imagery as GRD products, often with a number of preprocessed steps already applied to the image. For this thesis it was assumed that the preprocessed GRD imagery presented to the system would have a number of the most obvious errors cleaned up during the conversion from SLC to GRD. Furthermore, the final stage of ship detection would remove detections that are unreasonably large compared to expected ship sizes. For example, ships would be excluded that are 100 pixels long if a single pixel occupies 50 m. Alternatively, it was assumed that the later stages would remove these ambiguities using machine learning techniques by learning what constitutes a real ship and an ambiguity.

3.11.3 Sidelobes

When processing SAR imagery highly reflective objects can have multiple copies near to the original. These multiple copies appear as weaker versions of the original at set distances from the original. Examples of SAR ship sidelobes can be seen in Figure 3.6.

Sidelobes are a direct effect of the finite extent of the aperture which limits bandwidth. Objects in SAR, such as ships, have their responses modeled using what is known as a sinc function. This function has sidelobes which repeat at specific intervals and due to the large dynamic range in SAR imagery these repetitions can often still be seen. In some cases these sidelobes from a ship with strong returns can obscure nearby, weaker-return targets [54].

Apodization is a method of reducing sidelobes [54]. There is a direct relationship between sidelobe power and main lobe power such that if the sidelobes are reduced then the mainlobe's power is also reduced. This trade-off plays an important role in SAR preprocessing efforts but in some cases cannot be controlled depending on the type of product received from the SAR satellite imagery provider For instance, Sentinel-1 GRD products already have their apodization fixed. This is an important factor in understanding results from medium resolution ship detection methods.

3.11.4 Geometric effects

Geographical areas respond differently to SAR wavelengths which may manifest as distortions in an SLC image. Most of these distortions do not occur in SAR imagery over maritime areas but are discussed here for completeness.

SAR sensors measure the time difference between signals for a given area to measure distance. When one signal interacts with the base of a tall object tilted towards the SAR sensor shortly before a second signal interacts with the top, then the perceived time difference between the two signals will be shorter thus indicating a smaller distance. This has the effect of compressing the distance between the top and base of the tall object in the SAR imaging plane causing the object to appear foreshortened. This effect is heavily dependent on the angle at which the tall object is tilted towards the SAR sensor and could be compensated for if a terrain model is available or multiple acquisitions with different inclination angles.

Layover is an extreme form of foreshortening. When a tall object is tilted at such an angle that signals from the top of the object arrive before that of the base, both the top and base of the object will have inverted positions on the SAR imaging plane. These typically occur at low incidence angles where the areas will appear bright in geocoded SAR imagery.

When a tall object sits in the line-of-sight of another shorter object on the ground, the radar cannot see around the tall object. The tall object casts a radar "shadow" that SAR imaging cannot see behind because signals cannot interact past the tall object and thus these regions appear as blank or black areas in SAR imagery.

In SAR imagery for MDA a particular form of shadow manifests. Mountains and large structures can cast a shadow on SAR maritime areas because the wind typically associated with sea-surface roughness is blocked. This causes a "shadow" behind the mountain as the water in this area experiences lower wind speeds which cause the radar signals to be more dispersed [18]. This in turn causes backscatter in these areas to be lower than surrounding ocean areas with higher wind speeds yet objects such as ships within them can still have much higher backscatter. For an example of what this form of shadowing looks like in SAR imagery see the darker water areas off of the coast near Table Mountain in Figure 3.1.

3.12 SAR MISSIONS

Since the release of SEASAT in 1978 [2] SAR satellite observation has played an important role in remote sensing of the Earth. The following subsections each describe some historical and recent SAR satellites and some of their parameters with a summary of all these missions in Table 3.1.

3.12.1 ENVISAT

The Environmental Satellite (ENVISAT) was launched in 2002 and acted as the European Space Agency's (ESA) successor to the ERS satellite missions. ENVISAT operated until 2012 and contained

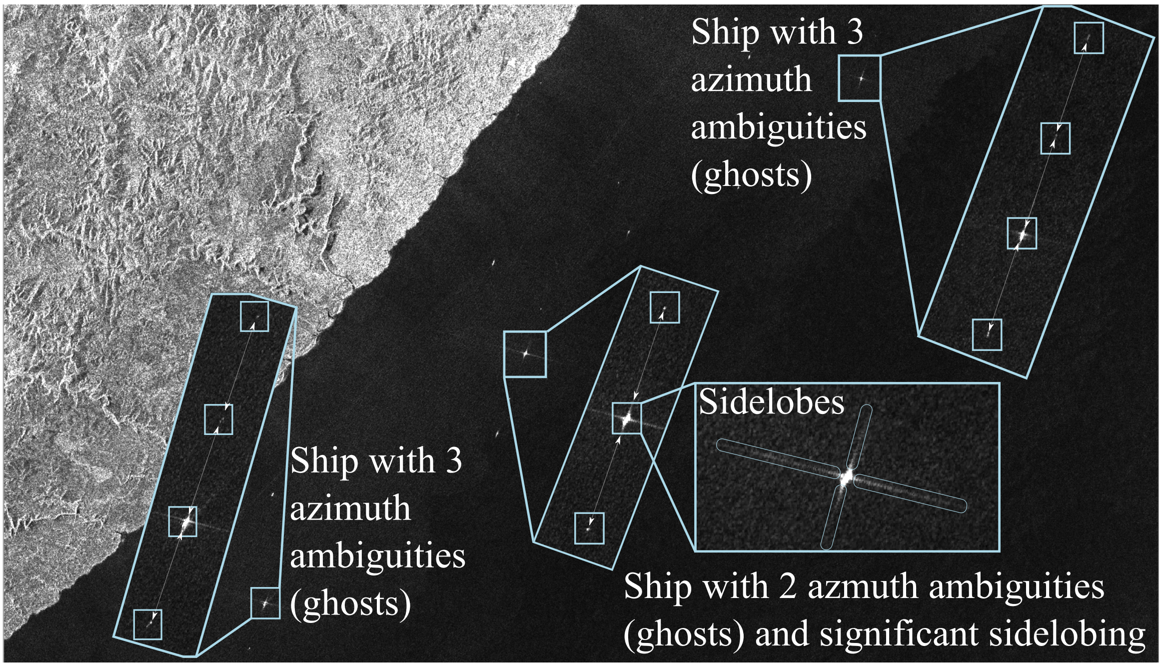

Figure 3.6. This figure shows highlighted views of the three bottom right (blue) portions of Figure 3.4. This includes azimuth ambiguities and sidelobing.

9 remote sensing instruments and delivered over a petabyte of data. It was the only orbiting dual polarimetric SAR satellite until 2007 when RADARSAT-2 was launched. The Advanced SAR (ASAR) instrument aboard the satellite provided a C-band 5.331 GHz, dual-polarization capable SAR sensor that was designed to gather data on water, ice and land areas. It had a 101 minute polar orbit period at an altitude of approximately 790 km. The satellite originally had a 35 day repeat cycle but this was altered in 2010 to 30 days.

3.12.2 SENTINEL-1 A/B

The Sentinel-1A satellite was launched in 2014 and is the ESA's successor to the ENVISAT mission providing global coverage for a number of science missions including maritime monitoring and land-based measurements. The satellite has a Sun-synchronous, near-polar orbit with a period of 98 minutes and a repeat cycle of 12 days at an altitude of 693 km. Onboard is a C-band 5.405 GHz, dual-polarization SAR sensor. To compliment Sentinel-1A, a second identical satellite was launched in 2016 called Sentinel-1B which follows the same orbit as Sentinel-1A but is 180° behind so that the constellation repeat cycle is reduced to 6 days.

3.12.3 RADARSAT-2

Created by the MacDonald Dettwiler and Associates company in association with the Canadian Space Agency (CSA) the RADARSAT-2 satellite was launched in 2007. It is the successor to the original RADARSAT-1 satellite with a number of more advanced device improvements. The RADARSAT-2 sensor is a C-band 5.405 GHz, quad-polarization capable sensor. It has a near-polar 100 minute orbit period at an altitude of 798 km and a repeat cycle of 24 days. It has seen applications in maritime monitoring, geological mapping and agricultural activity monitoring.

3.12.4 TERRASAR-X and TANDEM-X

The TerraSAR-X SAR satellite was developed by the German Aerospace Centre (DLR) in partnership with EADS Astrium and was launched in 2007. In 2010 a partner satellite, TanDEM-X, was launched to fly originally in a helical pattern to create an accurate Digital Elevation Measurement (DEM) of the Earth to an accuracy of approximately 2 m. The satellites use an X-band 9.65 GHz SAR sensor, has a polar, sun-synchronous orbit at an altitude of 514 km with an orbital period 95 minutes. The satellite has a repeat time of 11 days which allows for interferometric processing in both single-pass and repeat-pass configurations.

3.12.5 ALOS-2

The Advanced Land Observing Satellite-2 (ALOS-2) is the successor to the "ALOS-PALSAR" mission and was launched in 2014 by the Japan Aerospace and Exploration Agency (JAXA). It contains an L-band 1.270 GHz quad-polarization capable SAR sensor flying in near polar orbit at an altitude of 628 km. The satellite has an orbital period of 97 minutes with a 14 day repeat cycle which allows for more rapid monitoring of disasters compared to previous JAXA missions. The satellite also features the capability to provide a left and right looking sensor which is not available on most other SAR satellites.

3.12.6 COSMO-SkyMED

The Italian Space Agency launched the first two satellites of the COnstellation of small Satellites for Mediterranean basin Observation (COSMO-SkyMED) in 2007. It followed this with two more satellites launched in 2008 and 2010 to form a constellation of four medium-sized SAR satellites. The satellites all form the same orbital plane and are sun-synchronous, polar orbiting X-band 9.6 GHz dual-polarization capable sensors. They orbit at an altitude of 619 km with an orbital period of 97 minutes and repeat cycle of 16 days. Sensors 1, 2 and 4 are all offset by 90° from one another whilst Sensor 3 is offset from Sensor 2 by 67.5° providing varied intervals between satellite acquisitions along the same ground track (between 1 and 15 days difference).

Table 3.1. Comparison of the various SAR satellites both historic and currently operational. The table includes resolution modes that are most applicable to SAR imaging for small and large MDA applications.

Attributes	ENVISAT	SENTINEL-1A/B	RADARSAT-2	TERRASAR-X	ALOS-2	COSMO-SkyMED
Agency	ESA	ESA	MDA/CSA	Astrium/DLR	JAXA	MDA/CSA
Launch date	1 March 2002	3 April 2014/22 April 2016	14 December 2007	15 June 2007/21 June 2010	23 May 2014	8 June 2007/2008/2009/2010
Sensor band/bandwidth	C-band / 5.331 GHz	C-band / 5.405 GHz	C-band / 5.405 GHz	X-band / 9.65 GHz	L-band / 1.270 GHz	X-band / 9.6 GHz
Altitude (km)	790	693	798	514	628	619
Orbital period (minutes)	101	98	100	95	97	97
Repeat cycle (days)	35/30	12/6	24	11	14	16
Fine mode res. [rn. (m) × az. (m)] @ swath width (km)	[28 × 28] @100	[5.0 × 5.0] @80	[1.6 × 0.8] @18	[1.2 × 1.0] @10	[3.0 × 1.0] @25	[1.0 × 1.0] @10
Wide mode res. [rn. (m) × az. (m)] @ swath width (km)	[150 × 150] @400	[93 × 97] @400	[81 × 30] @300	[16 × 16] @100	[100 × 100] @490	[100 × 100] @300
Interferometry	Repeat pass	Repeat pass	Repeat pass	Single & Repeat pass	Repeat pass	Repeat pass
Polarimetric modes	Dual	Dual	Quad	Quad	Quad	Dual

CHAPTER 4 SHIP DETECTION IN SYNTHETIC APERTURE RADAR

4.1 CHAPTER OVERVIEW

Medium resolution SAR imagery covers ocean large areas but this comes at the expensive of reduced resolution. An operator searching through a SAR image covering millions of pixels and for ships which are approximately 10 pixels long can be time consuming and error prone. To aid in the development of a working SAR monitoring platform automatic ship detection methods are necessary to provide reliable and consistent results to better assess a given areas maritime domain [18, 55, 17, 3, 4]. Medium resolution SAR imagery is of particular importance as it can be used to gauge areas where illicit fishing activity is occurring [17] thus allowing higher resolution SAR imagery to be targeted a specific areas.

Ship detection in SAR imagery consists of several steps, each intending to narrow down the list of possible targets for the next [18]. A number of ship detection configuration exist, with the most common shown in Figure 4.1. SAR images are preprocessed to remove artifacts and land areas so that the prescreening stage can detect pixels that are brighter than the background at sea. The ship discrimination step then uses additional techniques to group these pixels and discriminate between areas that are ships and ones that are look-a-likes. Ship discrimination generates a list of likely ship positions which are sometimes fed into auxiliary processes such as operator validation, ship attribute (length, width, bearing, etc.) extraction or classification of ship type. For the purpose of this study only ship detection up to the discrimination step will be described in detail with a focus on intensity-based ship detection methods. The detection of wakes is an important topic in SAR ship detection [18, 56]

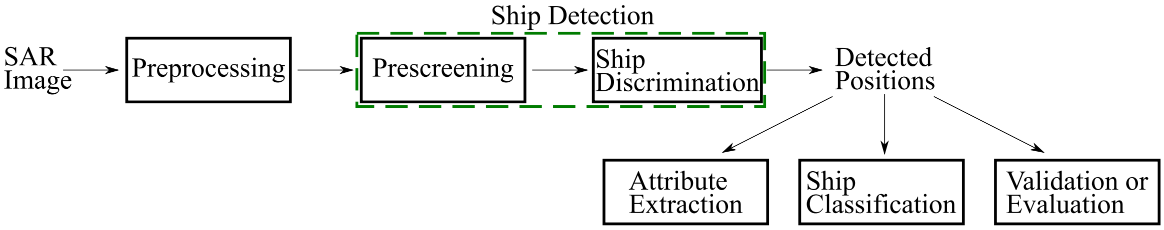

Figure 4.1. The common steps for ship detection in SAR imagery. The initial steps prepare the image into a standard from which it is then prescreened to detect possible targets. A ship discrimination step uses additional methods to discriminate ships from ship-like targets and, generally, provides positions of likely ship targets. Additional steps can include operator validation, attribute extraction and classification into various classes.

but is not the focus of this study due to inherent problems such as stationary ships, variable wake lengths and shapes, and strong reliance on sea-state and ship parameters [18].

4.2 PREPROCESSING

One of the most important steps in automatic ship detection is that of preprocessing [18, 57]. It largely determines the results of the subsequent steps. The most important aspect of this step is the ability to generate consistent processed SAR imagery for the prescreening and discrimination steps. By ensuring that the output is as uniform as possible subsequent steps should have fewer errors to deal with. Preprocessing generally involves signal and image processing techniques to enhance the image in a number of ways and like the other steps often has a trade-off between complexity, reliability and performance/accuracy.

Two assumptions need to be stated: it is assumed that all of the processing on the SAR imagery is done on the intensity images only because the phase is not exploitable on a per image basis and changes in sea-surface conditions vary significantly between repeat-pass SAR acquisitions. Second, it is assumed that the work here does not rely on polarimetric data. Whilst a lot of research has gone into the detection of ships in polarimetric data [18, 50, 58], such data is typically not available for medium resolution SAR imagery (at least fully polarimetric data) and the scope of such detection methods is beyond the scope of this study.

4.2.1 Speckle removal

Speckle is a major source of errors in both high and lower resolution SAR imagery. It is especially a problem for MDA applications where speckle interferes with the ocean background or clutter statistics and can appear as ship-like entities in low-to-medium resolution SAR imagery [18, 17, 57, 3]. The amount of speckle in a SAR image is estimated using a uniform image area and pixel intensity values and is often termed the Equivalent Number of Looks (ENL) [46, 59]. In SAR image processing literature there are two primary ways in which speckle is reduced: non-coherent/multi-look integration or adaptive spatial-based filtering [46].

As discussed previously, multilooking is the process of dividing the bandwidth of the azimuthal spectrum into L looks which form L independent images of the same scene. These are then incoherently averaged to reduce the speckle noise but at the expense of degrading the image resolution [46, 59].

Adaptive Spatial filtering are another technique often used for the filtering of speckle in SAR imagery using box-statistic filters. These make use of local variations in the data and use well-studied statistical image properties to reduce the effects of speckle. Spatial speckle reduction falls into two broad categories, namely Minimum Mean Squared Error (MMSE) such as the Mean, Frost, Lee or Kuan speckle filters [46, 47]; or Maximum a posteriori (MAP) based filters such as Gamma-Gamma speckle filters [60]. The filters remove speckle based on the assumption that it can be separated from the sea-clutter but do so based on a fixed (or variable) neighborhood size which degrades the spatial resolution of the SAR imagery.

The various filters each have their own trade-offs and benefits. For instance, the mean box filter might, on average, exhibit the best speckle reduction across a wide variety of samples but might do so at an increased loss of spatial resolution compared to the other methods. The Frost filter has excellent resolution preserving capabilities but speckle is not reduced as prominently. This all comes at the expense of increasing complexity which might not satisfy certain operational requirements. It should be noted that most SAR satellite providers distribute multilooked speckle-reduced products as part of their ground range detected products. This reduces the processing requirements on the user's end but does so at the expense of flexibility in choosing which speckle reduction technique is used.

4.2.2 Image Calibration

Image Calibration is the process of calibrating the image in terms of real-world positioning and radiometric properties. The process of image calibration takes into account two main factors, georeferencing and radiometric calibration. Uniform image calibration is essential to reproduce results and interpret results across studies.

Georeferencing is the process of geolocating every pixel within a SAR image to a point on the Earth, thereby assigning real-world coordinates to points [59]. This is usually done using either the known corner coordinates of the image or predetermined ground control points which typically accompany the SAR image as metadata. Often an initial run determines a pixel's rough accuracy with subsequent refinements created by an iterative procedure utilizing a precise orbital state vector (also provided as metadata with the SAR imagery). Geocoding refers to the process of ensuring the image is placed so that north is facing upwards. Finally, registration is the process of geolocating two images precisely in order to allow for comparisons between images in a meaningful way and also utilizes the orbital state vector data as discussed before. Some studies have shown that using precise co-registration artifacts in the sea can be reduced using multiple acquisitions over a longer time period [51].

Radiometric calibration is the process of converting the native SAR imaging readings into standardized geophysical units of measurement, normally known as the scattering coefficient σ_0 expressed in decibels. This represents the normalized radar cross section (RCS) per squared meter and is dimensionless. Radiometric calibration is important as it ensure that data can be compared between sensors, times and positions. The process of calibrating an image in terms of σ_0 is dependent on the incidence angle, wavelength, polarization and the ship/object's scattering properties. Other more uncommon forms of radiometric calibration include those based on radar brightness which is derived from the digital number inherent in some SAR products and is generated by applying a calibration factor [61].

4.2.3 Land Masking

Land masking is an important step in preprocessing SAR data as it determines how close results can be to the shoreline. Land areas can cause detection results because they typically produce backscatter that is higher due to the specular nature of land areas compared to flat ocean areas. Land masking essentially removes land in the processed SAR image and uses shapefiles of the coastline to remove the land. Alternatively, the coastlines are detected using automatic methods and then the same masking procedure is applied as with shapefiles [62]. In either case, a buffer zone determines how close to the shore the results can be relied upon and which determines the ability of the subsequent steps to detect ships in harbor/near shore areas [18].

4.2.4 Ambiguity Removal

Another common occurrence in SAR imagery is that of azimuth and range ambiguities. The removal of ambiguities forms a large part of research and typically involves using the SAR acquisition parameters such as PRF, satellite velocity and target range distance. These are used to predict the position of likely weakened and repeated “ghost” copies of the original highly reflective target. Additionally concepts such as repeat-pass ambiguity removal are also sometimes applied to SAR data [57, 51].

It is assumed that the techniques described and data used in this study have been done to an accuracy that will not hinder ship detection in medium resolution SAR imagery. As the only data available for this study is already multilooked this is the chosen form of speckle reduction with any latent speckle dealt with by the following steps. The image calibration should ensure that the data is radiometrically calibrated to σ_0 and georeferenced to within 1 pixel accuracy (platform resolution dependent). It was assumed that a buffer of 1 km would suffice as a land masking buffer and that any ambiguities not removed in the preparation of the satellite product by the satellite provider would be dealt with during prescreening and discrimination.

4.3 PRESCREENING

One of the primary steps in ship detection literature is that of ship prescreening [18, 63, 64, 17, 3]. The prescreening step is often combined with the discrimination step to form a single detection step. This is usually done for efficiency reasons as SAR images can be extremely large with sizes up to 52400×37200 pixels [65], depending on image resolution.

When the SAR image is properly calibrated and georeferenced then the next step is to generate likely targets. These targets are identified using a threshold across the image which splits the image into ships and non-ships. Due to the inherent property of these binary decision detectors which require a trade-off between detection accuracy and false alarm rate choosing a single threshold parameter that provides both a high detection accuracy and a low false alarm rate can often not be achieved. To this end, many SAR ship detection systems [18, 64, 17, 66, 67, 68, 69, 65] split the prescreening and discrimination phases of ship detection. Prescreening typically involves image processing and statistical methods on SAR intensity imagery to identify areas that likely contain ships. Discrimination then uses these results as input to discriminate ships from ocean-clutter and SAR artifacts using wide variety of science disciplines to identify false alarms. Prescreening methods fall into three broad categories, namely global, local and other, discussed next.

4.3.1 Global thresholding

Global prescreening methods take the entire SAR image and use a single value to threshold every pixel. These methods have historically been one of the first methods used in ship detection problems [18, 70, 56]. They provide a basic means of identifying bright areas in SAR imagery that can be implemented in an efficient parallel manner. A single threshold value is computed in some manner, such as using histogram percentiles, and every pixel in the image is compared against this threshold to determine if it is bright or not [18, 71]. The higher the threshold value the fewer false alarms but the possibility of missing a ship increases. A fairly successful recent application of historical global thresholding for prescreening and detection uses the Otsu's gray level thresholding to identify the threshold which partitions the ships and ocean clutter with maximum inter-class variance [72, 69]. Another approach normalizes the RCS of the pixels in the SAR image and then applies an empirically chosen single threshold to this image to identify ships [56].

The application of a single threshold value to an entire image can lead to efficient solutions but typically does not have the discriminatory power to separate ships in areas of both high and low contrast and is especially a problem in SAR imagery which exhibits a wide range of values between the near and far range known as the high dynamic range of SAR [18, 37, 39]. Research has shown that ship prescreening using global thresholding typically incurs orders of magnitude more false alarms [18, 3, 4] and requires a specially customized discrimination step to be successful [69].

4.3.2 Local, adaptive thresholding

Ships contain metal which reflect most of the transmitted radar signals back to the sensor and hence ships appear as high backscatter bright areas in SAR imagery compared to ocean areas. It is assumed that the backscatter around the ship is lower than the ship's backscatter or else it would be invisible/appear as ocean backscatter. Sea-surface conditions often vary from one end of the SAR image to the other and so a single global threshold usually does not provide the discriminatory power to separate ships in ocean areas with high and low sea-surface roughness [18].

Instead of comparing each pixel to a single global threshold researchers noted that the brightness of pixels relative to its surroundings was a key to separating high backscatter targets in areas of both high and low backscatter background returns. This led to the development of Constant False Alarm Rate (CFAR) prescreening [18, 17, 63, 70, 66, 67, 73, 74, 75]. CFAR uses a collection of two neighborhoods around a set of pixels to determine if this area has a higher local-relative backscatter than its neighbors. The CFAR algorithm ensures a constant level of false alarms by using a selected probability of false alarm (P_{fa}) to calculate a varying threshold on a per-region-of-interest basis. The surrounding neighborhood distribution and current area of interest are compared and the area is deemed bright if it is an outlier to the expected (background) distribution. The probability of false alarm sets a hard limit on the threshold T which in turn determines how many times brighter a given pixel needs to be than its neighbors to be identified as a ship. The adaptive nature of the method ensures that the number of false alarms is equal to or less than P_{fa}, hence ensuring a constant (expected) number of false alarms. Instead of specifying a required P_{fa}, a custom threshold T is sometimes chosen in order to prevent cases where both the number of true positives and false alarms cannot be met by the automatically calculated P_{fa} [76, 77, 78, 79, 79]

Research into CFAR prescreening is split into two major areas, modeling of the sea/ship distributions [18, 80] and the comparative manner in which these are used [18, 64, 79, 81]. The most common assumption for the sea-clutter distribution is known as the K-distribution. This models the water using a Gaussian distribution modulated by the mean of the amplitude data which itself is modeled by a Gamma distribution [18, 33]. Other distributions often associated with SAR ocean-clutter are the Rayleigh, Alpha-stable, Generalized Gamma distributions [18, 33, 82, 83]. Non-parametric type methods such as the Parzen-window Kernel-based sea-clutter distribution estimation tries to adaptively model the underlying distribution [84]. Most distribution modeling research in SAR imagery focuses on the sea-clutter but some research has gone into modelling the ship's backscatter distribution using the ship's physical properties [80].

The most widely used, Cell-Averaging CFAR (CA-CFAR) calculates the clutter mean and then compares the region of interest to this value to see if its T times brighter than this mean [18, 64, 17, 77, 3]. Initially, clutter was assumed homogeneous where CA-CFAR could potentially provide an optimal comparison statistic [64, 81] but this assumption does not always hold true. Additional methods were developed to incorporate heterogeneous distributions and hence are typically better at detecting bright areas for conditions [76]. The two most widely used examples of these methods are the Greatest-Of and Smallest-Of CFAR (GO-CFAR and SO-CFAR respectively) which check if the current pixel value is T times the largest or smallest pixel value in the surrounding area. Other heterogeneous CFAR methods exist such as Order-Statistic (OS-CFAR), Switched OS-CFAR (SWOS-CFAR) and Generalized Switching (GS-CFAR) each with their own advantages and disadvantages which broadly reorder the clutter samples in various ways and compare the test area to this reording [64]. Finally, a recent paper uses SAR imagery metadata to adaptively vary which CFAR method is used on a per resolution and region basis [85] which provides an excellent source of prescreening but does report processing times of hours per image for some of the methods used.

4.3.3 Other prescreening methods

While CFAR and global thresholding methods are the most ubiquitous means of prescreening an image, a number of other methods can be used - ranging from image processing to machine learning. The Wavelet analysis has played a major role in SAR prescreening due to its ability to identify signals in SAR imagery at various rotations and scales [18, 86]. One other prominent example of prescreening is the creation and thresholding of a Rice Factor image which is the coherent to incoherent received power ratio [87].

Prescreening largely determines the overall accuracy in ship detection systems. Global or locally adaptive thresholding methods with parameters set too stringently can fail to identify all possible ships in a given SAR image. Global methods introduce orders of magnitude more false alarms at lower thresholds than locally adaptive methods but can have the advantage of being more efficient solutions.

The selection of which CFAR method is largely based on the images to be processed. In most cases a single CFAR method can suffice for a single SAR dataset but the requirements become difficult to meet when the CFAR method is applied to a SAR dataset that varies in terms of sensor, polarization and resolution. To this end, and discussed in the next chapter, the simplest CFAR method is usually chosen and emphasis on reducing false alarms (assuming all ships are detected) is placed on the ship discrimination step.

4.4 DISCRIMINATION

A common strategy for ship detection is to initially highlight as many likely targets as possible from the entire SAR image using one specialized step and then following this up with a secondary step which works within the reduced search space to identify features correlated with ships. Ship discrimination is typically referred to as the high-level classification stage in ship detection literature [18, 64]. For the purpose of this thesis ship discrimination forms the last part of the ship detection procedure. Its goal is to identify positions of ships in the SAR image whilst reducing the number of false alarms presented to it by the prescreening step. The discussion of ship discrimination can be split into three areas - classical-; frequency-; and machine learning-based ship discrimination.

4.4.1 Classical ship discrimination

The first method ship discrimination strategy is to vary the P_{fa} or custom threshold in a conventional CFAR method [18, 64]. This approach can provide acceptable results but may fail on larger SAR datasets [88]. This can be improved by breaking the symmetry around the parameters by creating a cascade of CFAR thresholds, each tuned to remove different false alarms than the last [67]. Some methods use CFAR in a hybrid prescreening/discrimination stage by first estimating the underlying distribution using Kernel Density Estimation (KDE) and then using this as input into a conventional CFAR as the discrimination step [63].

Other CFAR-based discrimination methods create an intermediary image or representation as part of the prescreening step and then use CFAR to identify ships. For example, ships in both high resolution and lower resolution SAR imagery are often immediately apparent to an observer because of the difference in contrast between the relatively dark sea area. A saliency map is a computer vision construct which emphasizes salient objects and de-emphasizes other aspects within an image. Two examples of this in SAR literature include the creation of a saliency map using image processing [5] and machine learning techniques [89]. A local thresholding approach is applied as discrimination in the former [5] whereas the latter uses a specially adapted CFAR known as the Signed Pressure Function CFAR to the saliency map to identify ships from false alarms [89].

Another ship discrimination approach is that of clustering-based methods. These separate ships from false alarms by discriminating based on ship properties such as size, density and shape. Size-based methods use connected component analysis and then remove false alarms based on logical maximum ship sizes [90, 75]. For instance, one approach uses connected component clustering with a minimum size T_{CL} followed by position estimation of likely azimuth ambiguities [80]. Morphological operations feature in discrimination literature with the aim of using common operations such as erode and thinning to remove connected pixels and identify clusters of pixels more likely to be ships [70, 75]. Traditional clustering methods are also sometimes employed as additional discrimination after morphological processing such as k-means [85] or mean-shift [6] or more recently superpixel segmentation [91]. Superpixel segmentation is particularly interesting as the final stage of the discrimination step uses additional local and global contrast thresholds to identify pixel segments likely to be ships [91].

4.4.2 Frequency-based ship discrimination

Another popular form of discrimination uses the assumption that the frequency components of false alarms exhibit different properties to those of ships. Conventional filtering techniques such as notch filtering have been shown to provide acceptable results but only with high resolution imagery [58]. The most common form of frequency processing for ship discrimination is Wavelet filtering. Wavelets extract detections using filter banks attuned to certain signal properties such as frequency and rotation. One of the first uses of Wavelet processors to SAR imagery used it as a combined prescreening and discrimination stage [86, 92] whereas later attempts used it solely during discrimination [66]. A more recent advancement applies Gabor Wavelets to the output of a CA-CFAR prescreened SAR image. Gabor Wavelets allow for infinitely many scales, rotations and frequencies enabling more flexibility in the filter bank configuration compared to previous Wavelet discriminators [7].

4.4.3 Machine learning-based ship discrimination

Machine learning methods have been used for ship discrimination since at least [18, 93]. These ship discriminators are trained on data to identify salient characteristics of ships. These characteristics can range from size features to textures or backscatter composition.

Machine learning ship discrimination most commonly uses either Neural Networks (NNs) [18, 93, 88] or Support Vector Machines (SVMs) [94, 95, 96]. Classical NNs were one of the first types of machine learning ship discriminators used [93]. More recent developments have used SVMs as they can model the separation between false alarms and ships better using the kernel method [94, 95, 96].

The training of neural networks is an important aspect of the ship discrimination as it can affect the performance. SVMs often use a constrained minimization procedure [95] whereas there have been multiple studies into using alternative means of training NNs, specifically for ship discrimination. These often take the form of evolutionary algorithms. These, too, are minimization procedures but take inspiration from real-world biological processes to train the NN. Examples of these types of algorithms applied to SAR imagery for ship discrimination include Genetic Algorithms (GA) and Ant Colony Optimization [93, 97].

While SVM now play a large role in ship discrimination, interest in traditional NN architectures have been renewed by extending them in depth. This recent advancement has been called deep learning and is the next step in the evolution of machine learning. In classical machine learning features are hand picked from an initial limited set of calculated features and the combination of these features with the best performance is chosen as the final set of features for discrimination. This process is known as feature engineering and deep learning forgoes this step by placing the responsibility of finding the best set of features on the network during training from a much large initial feature set. Initial tests indicate promising results [88] but further studies are required to understand the long term efficacy of this new form of NN for ship discrimination in SAR imagery.

4.5 SHIP DETECTION CONSIDERATIONS

In the addition to the above, some practical issues need to be addressed. This section will describe some of the pertinent issues, which types of SAR data these affect and how they are typically addressed.

4.5.1 Effectiveness of bands on maritime monitoring

SAR that is available commercially has 3 common bands, namely X-, C-, and L-band. These bands each interact differently to maritime conditions and the choice of which band to use for maritime monitoring (ship detection and environmental monitoring) has been studied extensively. The choice of which band largely depends on application but some broader findings are available to help choose the most effective band. X-band is highly sensitive to atmospheric effects [98] where initially L-band was shown to have difficulty enhancing maritime objects of interest such as oil-slicks [99, 100]. More recently, however, polametric L-band processing has shown improved performance for oil-slick detection [101, 102]. For general maritime monitoring C-band seems to be the most common choice as it shows strong contrasts at sea when wind speeds are below 14 m/s [103]. It also maps shorelines more accurately than the other bands [104]. Finally, C-band has shown excellent performance for bilge-dump detection [105] and ship detection in a number of scenarios [18, 3, 4]. For this reason ENVISAT, RADARSAT-1, RADARSAT-2, SENTINEL-1A and SENTINEL-1B all carry or carried a C-band sensor for general maritime operation [57]. The agreement to use C-band sensors across multiple satellites and providers built with MDA applications in mind indicates that C-band is a suitable SAR sensor band for monitoring MDA.

4.5.2 Data Availability

A significant issue faced when using SAR imagery for maritime monitoring and specifically for ship detection is data availability. There are two aspects to this discussion - the accessibility of SAR data and the repeat/revisit times and matching of this to auxiliary ship data such as AIS transponder data.

Historically, SAR imagery has been particularly difficult to obtain due to high data costs. In 2014 ESA announced that the Sentinel program will allow free and unlimited access to all satellite imagery taken by any of the Sentinel missions. In particular, Sentinel-1A/B is now freely available to anyone with an internet connection. The downside of this is that specific mode and area acquisitions are not possible without a formal agreement with ESA. To obtain specific imagery over specific areas for operational usage taskable satellites are necessary such as RADARSAT-2 and TERRASAR-X. For this study, both freely available (Sentinel-1A) and taskable satellite data (RADARSAT-2) are used.

All SAR satellites have a finite power consumption limit [37, 57] and as such only certain modes are used at certain times. Furthermore, the speed of the satellite is finite and thus it takes a finite time to revisit a specific area. For operational ship monitoring this can be a problem, specifically if the area of observation is small. This problem can be alleviated by using multiple satellites in tandem to observe an area. A recent study has calculated that for a given area using high resolution satellite data from COSMO-SKYMED and RADARSAT Constellation Mission (RCM) the combination could achieve a mean revisit time of 7 hours [42]. In addition to this, the study also showed that matching AIS data for the same region could be acquired within 25 minutes of the SAR acquisitions [42].

4.5.3 Resolution on ship detectability versus swath width

A major concern for any ship detection system is that of the swath width/image resolution trade off. Current SAR systems can either observe a small area with very high resolution imagery or a large area can be monitored at a much reduced resolution per pixel. Advances in SAR technology and processing has seen an improvement for low-to-medium resolution SAR imagery but there is still a fundamental limit that needs to be addressed which is called the minimum mappable unit (MMU). Ships smaller than a given ground resolution may be invisible in that pixel depending on how the subscatters combine during processing. Due to the likelihood of speckle a single pixel may appear bright yet not contain any ship. To distinguish within a single pixel and speckle requires highly accurate, timely auxiliary knowledge such as AIS. Even with this auxiliary knowledge SAR imagery tries to fill gaps which cannot be achieved using transponder data (i.e. dark targets) and as such it is assumed that a ship is only detectable if it occupies a MMU of two or more pixels in the GRD type imagery. This limit affects the minimum pixel size a ship needs to occupy and thus a ship needs to be approximately two pixels long in either length or width to be detected. Methods of detecting ships smaller than this in medium resolution imagery are out of scope of this study. The minimum ship size, however, largely depends on the preprocessing steps taken before the ships are detected. For GRD imagery preprocessing steps such as main lobe focusing/side-lobe reduction and multilooking to reduce speckle play a large role in determining the final size in pixels a ship occupies in a SAR image versus its actual size on the water. To this end the minimum detectable ship size will depend on the SAR sensor and its ability to discriminate small bright scatterers during RAW to SLC conversions and then SLC to GRD conversions.

4.5.4 Medium resolution imagery for ship detection

A number of new studies are focused on ship detection using Sentinel-1 imagery with focus on Interferometric Wide swath (IW) Single Look Complex (SLC) imagery type [106, 107]. SLC imagery has been shown to have excellent ship detection performance due to the increased spatial resolution [106] and similar results occur for other SLC-type satellite sensor imagery such as RADARSAT-2 and TERRASAR-X too [50, 108, 106, 107]. While SLC high-resolution imagery is particularly good at detecting ships as they are highly reflective targets spread over hundreds of pixels they do so with a reduced swath width.

Whilst some research has been done into Extra-Wide swath (EW) mode imagery for Sentinel-1 ship detection [106, 57], current studies could be improved by study into this image type over a specific study area, where and why false alarms occurred, how parameter adjustments might affect performance, few comparisons between sensors/resolutions and as-of-yet no definitive comparison among current state-of-the-art ship detection methods have been made for this type of imagery [106, 109, 108]. To this end Sentinel-1 EW imagery has much larger swath widths which is specifically useful for monitoring South African waters. South Africa's EEZ covers more area than its land and these vast areas cannot be properly monitored using Sentinel-1 IW imagery (due to the reduced swath width). The ESA has also deemed South Africa and its waters a calibration site for the Sentinel-1 mission and is currently one of the few areas where EW imagery is being acquired near a coastline and is not related a sea-ice zone [110].

Additional research effort into various ship detection methods for SAR imagery includes the usage of TerraSAR-X [63, 50, 111, 107, 73], RADARSAT-2 [112, 113, 114, 115] and CosmoSkyMed [113] satellites. These satellites provide additional modes and resolutions not necessarily available on Sentinel-1 but the data are not free. Focus on these satellites often also uses full- or quad-polarimetric information which can require specially developed ship detection methods to use [50, 58, 116, 117]. While the Sentinel-1 EW imagery does not provide full polarimetry, dual polarimetry allows for double validation of targets and provides additional opportunity to identify polarizations which provide improved ship visibility over others [27].

4.5.5 Ship detection performance metric coherence

There is a lack of coherence among the different performance metrics and their usage within the ship detection community. Across a number of recent studies there exists a multitude of ways to report results, with few similarities between the methods [50, 63, 115, 111, 58, 106, 73]. In addition, the way in which performance is measured varies from study to study and the results need to be critically evaluated before presenting methods as better or worse [118]. In one study [106], the authors state that AIS ship transponder information is used to verify detections. The authors go on to state how SAR ship detections that do not have matching transponder information are disregarded [106]. While this can be used to give a general idea of performance, it completely negates the usefulness of SAR imagery which can circumvent ships that switch off their transponders [17] and could fail to detect any potential ships in an image if useful AIS data is not acquired for a given SAR image. In another study [50], the authors provide a much more comprehensive set of ground truth data including both visually inspected and AIS matched ships but fail to describe the total number of false alarms not related to ambiguities their ship detection method incurs. Another aspect that is rarely described is the reconstruction performance of the ship detection method. Subsequent stages might require improved ship reconstruction to estimate various parameters of the ship and the lack of performance metrics to assess reconstruction performance is another limiting factor in current ship detection studies. With the lack of a single common, complete SAR data set and the difference in performance metrics available, comparison between methods developed by different authors becomes even more difficult.

4.6 CONCLUSION

Over the course of this chapter a number of research opportunities were identified. To better focus the study going forward the following provides a list of these.

- **Focus on high resolution SAR imagery**

  High resolution SAR imagery often receives research priority over lower resolution imagery due to more detailed ships within which implies smaller ships can be tracked. Furthermore, ships in high resolution imagery have more data associated with them which can mean more descriptive features can be formed which may aid in detection, discrimination and classification tasks. All of these attributes dictate that new ship detection methods are primarily aimed towards higher resolution SAR imagery.

- **Lack of ship detection research on Sentinel-1 EW imagery**

  Sentinel-1 imagery provides a free-to-use source of SAR imagery. Most focus on SAR ship detection for this data has been on its higher resolution imagery but EW imagery also provides a source of data for lower resolution ship detection research that could supplement the high resolution information.

- **Small versus large dataset**

  Smaller datasets are often used in lieu over larger, more varied datasets, primarily due to the extensive costs involved in acquiring many SAR images. Whilst smaller datasets provide good initial indications of possible performance, their smaller sizes do not present a representative population. Smaller, less varied datasets therefore call into question the statistical significance of any results obtained. Finally, larger datasets can better represent operational situations, which may be a deciding factor when selecting a ship detection method.

- **Medium resolution SAR machine learning**

  Medium resolution SAR imagery provides capabilities to detect ships at sea but those ships are in the order of 5-7 pixels long [4]. This makes applying any machine learning to SAR imagery complex without appropriate considerations. Furthermore, in the field of machine learning benchmark datasets are readily available to method designers to directly compare methods against one another. This trend has not yet carried over to the SAR machine learning research.

- **Metric and reporting inconsistencies**

  CFAR-based methods are known as binary decision classifiers and one of their primary principles is the trade-off necessary between false alarm reduction and true positive retention. This trade-off manifests differently in SAR ship detection compared to other areas of research due to the large discrepancy between the number of ships and ocean pixels in wide-swath SAR imagery. This means that the metrics and the way in which they are reported need to be carefully considered to provide a clear picture of the results. In addition to this, different studies report with a variety of different metrics which can make comparisons a complex task.

- **Lack of use of auxiliary data**

  Transponder data is often used as a means of verifying ship detection results and extracting ship types from correlated SAR and transponder detections. This ignores the wealth of information present by using this data as long-term distribution analysis data (i.e. *a-priori* data). Auxiliary data, such as historical transponder data, is rarely used as part of the detection stage.

- **Minimum ship size detectability**

  Special considerations need to be made in order to understand and cope with the minimum detectable ship sizes imposed by using medium resolution data. For instance, methods that work on high resolution SAR ships with hundreds of associated pixels do not necessarily translate to medium resolution SAR ship with many fewer pixels per ship.

- **Preprocessing, data types and sources of error**

  Data type conversions, preprocessing and SAR image peculiarities can all possibly describe errors in SAR ship detection but are either assumed as known or occasionally not described at all. A common source of many SAR errors, for instance, is the conversion from SLC type data to GRD type data and the effects these conversions have on SAR ships and artifacts. If GRD type data is the only type available (such is the case with Sentinel-1 EW imagery) special attention needs to be paid on what effects this may have on SAR ship detection performance.

Research into ship detection has yet to find the optimal detector and with new data constantly becoming available ship detection is an active area of research in the geoscience and remote sensing community.

This chapter analyzed the various literature related to SAR ship detection and described the most common steps found. The first step, preprocessing, ensures that data are of a consistent and standard format when presented to the next steps. Prescreening methods were discussed and it was shown that CFAR plays an important role as the initial stage in many ship detections systems. Once initial targets are identified by the prescreening then various ship discrimination steps can be used to isolate false alarms. The following chapters described two novel methods developed for this study and the data they were tested against.

CHAPTER 5 ADVANCED SHIP DETECTION

5.1 CHAPTER OVERVIEW

Two novel ship detection methods are introduced in this chapter aimed to address some of the identified shortfalls in the SAR ship detection literature. An overview of the ship detection process is given followed by a mathematical description of the basic CFAR prescreening method. This is followed by a novel extension to CFAR for per-pixel thresholding control as in [3]. This extended CFAR method is then used to threshold a SAR image based on a ship distribution map and initial detections using an optimisation procedure known as Simulated Annealing (SA) [3]. A second method, introduced in [4], is also described which uses a low-threshold CFAR prescreening step to derive initial detections which are then fed to a Haar-like feature extraction step. These features are fed into a cascade classified trained to help identify ships from false alarms in a rapid, consistent manner.

5.2 SHIP DETECTION OVERVIEW

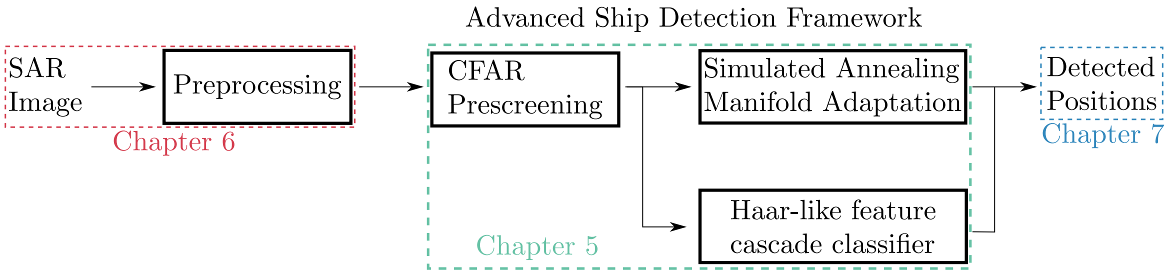

Figure 5.1. The first step, preprocessing is discussed with the creation of the SAR dataset, as described in Chapter 6. The next two stages, prescreening and discrimination, are discussed in this chapter. Chapter 7 deals with the results obtained and a discussion thereof.

With over 100 000 ships active at any given point in time in the ocean [1], the detection of ships using any means possible is important. Maritime surveillance can be accomplished by processing SAR imagery using a multistage approach whereby each stage provides ever stricter requirements on the ships that are accepted [18, 66, 64, 119, 6, 67, 74]. Figure 5.1 gives an overview of the ship detection system used in this thesis. It was assumed that no differentiation between ships and other bright targets are made and that the ship detection methods presented here can be extended using auxilarily information as additional processing step to separate ships and other targets if necessary.

The first stage of most ship detection systems is data acquisition and preprocessing, Figure 5.1. These steps are discussed further in Chapter 6 which describes the SAR dataset and preparation used in this thesis. As a brief introduction the preprocessing stage completes two tasks - the first is the removal of land from the image and the second is radiometric calibration. Land removal is done in order to prevent incorrect detections over land as well as to reduce land azimuthal ambiguities near the coast. Radiometric calibration is put in place so that detections between various acquisition modes are compared using a similar basis. Additional preprocessing steps involving filtering were not applied in order to reduce the possibility of altering the sea clutter statistics as well as to prevent the removal of small ships within the SAR imagery.

Prescreening and ship discrimination stages are the stages described in this chapter. Prescreening uses a form of local thresholding to identify a list of bright objects in a SAR image that may be a ship or a false alarm. The prescreening stage is applied to reduce the large discrepancy between the number of ships and the number of sea pixels used in the subsequent detection process. This effectively reduces the input search space for the discrimination stage. The discrimination stage's primary goal is to use various methods to learn when a sample is a false alarm and when it is a ship, thereby reducing overall false alarm rates while trying to maintain a high level of detection accuracy.

5.3 CFAR SHIP PRESCREENING

5.3.1 Conventional CA-CFAR

The first true detection stage in most ship detection systems is the prescreening stage. A commonly used variant of the CFAR method is known as the Power Ratio (PR) or Cell-Averaging CFAR (CA-

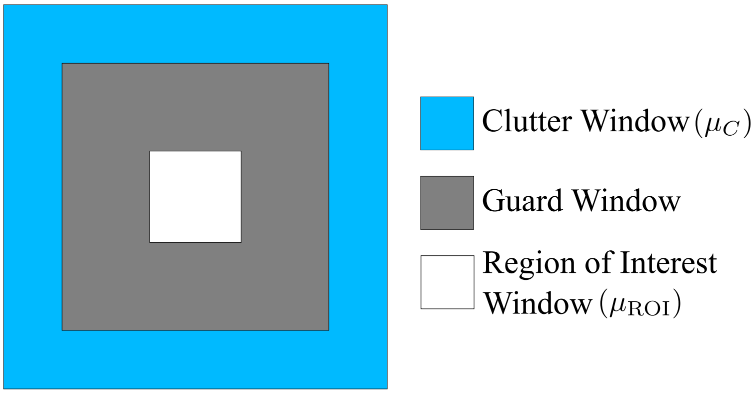

Figure 5.2. A CFAR window configuration. The mean pixel value inside the clutter and ROI windows are μ_{C} and μ_{ROI}, respectively. The clutter window is used to represent each pixel's mean ocean backscatter or clutter level. The guard window is there to prevent corruption of the clutter mean by objects larger than the ROI. Only ROIs where $\mu_{\mathrm{ROI}} > \mu_{\mathrm{C}} \times T_{\mathrm{C}}$ are selected as bright pixels. The sizes of the windows are defined as squares with lengths S_C, S_G, and S_{ROI} for the clutter, guard and ROI, respectively.

CFAR) [18, 77, 17, 64, 67, 74]. It is based on a scalar threshold value which determines how much brighter a pixel must be compared to its local surroundings to be selected as a target or ship. All CFAR methods use a sliding window configuration, shown in Figure. 5.2, with this threshold to identify possible targets. A CA-CFAR prescreening stage compares the center region of interest's (ROI) window mean (μ_{ROI}) to the clutter's window mean (μ_{C}) with a guard window to prevent ROI value corruption of the clutter mean [3, 18]. As the window moves across the image, ROI pixels which are T_{C} times brighter than μ_{C} are marked as bright pixels in an output binary image $\mathbf{J}$. The threshold (or depending on the type of CFAR method the probability of false alarm P_{fa}) can either be a fixed constant or a two-dimensional manifold which can be varied across a SAR image (described in section 5.3.3. Among the benefits of the CA-CFAR prescreening stage is its low complexity and the ability to compute good initial estimates of the target without computing the probability density function (PDF) for each sub-window. The disadvantage of using a single scalar threshold to define the distribution of reflectance of the ocean that the distribution of the sea clutter can be heterogeneous which could cause the method to fail [64, 74].

Assuming an input SAR intensity image $\mathbf{I}$ and binary output image $\mathbf{J}$ with dimensions $X \times Y$ where $x = \{0, \ldots, X-1\}$, $y = \{0, \ldots, Y-1\}$ and $x, y \in \mathbb{W}$ such that $\mathbf{I}$ and $\mathbf{J}$ can be defined as in [3, 4] by

$$\mathbf{I} = \left\{ \left\{ I(x,y) \right\}_{x=0}^{x=X-1} \right\}_{y=0}^{y=Y-1} \tag{5.1}$$

$$= \begin{bmatrix} I(0,0) & \cdots & I(0,Y-1) \\ I(1,0) & \cdots & I(1,Y-1) \\ \vdots & \ddots & \vdots \\ I(X-1,0) & \cdots & I(X-1,Y-1) \end{bmatrix}, \tag{5.2}$$

$$\mathbf{J}(\mathbf{I},T_{\mathrm{C}}) = \left\{ \left\{ J(\mathbf{I},x,y,T_{\mathrm{C}}) \right\}_{x=0}^{x=X-1} \right\}_{y=0}^{y=Y-1}. \tag{5.3}$$

Where $T_{\mathrm{C}} \in \mathbb{R}$ is a scalar value known as the CA-CFAR threshold and is inversely proportional to the number of false alarm pixels permissible. The CA-CFAR binary pixel $J(\mathbf{I},x,y,T_{\mathrm{C}})$ and mean (power) ratio $\mu_{\mathrm{ratio}}(x,y)$ are calculated with

$$J(\mathbf{I},x,y,T_{\mathrm{C}}) = \begin{cases} \text{true} & \text{if } \mu_{\mathrm{ratio}}(x,y) > T_{\mathrm{C}} \\ \text{false} & \text{otherwise} \end{cases}, \tag{5.4}$$

$$\mu_{\mathrm{ratio}}(x,y) = \frac{\mu_{\mathrm{ROI}}(x,y)}{\mu_{\mathrm{C}}(x,y)}, \tag{5.5}$$

where $\mu_{\mathrm{ROI}}(x,y)$ and $\mu_{\mathrm{C}}(x,y)$ are known as the region of interest mean and clutter mean respectively and are calculated using the window system shown in Figure 5.2. Notice that the threshold T_{C} is a single value which acts equally on all pixel values, irrespective of pixel location within the SAR image. The above CFAR formulation is known as a custom threshold factor formulation of the CFAR method. In the classic formulation of the CFAR algorithm the threshold is adaptively calculated based on the clutter's assumed distribution but is still tied to a single, pre-selected fixed probability of false alarm P_{fa}. Formulating the CA-CFAR using equation (5.5) in [18, 77, 17, 64, 67, 74] affords us the ability to extend the fixed threshold or P_{fa} to adapt this value across the SAR image.

5.3.2 Alternative CFAR methods

In the CA-CFAR method clutter values not in the guard or ROI window are considered equally important and are compared to the ROI mean. By weighting each pixel equally no preference towards brighter or darker clutter pixels are given. Contrastingly, methods such as Greatest Of-CFAR (GO-CFAR) and Smallest Of-CFAR (SO-CFAR) use the the greatest or smallest pixel value in the clutter window. This value is then compared to the ROI in the same way for the different CFAR methods using a threshold T_{C}.

As mentioned in [64], SO-/GO-CFAR based methods tend to perform better when applied to heterogeneous clutter. These methods still use a single threshold or P_{fa} to calculate whether a pixel value is higher than the highest or lowest pixel value. It should be noted that whilst the CA-CFAR method is extended in the next section, a number of CFAR forms could also be extended. The CA-CFAR method used here could be replaced with the GO-/SO-CFAR based methods by changing how μ_{clutter} is calculated. The only constraint is that the chosen prescreening method identifies all the ships in the image with methods. This is most easily accomplished by using either a very-low threshold global thresholding method or a low threshold CA-CFAR but can also be accomplished using other CFAR variants with carefully selected thresholds. Due to the assumption that ships are at least as bright as their surroundings, the CA-CFAR method provides a method that will highlight all the ships with an order of magnitude fewer false alarms compared to global thresholding methods [18, 3, 4].

5.3.3 Extending CA-CFAR Prescreening

The conventional CA-CFAR method uses a single threshold value to determine if the current pixel ratio μ_{ratio} is a ship or not. If the threshold value is low, a vast number of pixels will be highlighted, many of which will be false alarms. If the threshold value is high then the number of false alarms will be significantly reduced but a number of valid targets will be ignored, causing a drop in detection accuracy. This makes the selection of T_{C} complex and made more so by the fact that a single threshold value, even when used to discriminate between local statistics of pixels, may not be sufficient to properly discriminate between similarly valued mean ratio values. Figure 5.3 presents an example of how a single threshold, described here as a flat manifold, can fail on occasions to properly discriminate regions with the same or similar μ_{ratio} values. Pixels that are brighter than their neighbors manifest as large values compared to others in the neighborhood. These high ratio values appear as spikes in the ratio image when $\mu_{\text{ROI}} > \mu_{\text{c}}$. Figure 5.3 shows an example of three such spikes found in a mean ratio image with two threshold manifolds overlaid - one flat and the other non-flat. A single-valued, flat manifold such as T_1 would not be able to differentiate the spikes two and three with the same value. With a flat threshold, either they are both accepted or rejected as bright ship pixels. If we assume that number three is a false alarm by extending the threshold manifold to allow for variations in the threshold value along the manifold the two spikes could easily be separated by increasing the threshold over the one that is not a ship.

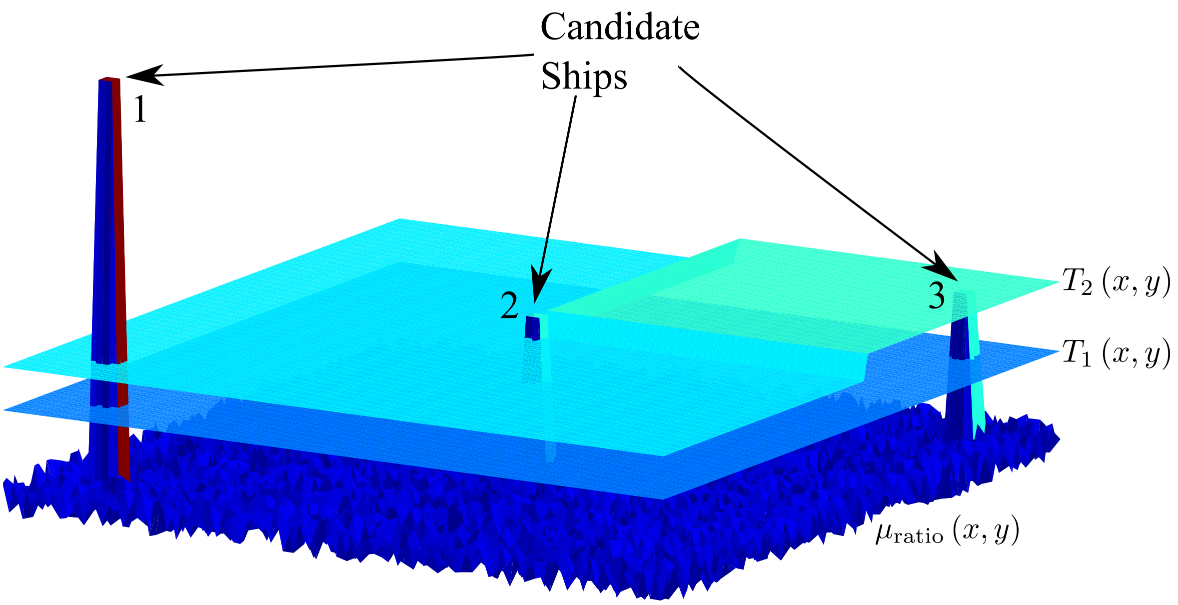

Figure 5.3. Ratio image $\mu_{\text{ratio}}(x,y)$ and two threshold manifolds, T_1 and T_2. Spikes one, two and three indicate three objects that are brighter than their surroundings, with the one and two being ships and three being a false alarm. Using a flat threshold manifold such as T_1 spikes two and three cannot be separated. A non-flat manifold, such as T_2, allows for discrimination between these two ships.

The single value scalar threshold T_C can be extended to a discrete threshold manifold or surface, constrained by the input image dimensions $X \times Y$ where $x = \{0,\ldots,X-1\}$, $y = \{0,\ldots,Y-1\}$ and $x,y \in \mathbb{W}$ such that threshold manifold $\mathbf{T}$ can be defined as

$$\mathbf{T} = \left\{ \left\{ T(x,y) \right\}_{x=0}^{x=X-1} \right\}_{y=0}^{y=Y-1} \tag{5.6}$$

$$= \begin{bmatrix} T(0,0) & \cdots & T(0,Y-1) \\ T(1,0) & \cdots & T(1,Y-1) \\ \vdots & \ddots & \vdots \\ T(X-1,0) & \cdots & T(X-1,Y-1) \end{bmatrix}. \tag{5.7}$$

This creates a discrete manifold that is bounded at the sides by the image limits X and Y and threshold value $T \in R^+$ [120, 121]. In much the same way the various threshold surface solutions possible for this method all lie within the constrained surface or discrete manifold parametrized by the two positional variables (x,y) within the image and the threshold value T (akin to the two pose variables and azimuthal lighting in [122]).

Using the new threshold manifold $T(x,y)$, the output binary image $J(\mathbf{I},x,y,T(x,y))$ is calculated with

$$J(\mathbf{I},x,y,T(x,y)) = \begin{cases} \text{true} & \text{if } \mu_{\text{ratio}}(x,y) > T(x,y), \\ \text{false} & \text{otherwise,} \end{cases} \tag{5.8}$$

where $T(x,y) \in R^{+}$. Pixels with an associated threshold value of $T < 1.0$ are ignored. The threshold value for this thesis was assumed to be within the range $T \in [1, \text{SAR}_{\text{max}}]$ where SAR_{max} represents the maximum pixel value in the SAR image. These bounds are important as they significantly reduce the range of possible threshold values which is important to reduce the computational complexity of the SA procedure. The lower bound of $T \geq 1$ is derived from the assumption that ships need to be at least as bright as their surroundings. If the threshold is larger than the maximum pixel value in the SAR image then no ships will be selected because no ship pixels can be greater than $T(x,y) \cdot \text{SAR}_{\text{max}}$ which sets the hard limit for the threshold.

In this method the assumption that a singular scalar threshold value is sufficient is discarded by creating a constrained threshold manifold whereby each pixel is assigned its own specific threshold. This threshold manifold or constrained surface [120, 121, 122], in addition to the local statistics within each window, provides a ship detection method which extends the CA-CFAR method to be more flexible whilst still avoiding the local PDF computation that other methods require [67, 74].

The task is then to compute appropriate thresholds for each pixel. For areas with higher average backscatter (those close to the nadir position) lower thresholds may be necessary whilst those further away from the nadir might require higher threshold values. A non-flat threshold can be constructed by setting a lower threshold for all values along the nadir at T_C^{min} and a higher one at the end of the swath with T_C^{max}.

5.3.4 Discrimination stage requirements

This study introduces two different discrimination stages. The prescreened binary image $\mathbf{J}$ generated by processing the input SAR image using equation (5.5) or (5.8) is fed into the two discrimination stages differently. For the first method, based on SA, the entire binary image is passed to the SA process as the initial manifold as described in section 5.4.3. For the second discrimination method SAR sub-images of 21×21 pixels are extracted where $J(x,y) = \text{true}$ and processed to extract the ship-like features. Using a low threshold CA-CFAR method to extract sub-images reduces the number

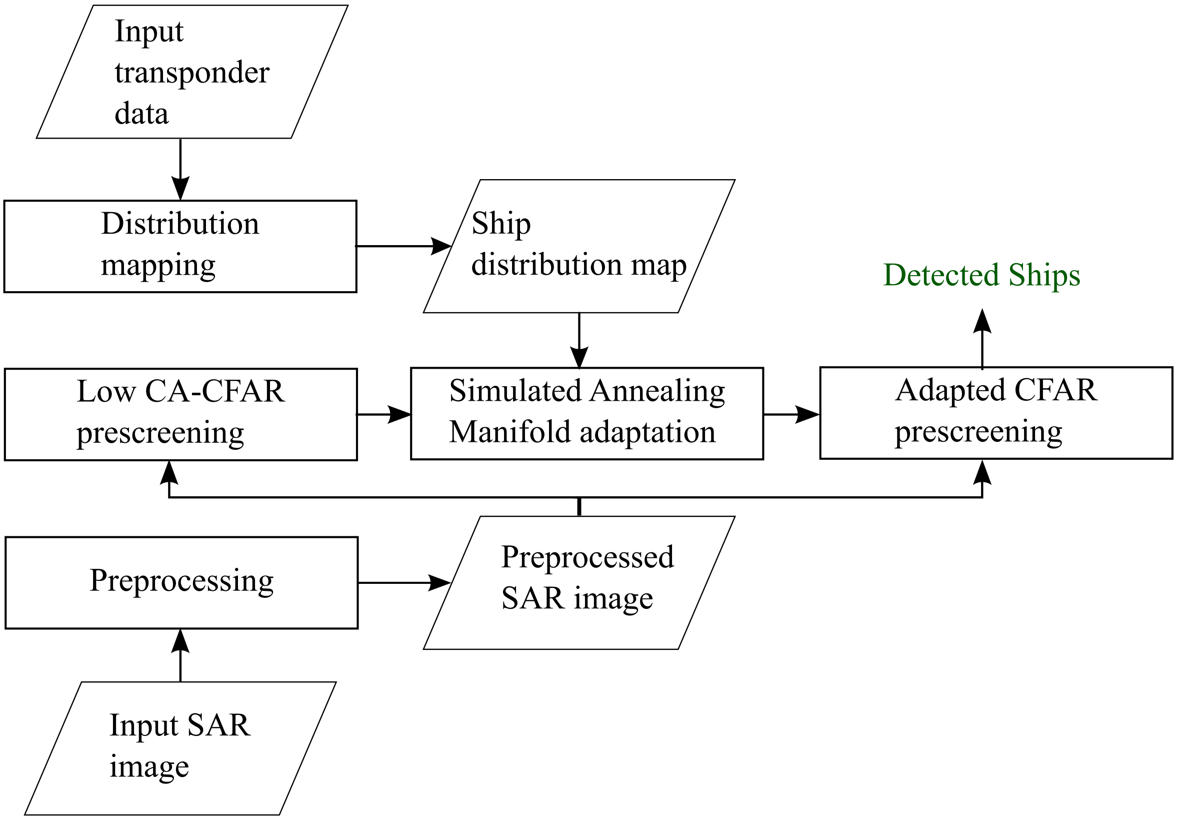

Figure 5.4. Flow diagram of the system process for this experiment. A SAR image is preprocessed by removing the land and georeferencing the image. This processed image is then prescreened using an initial CA-CFAR which generates initial detections. This initial solution is adjusted using SA until there is little change in the solution. This is then used in a second prescreening stage to produce a binary image with the detected ships centers as true values.

of sub-images presented to the classifier by at least an order of magnitude whilst still presenting all the possible ships in an image due to the low-threshold chosen [4].

5.4 DISCRIMINATION METHOD 1: SIMULATED ANNEALING MANIFOLD ADAPTATION

The entire detection process proposed for this first method is shown in Figure 5.4 [3]. The conventional CA-CFAR method described using equation (5.5) is extended in the next section to a new method that allows for per-pixel thresholding. Following this, the creation of the ship distribution map is described which is used as input into the SA stage which is discussed thereafter.

5.4.1 Ship distribution mapping

Traditionally, ship monitoring relies on using a transponder system [55, 17, 119, 6]. These transponder systems range from terrestrial based systems such as conventional AIS to space-based transceiver systems such as Satellite-AIS (Sat-AIS) and Long Range Identification and Tracking (LRIT) [17, 119, 6]. Ship detection using transponders becomes difficult when either the transponders are sabotaged or out of range (for terrestrial transponder systems). Despite this, the immense amount of data provided by transponders can still be useful for the creation of a ship distribution map to profile ship movement behavior [17].

If enough ship positions are collected over a number of years, a daily, weekly or even monthly ship distribution map for a given region could be generated, as shown in Figure 5.5. All 12 months of transponder data was used to generate the ship distribution map and it is assumed this would sufficiently model the average movement of ships within the image's geographical limits.

This ship distribution map is used to assign, to each pixel of the input image, a value which represents the likelihood of that pixel having shipping traffic. Pixels with high associated probabilities implies many ships transmitted their position at that geographical position and low associated probabilities means fewer ships had coordinates recorded for that geographical position. More formally, given an input image **I**, the associated ship distribution map **V** for that image is defined as

$$\mathbf{V} = \left\{ \left\{ V(x,y) \right\}_{x=0}^{x=X-1} \right\}_{y=0}^{y=Y-1} \tag{5.9}$$

$$= \begin{bmatrix} V(0,0) & \cdots & V(0,Y-1) \\ V(1,0) & \cdots & V(1,Y-1) \\ \vdots & \ddots & \vdots \\ V(X-1,0) & \cdots & V(X-1,Y-1) \end{bmatrix}. \tag{5.10}$$

Each $V(x,y)$ is calculated by adding up the number of ship positions found in the data nearest to that (x,y) coordinate divided by the total number of coordinates counted so that $V(x,y) = 1$. Once this distribution map is generated, it can be used to adapt an initial threshold manifold using SA. If the ship distribution map is unavailable, the current non-flat threshold manifold is passed onto the final stage and is used to threshold the input image to produce a final output. The ship distribution map is therefore useful to significantly reduce the false alarm rate but is not required in order for the method to produce results.

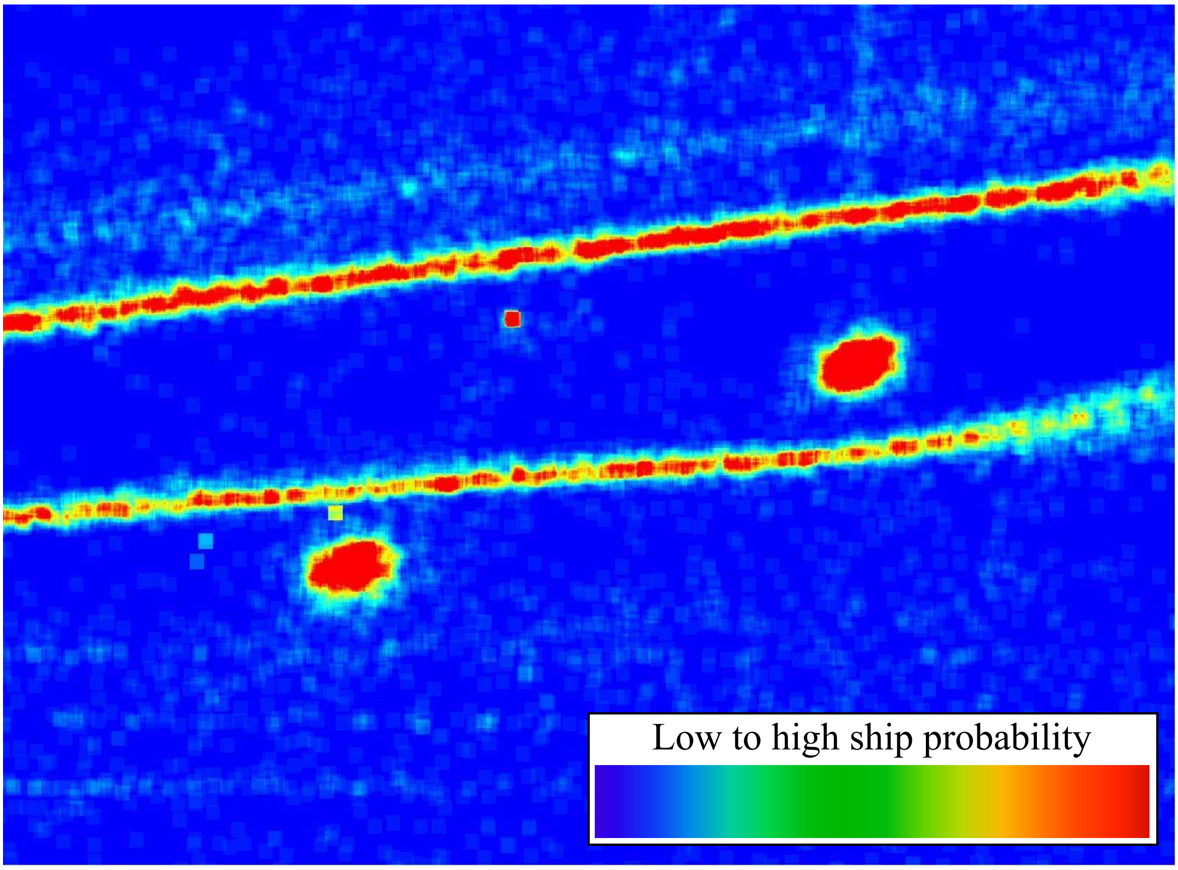

Figure 5.5. A section of the ship distribution map generated using all 12 months' LRIT data within the given geographic region. The image shows the ship distribution map off the coast of South Africa, near Mossel Bay (34.1833° S, 22.1333° E). It is interesting to note that two shipping lanes are clearly visible as well as two platforms. This is due to the fact that thousands of ship positions were collected along those lines, indicating a large number of traversals over those points.

5.4.2 Simulated Annealing

To adapt the threshold manifold a widely used optimization method known as SA was used in conjunction with the ship distribution map [123]. SA mimics the process of heating a material and allowing it to slowly cool to reduce abnormalities in the material. The method works by altering a currently accepted solution, testing the validity of the new solution and then replacing the current best solution with the new solution. The method also allows suboptimal solutions to be accepted to improve solution diversity. A flow chart of the SA method is shown in Figure 5.6. SA is used to adapt a flat manifold over a number of steps to increase thresholds over areas unlikely to contain ships. This reduces a large number of false alarms but also allows for low thresholds so ships that are not particularly bright

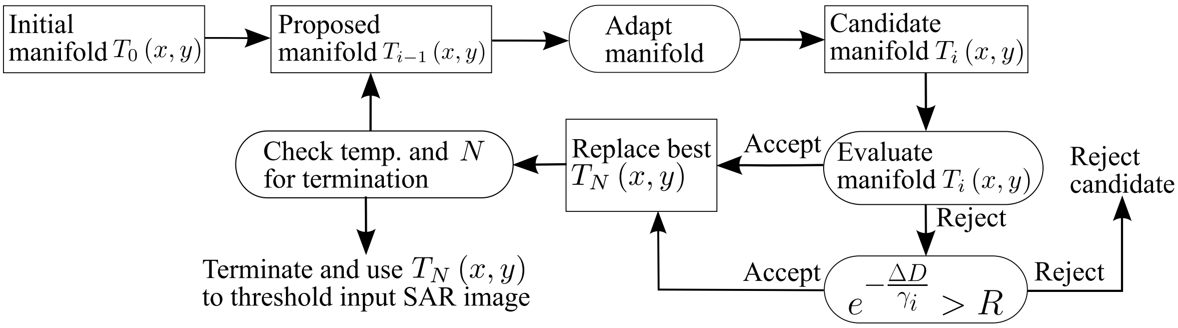

Figure 5.6. The SA threshold manifold adaptation process. The process starts at $i = 1$ by using the intial manifold T_0. The manifold is adapted using the process described in section 5.4.6 which generates the candidate threshold manifold. If the candidate threshold manifold fails evaluation it can still be selected as a new, best candidate by means of the Boltzmann probability as described in section 5.4.6. Finally, the process is terminated when either N steps have occurred or the change in temperature over a number of steps has stayed constant.

compared to their neighbors can still be detected. One of the benefits of SA is that it uses a given solution to generate further solutions. This is in contrast to other optimization methods, such as GA, which search the entire solution space using multiple different candidates [124, 125].

5.4.3 Initial threshold manifold

It is assumed that the initial (flat) threshold manifold highlights all ships within the SAR imagery with a large number of false alarms. This implies that the initial threshold manifold T_0 is a good starting solution because subsequent processing steps need only remove the false alarms by increasing those pixels' thresholds to improve performance. This selection of the starting manifold significantly reduces the number of searchable ship positions from the entire image to only areas where pixels are as bright as their surroundings. Subsequent steps of the SA processes uses the ship distribution map to evaluate changes in threshold manifold values. The initial threshold manifold, T_0, is generated by running a low, flat CA-CFAR prescreening on the input SAR image $\mathbf{I}$ such that $T_0(x,y) = J(\mathbf{I}, x, y, T(x,y) = 1.0)$. For the sake of brevity T_i for $i = 1, 2, \ldots, N$ is equivalent to $T_i(x,y)$ where N represents the total number of SA steps. This will select all areas of the input image that have a brighter-than-average pixel value including all ships. These positions will have an associated threshold manifold value of $T_0 = 1.0$ whilst all others will have have $T_0 = 0.0$. To correctly increase threshold manifold values for false alarms a means of threshold manifold evaluation is presented next.

5.4.4 Mean change in probability per ship

SA requires a manner to evaluate the current solution T_{current} and its possible replacement T_i. To do so, some performance metric must be calculated for each solution. Given T_i and $\mathbf{I}$, the number of ships detected L_i, the total probability v_i^{total} at time step i can be calculated. The total probability v_i^{total} is the sum of all probabilities for all the detected ship centers across the whole image using $V(x,y)$ at each time step i which is computed as

$$v_i^{\text{total}} = \sum_a^X \sum_b^Y \{V(a,b) \mid J_i(\mathbf{I},a,b,T_i) = \text{true}\}, \tag{5.11}$$

where $J_i(\mathbf{I},a,b,T_i)$ is the input image $I(x,y)$ processed using the CA-CFAR with the threshold manifold T_i. Note that total probability may change at each step because the detected ships may change at each stage.

The mean probability per ship is

$$\alpha_i = \frac{v_i^{\text{total}}}{L_i}. \tag{5.12}$$

This can be extended to include the variations in the mean probability per ship at each time step by noting the change in α and the change in the number of ships such that the mean change in probability per ship, β_i, is

$$\beta_i = \frac{|v_i^{\text{total}} - v_{i-1}^{\text{total}}|}{|L_i - L_{i-1}| + \varepsilon}. \tag{5.13}$$

The symbol ε is a arbitrarily small value, typically $\varepsilon << 10^{-9}$. At each time step, β_i can change based on the current threshold manifold T_i, which then directly affects the value of total probability v_i^{total}.

Once the mean change in probability β_i is calculated for a given time step, a cost function can be used to decide if the current threshold manifold T_i represents an improvement or not. The cost function at time step i, D_i, is calculated using β_i with

$$D_i = 1 - |\beta_i - \beta_{i-1}|. \tag{5.14}$$

For the initial threshold T_0 values are assumed such that $D_0 = 1$, $v_0^{\text{total}} = 0$, $L_0 = 0$ and $\beta_0 = 0$. Cost function values that are closer to one are preferable because they represent a smaller change in mean ship probability. This is because a small decrease in mean ship probability indicates a reduction in the number of ships in low probability zones which are most likely false alarms. This causes a small change in β between step $i-1$ and i and thus the cost function tends closer to one in those cases. An

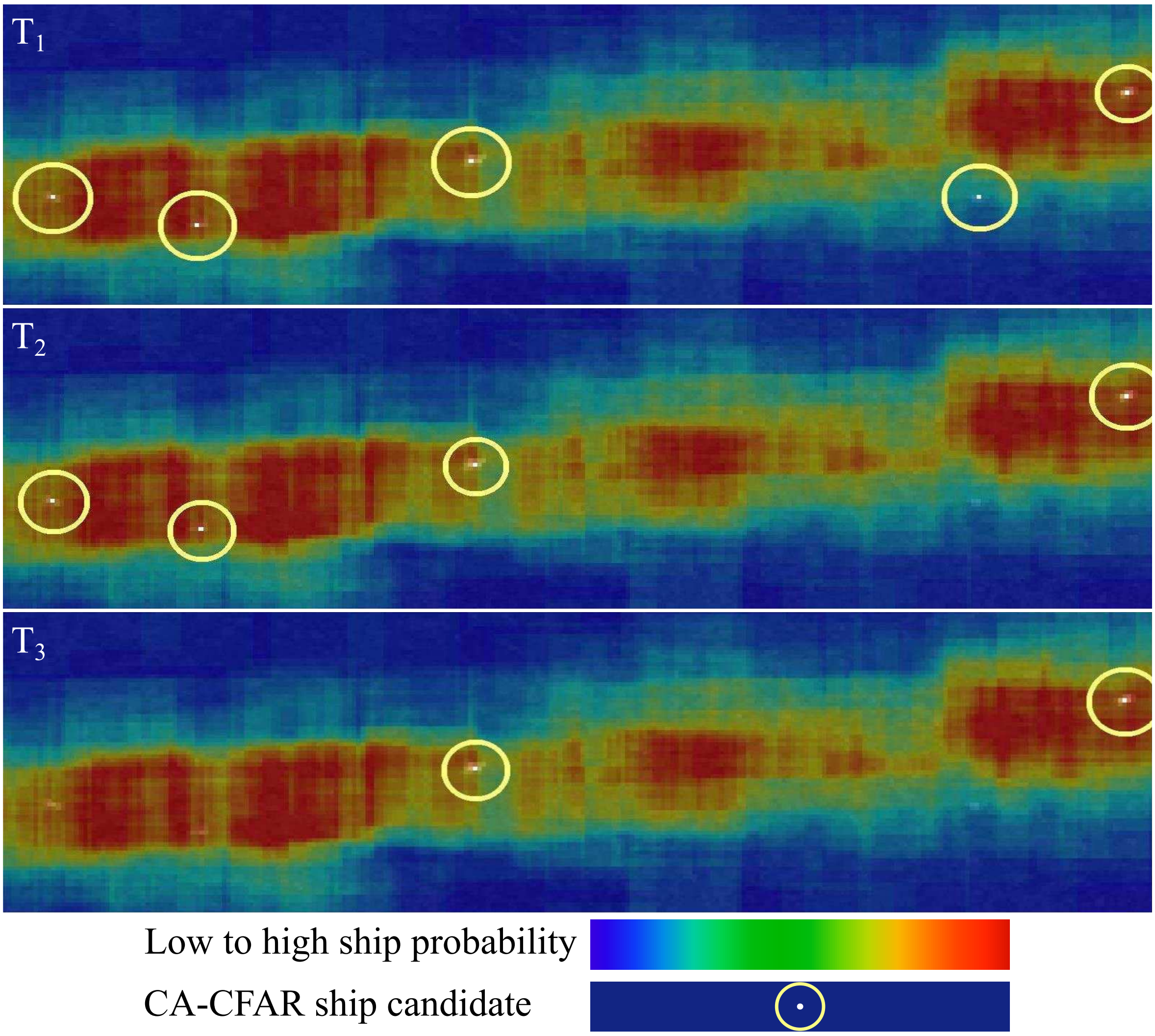

Figure 5.7. Three flat threshold manifolds are shown with $T_i(x,y) = \{2.0, 2.5, 3.0\}$. The ship distribution map $V(x,y)$ is superimposed over each image. The number of ships are $L_1 = 5, L_2 = 4$ and $L_3 = 2$ and the total probability is $v_1^{\text{total}} = 0.5, v_2^{\text{total}} = 0.45$ and $v_3^{\text{total}} = 0.2$ per step. Using equation (5.14) the cost values are $D_1 = 0,900, D_2 = 0,950$ and $D_3 = 0,925$. Notice how, intuitively, the highest cost threshold T_2 is the best threshold manifold because it removes a redundant bright pixel present at T_1 but does not remove the two high probability ships like T_3 does.

example of this process is shown in Figure 5.7. Do note that for the sake of clarity, a flat threshold manifold is used in this example and not the non-flat manifold as introduced in this thesis (the same principle applies).

5.4.5 Simulated Annealing alternatives

Despite the efficiency of methods such as GA or Particle Swarm Optimization, the SA produces a solution which is more intuitive to the problem of computing the threshold manifold [124, 125, 126]. The reason is that the CA-CFAR produces accurate initial conditions for the SA to adapt quickly to an acceptable solution, which can reduce the computational costs.

There are a number of reasons SA was selected above other methods. As mentioned in [125, 124], it is expected that there will be cases where either GA or SA will be better suited to the problem. The following presents the reasoning as to why SA was considered better suited to the generation of non-flat threshold manifolds given an initial input solution.

When comparing GA and SA on a computational basis, in most cases GA is far better than SA as it searches the solution space simultaneously using multiple solutions at once versus SA which searches the solution space using one solution with many epochs of adaptation [124]. In most cases this causes SA to have a much greater computational time because if the optimal solution is at one point of the searchable space and a search is started in the opposite position then the entire searchable solution space is searched serially when using SA rather than in parallel for a GA [124]. The main advantage of SA can be seen with the intelligent selection of the initial starting point and the way in which the initial starting point is adapted to form a final solution [126]. The initial threshold manifold, T_0, is generated using a low threshold CA-CFAR highlighting all of the ships as well as a number of false alarms. The best possible manifold will be a version of T_0 that rejects all false alarms but maintains all of these correct detections. Due to the selection of this initial starting point a large area of the search space becomes irrelevant because the solution is inherent from T_0. Therefore, a major benefit of GA being efficient solution space searching becomes less applicable as the entire solution space need not be searched. Furthermore, the way in which GA searches might cause it to stochastically diverge away from T_0, thus searching for a solution in part of the solution space that is not applicable.

A practical concern regarding selecting GA above SA in this work is generating a starting population from T_0. The starting GA population could be generated from this initial solution but then the question of population solution diversity arises. How can a starting set of solutions be generated from a good initial solution whilst maintaining population diversity? A second, related concern is how can the genes and mutations for each generation be designed for a threshold manifold to a) maintain solution diversity so that local minima are avoided and b) keep the population close enough to the good initial solution, even during mutations? To this end, SA lends itself as the more natural optimization method in this instance as better manifolds are derivatives of the original and changes are improvements upon previous steps. Also the small, gradual change in threshold value across the manifold using the SA procedure fits well with the manner in which each solution is evaluated (detection of large changes in average ship probability). This furthers the case for SA being a more suitable optimization method for this work given the way in which the auxiliary data is used. Looking specifically at how the computational burden can be reduced, we provide a few specifics as to why using SA becomes more attractive than in the general case by reducing the searchable solution space. Due to the initial input manifold being acceptable, the size of the SA solution search space is greatly reduced from $X \cdot Y \cdot \mathbb{R}$ searchable points (every single manifold coordinate) to $L_0 \cdot \mathbb{R}$ searchable points (where L_0 is the number of initial ships detected at T_0). For a typical Sentinel-1 image, $X \cdot Y \geq 475000000$ whereas $L_0 < 5000$ which is a 95000 fold decrease in search space size. Furthermore, the adaptation process computational time per epoch is linear in the number of initial and subsequent ship detections and as more false alarms are removed the adaptation process runtime per epoch decreases.

Another point that needs to be considered is that the possible searchable space per searchable point need not be the entire $\mathbb{R}$ range. Let us assume an 8-bit grayscale input image for interests, the solution space is reduced to $1 \leq T(x,y) \leq \mathrm{SAR}_{\max}$. The lower threshold bound, $1 \leq T(x,y)$, stems from the requirement that ships be at least as bright as their surroundings. The upper bound of threshold values can be understood with two special cases, namely when $\mu_c = 1$ and as $\mu_c \to 0$. When $\mu_c = 1$, $\mu_{\text{ratio}} = \frac{\mu_{\text{ROI}}}{\mu_c} = \mu_{\text{ROI}}$ and so T cannot be more than the maximum pixel value, in this case $T(x,y) \leq \mathrm{SAR}_{\max}$. When $\mu_c \to 0$,

$$\lim_{\mu_c \to 0} \mu_{\text{ratio}} \to \infty >> T(x,y), \tag{5.15}$$

We can then choose the maximum value of $T(x,y)$ to be any finite value less than ∞ because the above equation will be satisfied. Therefore, $T(x,y) \leq \mathrm{SAR}_{\max}$ is selected to fall in line with the previous case. This reduces the search space that the SA has to deal with to $\mathbb{R} \in [1, \mathrm{SAR}_{\max}]$ rather than all $\mathbb{R}$ for each manifold threshold value.

The selection of which method to implement to perform the adaptation is a matter of designer choice [125, 124]. In some applications better computational time performance will be required and so GA or another method might be chosen and the adaptation process changed to suit that method. For the case of this thesis, a proof of concept was presented and the selection of optimization method hinged on which method seemed to lend itself best to the presented process and given auxiliary data rather than practical and implementation concerns. For the case of this thesis the adaptation of a single solution given a well derived input solution indicated SA would be a suitable method to test the concept.

5.4.6 Manifold adaptation

The manifold adaptation scheme used in this thesis estimates the degree to which the areas of the manifold should be adapted by using the number of ships that are neighboring every ship. The threshold manifold is increased by a uniform random amount inversely proportional to the number of ships near each ship and added to the previous threshold value at that pixel which is expressed as

$$T_i(a,b) = T_{i-1}(a,b) + \left(\frac{R_z}{Z(a,b)}\right) \text{ where} J_i(\mathbf{I},a,b,T_i) = \text{true}, \tag{5.16}$$

where R_z is a randomly chosen uniform value which scales the change at position (a,b) from the previous position. $Z(a,b)$ refers to the number of ships in a square area around the ship found in $J_i(\mathbf{I},a,b,T_i)$. If no ships are found within the area, $Z(a,b) = 1$. The reasoning behind the inverse relation between the number of ships and the threshold change is that areas with more ships should be increased slowly as the likelihood of ships in those areas is assumed to be more. Singular, solitary pixels' thresholds should be increased rapidly so that their effect on the overall mean probability can be ascertained quickly. If these solitary pixels are in low probability areas then their removal will have little to no effect on the mean probability per ship and these would typically be assumed as false alarms and require higher threshold values.

Despite the above, a threshold with a low cost can still be accepted if the rejected candidate's probability of acceptance is above a given value known as the Boltzmann probability. The SA method allows for this replacement of the current optimal solution in order to prevent the process from settling into non-optimal, local minima. To prevent this, the temperature parameter γ is introduced which is related to the mean threshold value. Specifically, the current temperature γ_i is equal to

$$\gamma_i = \frac{100}{\mu_{T_i}}, \tag{5.17}$$

$$\mu_{T_i} = \frac{1}{L_i}\sum_{x=0}^{X-1}\sum_{y=0}^{Y-1} T_i(x,y) \text{ where } T_i(x,y) > 0, \tag{5.18}$$

for $i = 1 \ldots N$. We assume $\gamma_0 = 100$ and $\mu_{T_0} = 1.0$ because at $i = 0$ all threshold values within T_0 are either $T = 1.0$ for highlighted pixels or $T = 0.0$ for the rest.

The value of μ_{T_i} increases as the SA process continues, thus decreasing the temperature γ_i over time. Using the current temperature and the change in cost, a previously rejected threshold manifold can be accepted using the Boltzmann probability if

$$e^{-\frac{\Delta D}{\gamma_i}} > R. \tag{5.19}$$

Where ΔD is the change in cost between the current solution and the best solution, γ_i is the current temperature of the solution and R is a random uniform real number in the range $[0,1]$.

The above is repeated until the change in cost function over a number of time steps is negligible or a number of predefined time steps N has been reached. The final output image is $J_N = J(\mathbf{I}, T_N(x,y))$. The ships within this image are grouped together, and their center positions within the image are used to compare against the known ship positions to determine the method's performance. Using the center position ensures groups of nearby detections are fused in order to prevent azimuthal ambiguities near to the ships whilst maintaining the correct number of detections.

5.5 DISCRIMINATION METHOD 2: HAAR-LIKE FEATURE EXTRACTION AND CASCADE CLASSIFICATION

Research into Sentinel-1 ship detection generally focuses on the higher resolution IW imagery [82, 73, 127]. IW imagery facilitates precise monitoring of small areas and the higher resolution imagery allows algorithms that cannot necessarily be created using medium resolution imagery such as ship-type classification. However, the impracticality of monitoring large areas using only high resolution SAR imagery demands effective capability be developed to detect ships in low-to-medium resolution SAR imagery. Also initial detections can be made using medium resolution, wide swath imagery which can then advise operators where to task high resolution SAR imagery. Almost exclusively in ship detection studies the prescreening step is configured to stringently remove as many false alarms as possible [127, 80] which reduces the responsibility of the ship discrimination step. The difficulty with this is that stringent removal of false alarms in the early detection steps increases the likelihood of not detecting ships in subsequent stages. Depending on the requirements of the ship detection process and operator, this may not be a desirable result.

The previous discrimination method explored the limits of what can be done by extending the conventional CFAR algorithm to exhibit per-pixel threshold values. One of the downsides of using this

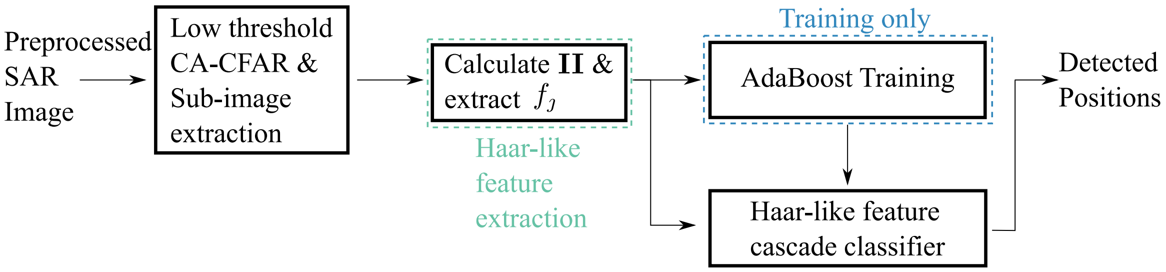

Figure 5.8. The Haar-like feature extraction and cascade classification overview. The figure shows the two types of systems - training creates the cascade classifier that is used during the ship detection process when testing.

method is the computational burden required to generate a manifold that provides reasonable results, typically due to optimization procedures such as SA. Also, depending on the prescreening and discrimination method used, a significant increase in computational complexity can sometimes occur in large SAR imagery [80]. Ship detection using machine learning has historically been arduous due to the limited number of samples available to train systems which, in part, is due to prohibitively expensive SAR imagery. With the release of the free Sentinel-1 imagery, large SAR datasets could be created and thus research into more modern machine learning techniques became possible. This thesis introduces a novel ship detection method which combines a low-threshold presecreening step with a novel ship discrimination step that extracts ship-like features and presents these to a classifier tailored to effectively identify ships from false alarms. These unique features are scalable, rapidly calculable and are descriptive enough to highlight ships effectively across a large SAR dataset. By using CA-CFAR as the prescreening step these features are only extracted for objects likely to be ships thereby improving the method's efficiency on SAR imagery compared to the direct application on the SAR imagery. The combination of these adaptable features and versatile machine intelligence-based ship discrimination allows the proposed method to be both efficient and accurate [4].

An overview of the proposed method is described in Figure 5.8. After the low-threshold CA-CFAR prescreening method identifies likely ship candidates which are sent to the novel discrimination method as 21×21 subimages. These subimages are processed to extract Haar-like features which are then fed to an adaptable cascade classifier to discriminate ships from non-ships.

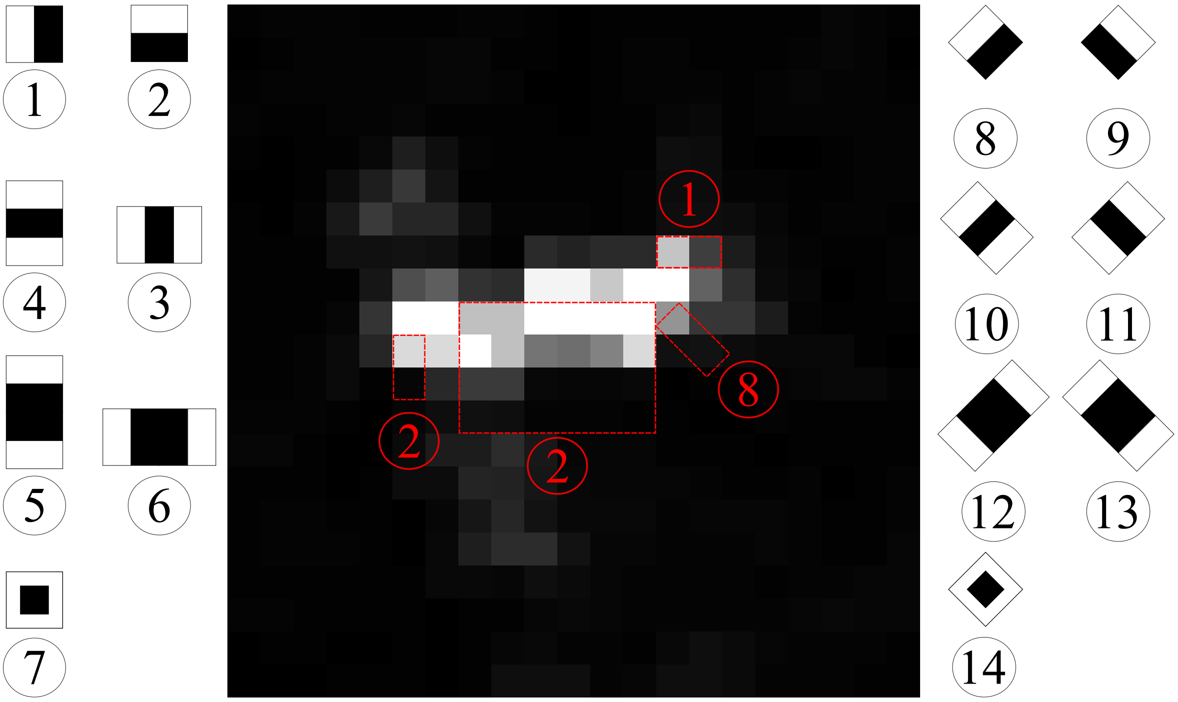

Figure 5.9. A 21×21 RADARSAT-2 SAR intensity sub-image containing a ship with the upright [128] and rotated [129] Haar-like feature templates. Each ship can be described by a combination of these feature templates, at various scales and positions in the image.

5.5.1 Haar-like feature extraction

The process of detecting all ships in an image can be accomplished if it is assumed that ships are brighter than their surroundings and a low enough threshold ($T_C = 1.0$) CFAR will detect all ships in an image [3, 18]. To remove the many accompanying false alarms we propose to use special ship-like features called Haar-like features. These features have a number of directly relevant advantages for SAR ship discrimination as they are scalable, rapidly calculable and also reduce the in-class variance whilst increasing the out-of-class variance [128, 129]. Furthermore, using variants that are rotated, the features are simultaneously scale and rotation invariant [128, 129]. An example of how the features look, scale and rotate to describe ships effectively is shown in Figure 5.9.

Haar-like features come in three types (edge, line and center) and two variations (upright [128] and rotated [129]). A single Haar-like feature is simply the normalized difference between two (or more) scalable areas in a SAR ship sub-image. To aid in rapid calculation of these features, the concept of integral images is introduced [128]. An integral image $\mathbf{II}$ is the integral result of $\mathbf{I}$ and is calculated as the summation of all pixels above and to the left of a pixel at $I(x,y)$, inclusive. More specifically,

$$II(x,y) = \sum_{x' \leq x} \sum_{y' \leq y} I(x', y'). \tag{5.20}$$

The advantage of using an integral image to calculate sums is that a single pass over the image is all that is required to calculate any integral image value and subsequent values only require reference lookups to **II**. Assuming $II(-1,y) = II(x,-1) = 0$ [129], the integral image value at pixel (x,y) is calculated using only four references to **II** such that

$$II(x,y) = II(x,y-1) + II(x-1,y) + I(x,y) - II(x-1,y-1). \tag{5.21}$$

To calculate a single two-part Haar-like feature, f_j we make use of the integral image to calculate the value over the two template areas using only six integral image references. Assuming two template rectangles r_1 and r_2 with heights $\mathcal{Y}_1$ and $\mathcal{Y}_2$ and widths $\mathcal{X}_1$ and $\mathcal{X}_2$, a two-part upright Haar-like feature f_j is calculated as

$$f_j = \frac{\Omega(r_1) - \Omega(r_2)}{\mathcal{X}_1 \times \mathcal{Y}_1 + \mathcal{X}_2 \times \mathcal{Y}_2}, \tag{5.22}$$

$$\begin{aligned} \Omega(r) = {} & II(x-1,y-1) + II(x+\mathcal{X}-1, y+\mathcal{Y}-1) - \\ & II(x-1, y+\mathcal{Y}-1) - II(x+\mathcal{X}-1, y-1). \end{aligned} \tag{5.23}$$

Where f_j is normalized by the area of the two templates so that features of different scales are weighted equally and $\Omega(r)$ is the pixel sums for r_1 and r_2, respectively. Due to two common points, f_j only requires six references to **II**, irrespective of where or how large the feature is within the sub-image. The above only applies to upright features, but can be extended to include rotated features using a rotated integral image [129] thereby improving rotation invariance. For an illustrative example of how to calculate a single upright two part Haar-like feature see Figure 5.10. Once these features are extracted they are presented to a trained classifier created using AdaBoost.

5.5.2 Cascade classifier creation using AdaBoost

A single 21×21 sub-image can contain up to 111160 (upright) or 155060 (upright+rotated) Haar-like features. This would be too many features for conventional classifiers to successfully train on due to the curse of dimensionality [130]. To effectively select the most descriptive Haar-like features and create a classifier to discriminate ships the Adaptive Boosting (AdaBoost) method is chosen [128, 129, 131]. AdaBoost does this using three main concepts: weak learners or feature thresholds; strong learners which are weighted combinations of weak learners; and sample importance to identify which samples are most difficult to classify. By intelligently ordering the strong learners in a cascade classifier,

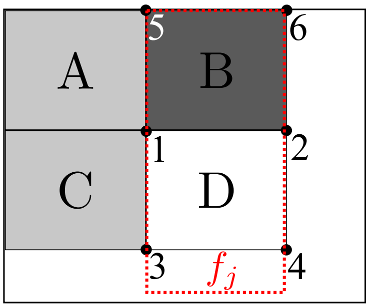

$$1 = \sum\sum A \qquad 2 = \sum\sum(A+B)$$

$$3 = \sum\sum(A+C) \quad 4 = \sum\sum(A+B+C+D)$$

$$\begin{aligned} \Omega(B) &= 2-1 \\ \Omega(D) &= 4+1-(2+3) \\ f_j &= \Omega(D)-\Omega(B) \\ &= 4+1-2-3-2+1 \end{aligned}$$

Figure 5.10. Example calculation of an arbitrarily sized upright Haar-like feature within a SAR ship sub-image. Points 1 through 4 are calculated as the sum of pixels above and to the left of the point. These points are then used to calculate sums B and D (equation (5.23)) using only two and four references, respectively. Finally, irrespective of size, feature f_j can be calculated using equation (5.22) with only six unique integral image references (normalization not shown).

AdaBoost also ensures that only the most likely ship candidates reach the final stages where the stages are most complex and easy-to-discriminate samples are quickly accepted/discarded in the first stages thereby improving classification computational efficiency [128]. An overview of the entire AdaBoost training procedure is given in Figure 5.11 as well as an example of the cascade classifier using strong and weak learners in Figure 5.12.

The AdaBoost creation of the cascade classifier proceeds over $\mathcal{L}$ rounds where $l = 1,2,\ldots,\mathcal{L}$. For each round S_l steps occur so that $s = 1,2,\ldots,S_l$. Assuming M samples (both ship and ocean) such that $m = 1,2,\ldots,M$ with N features such that $n = 1,2,\ldots,N$ where each sample $x_1,x_2,\ldots,x_M$ is $x_m = \{f_1,f_2,\ldots,f_N\}$ and f_n is the nth Haar-like feature. For each sample we assume a label $y_m \in \{-1,1\}$ for ocean and ship examples, respectively. Additionally, each sample x_m has a sample importance distribution value $\mathcal{D}_s(m) = \{\mathcal{D}(1),\mathcal{D}(2),\ldots,\mathcal{D}(M)\}$. For the first step $s = 1$ all samples are weighted equally such that $\mathcal{D}_1(m) = \frac{1}{M}$.

For each round l a strong learner $H_l(x)$ is created that is a linear combination of weighted weak learners h_s. The simplest weak learner function that can be defined is a threshold θ_n of a single feature f_n such that $h_n(x_m) = f_n > \theta_n$. This threshold is selected as the value that separates the M samples with a fixed error less than 0.5 for each feature n. At every time step a single learner is selected such that h_n at s (h_s for brevity) from the set of all weak learners $\mathcal{H}$ if it has the lowest error rate (at least $\varepsilon_n < 0.5$). The error ε_n represents the error that feature has in classifying all the samples. The Single learner is

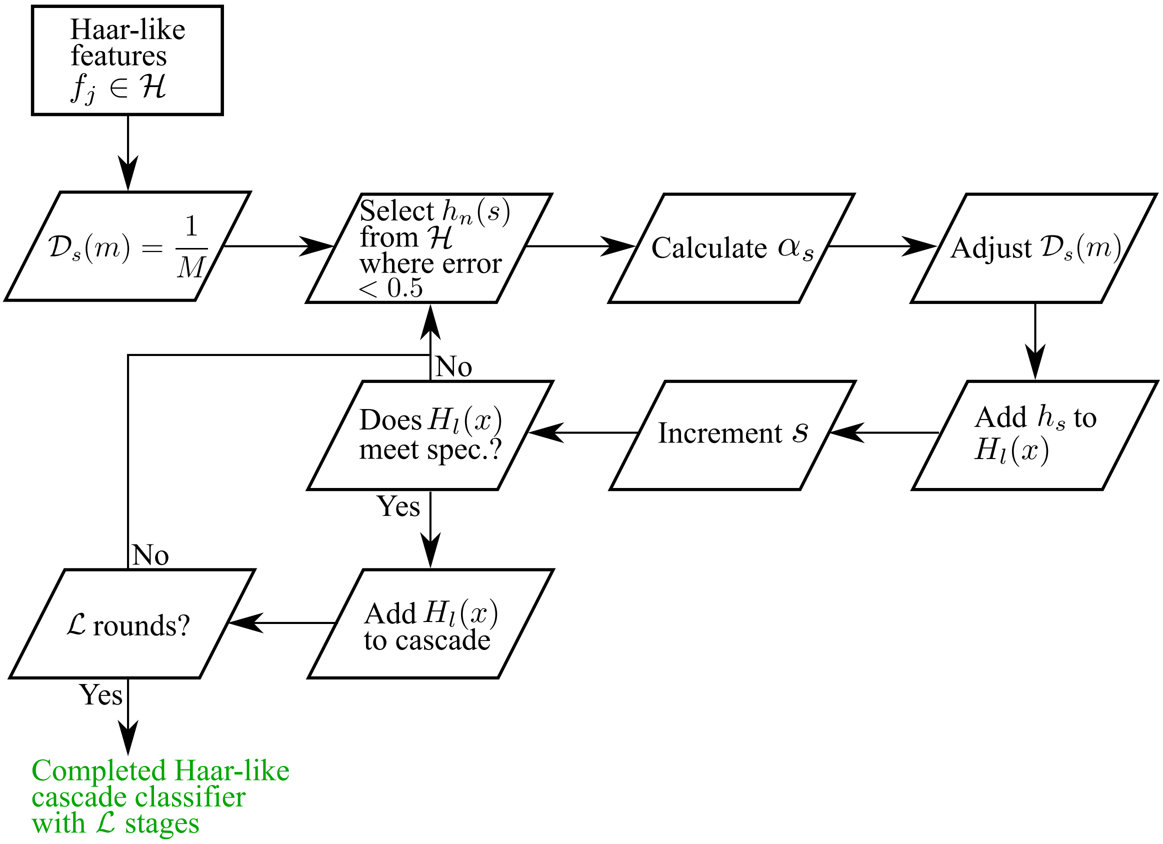

Figure 5.11. An overview of the AdaBoost training algorithm. The system receives sub-images containing likely ships and extracted Haar-like features. During each of $\mathcal{L}$ rounds a single strong learner is created from $S_{\mathcal{L}}$ weak learners. During each round if the cascade classifier meets the desired specifications (can be specified in general or per-round) then it is added to the cascade classifier otherwise more weak learners are added until the specification is met.

assigned a weight α_s using

$$h_s = \arg\min_{h_n \in \mathcal{H}} \sum_{m=1}^{M} \mathcal{D}_s(m)[h_n(x_m) \neq y_m], \tag{5.24}$$

$$\alpha_s = \frac{1}{2} \log\left(\frac{1+r_s}{1-r_s}\right), \tag{5.25}$$

$$r_s = \sum_{m=1}^{M} \mathcal{D}_s(m) h_s(x_m) y_m. \tag{5.26}$$

Where $\mathcal{H}$ contains $N = 111160$ or $N = 155060$ weak learners depending if upright or upright and rotated Haar-like features are selected. The weighting factor, α_s, is known as the weak learner importance. As shown in equation (5.25), weak learners h_s with error rates closer to 0.5 will have lower α_s values and hence their contribution to the strong learner $H_l(x)$ will be decreased because they provide less discrimination capability. By combining enough of these weak learners it is has been proven that the resulting strong learner (and by extension cascade of strong learners) can be trained to a required accuracy and false alarm rate on the training data with a bounded generalization error [128, 129, 131].

The final computation during step s is the adjustment of the distribution $D_s(m)$ for the next step $s+1$. The distribution value at m is increased for misclassified samples and decreased otherwise. The magnitude of this change is dependant on the previous distribution value of $D_s(m)$ and current weak learner importance α_s such that

$$\mathcal{D}_{s+1}(m) = \frac{\mathcal{D}_s(m)\exp(-\alpha_s y_m h_s(x_m))}{Z_s}, \tag{5.27}$$

where Z_s is a normalization factor chosen so that $\mathcal{D}_{s+1}$ is a distribution. Adjusting the sample importance in this manner allows the AdaBoost procedure to hone in on features that can be thresholded such that $\varepsilon_n < 0.5$, even for difficult to classify samples when $s > 1$. This is repeated S_l times until the strong learner meets a specified minimum accuracy and false alarm rate.

Once S_l steps have taken place using equation (5.24), (5.25) and (5.27), a strong learner $H_l(x)$ can be defined as a linear combination of S_l weak learners $h_s(x)$ and weak learner importances α_s such that

$$H_l(x) = \text{sign}\left(\sum_{s=1}^{S_l} \alpha_s h_s(x)\right). \tag{5.28}$$

After $\mathcal{L}$ rounds a cascade classifier is created containing $\mathcal{L}$ strong learners $H_l(x)$ which in turn are composed of S_l weak learners. The AdaBoost procedure reorders the cascade classifier so that, typically, $S = 1$ for $l = 1$ and $S \geq 1$ for $l \geq 1$. This configuration is an integral part of the proposed method because it allows for the removal of easy-to-identify false alarms at the beginning of the cascade while delegating difficult sample discrimination requiring more features to the end, thereby improving computational efficiency. If a sub-image is classified as a ship by $\mathcal{L}$ cascaded strong learners it is deemed a ship.

5.5.3 Additional considerations

In addition to the above there are a number of practical considerations that need to be addressed.

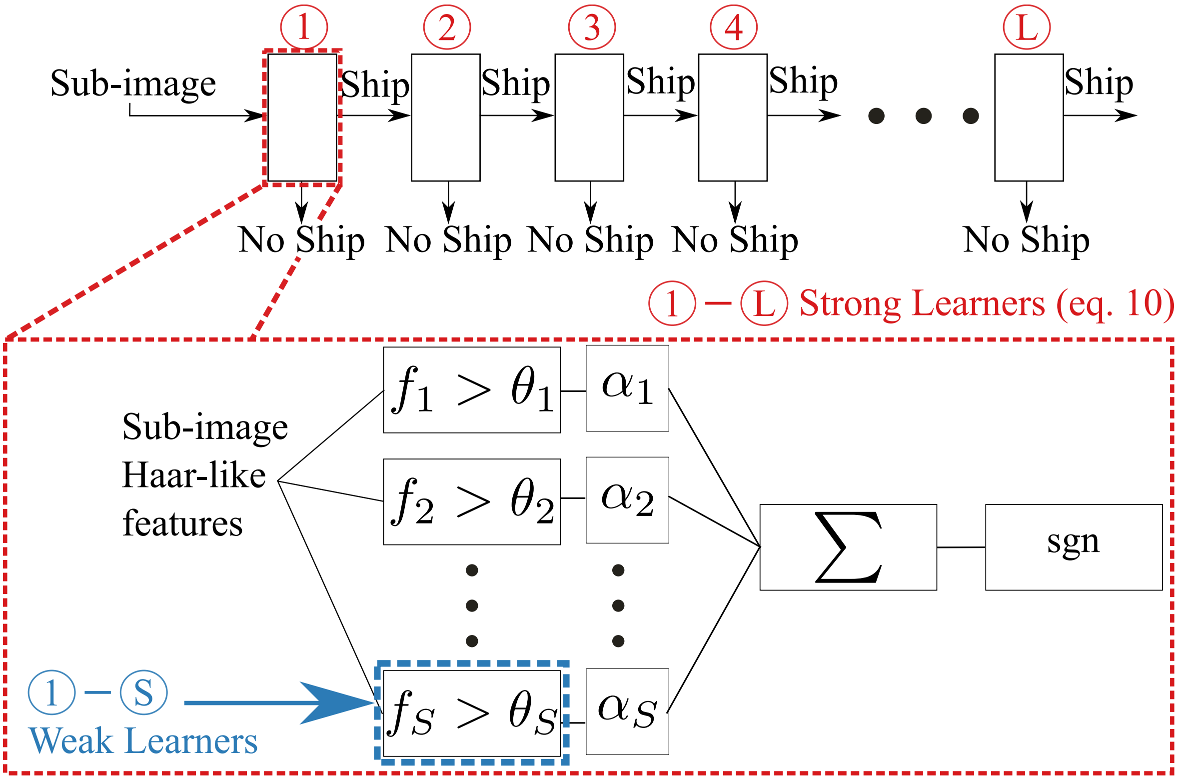

Figure 5.12. A trained AdaBoost Haar-like feature cascade ship discriminator. A sub-image is fed into the cascade window and only the relevant Haar-like features are extracted per-stage. If a sub-image survives $\mathcal{L}$ strong classifier stages then it is classified as a ship. Each strong classifier has S weak classifiers within it where typically $S = 1$ for the first stage and $S > 1$ to improve computational efficiency.

5.5.3.1 Feature selection

In classical machine learning, one of the most important tasks is the selection of relevant features for classification. This step, referred to as feature selection or engineering, often requires in-depth knowledge of the problem area as well as an understanding of how certain features may affect results. Feature engineering often involves statistical analyses of the features including trying to capture which features explain the most variance in the dataset. As mentioned above, the Haar-like feature extraction process extracts hundreds of thousands of features for even a small 21×21 sub-image. While a technique such as Principle Component Analysis (PCA) can be extended using Singular Value Decomposition (SVD) to process this many features, in practise this leads to very large matrices that can be limited by hardware (i.e. the **U** matrix of the SVD enhanced PCA method will be 155060×155060

single/double precision matrix for our rotated feature's case). Selecting features by hand is feasible when the number of features is below 1000 but beyond that becomes an error-prone task with no guarantee that the selected features properly allow for exploration of the solution space.

A number of modern machine learning techniques place the responsibility of feature selection within the training architecture and is part of the reason the AdaBoost method was chosen as the training method for this system. The AdaBoost method described above selects the most relevant features using α_x, focuses on the most relevant examples using $D_s(m)$ (those which are proving the hardest to classify) and builds the classifier at the same time. This is one step removed from many of the latest machine learning techniques which even create problem-specific features as part of the network known as deep learning. In this case the completeness and similarity of Haar-like features to ships lent itself to the natural selection of these features over hand-crafted features. Furthermore, the AdaBoost training helps eschew a common difficult of feature selection by automatically selecting relevant features as part of the training process.

5.5.3.2 Application of the method specific to wide-swath SAR

The direct application of the original Haar-like methods [128, 129] has shown a detection accuracy performance that is unacceptable on its own, despite the low FAR achieved [4]. To explain this the concept of voting needs to be introduced. Practical implementation of the the Haar-like papers use a sliding window approach to detect objects within an image. Each object is assigned a detection vote $\mathcal{V}$ after its successful classification using the Haar-like cascade classifier and then the window is moved one pixel on and the same process is repeated again until the entire image has been covered. An object is only detected within the image when there is a minimum of $\mathcal{V}$ detections for that object within the image. This vote value $\mathcal{V}$ sets a hard limit to the minimum number of detections that are necessary to accept a sample when $\mathcal{V} > 1$. If $\mathcal{V}$ is set too high (either by design or automatically during training) then correct objects can be missed in a large varying datasets whereas setting this value too low will increase the FAR. This is akin to CFAR prescreening where the probability of false alarm or threshold determines how many ships will be detected/missed.

Our implementation of the method avoids this problem by always assuming $\mathcal{V} = 1$ or in other words no voting is applied. By providing the Haar-like detection stage with more likely targets, as opposed to every single pixel, we assume that after both CA-CFAR prescreening and L classifier stages the current window has a ship in it and voting does not need to be done. To this end low-threshold prescreening removes the need for voting because we only pass over each object only once in an entire image and therefore do not need to collect votes.

Finally, the original methods were tested on images that are typically less than 1000×1000 [132]. At this size the sliding window approach presents approximately 960400 overlapping 21×21 windows to the classifier. The average size of a SAR Sentinel-1 GRDH image is approximately 22900×19600 [4] which would present approximately 447990400 overlapping 21×21 windows to the classifier. While the original methods performed well on the original images sizes they were given, but both original papers' methods were simply not designed to process images two orders of magnitude larger and evidence of this is shown in their poor performance by direct application to the dataset [4]. Instead of direct application some adaptation to these two original methods was applied to allow the method to perform better on SAR imagery. Even if a prescreening stage still allows 10000 samples through to the classifier per image we still reduce the number of 21×21 windows seen by the classifier by a factor of approximately 44800. This represents a significant reduction in processing required to identify ships in SAR imagery especially compared to the SA manifold adaptation method whilst further increasing the probability of detection because the number of possible false alarms presented to the classifier is reduced than simple direct application of the Haar-like original methods to SAR imagery.

5.5.3.3 Adaptability of proposed method

Adaptability for our described method is achieved using three aspects. First using a fixed low threshold will ensure all potential ships in the SAR image are presented to the cascade classifier, irrespective of image type/sensor/resolution as long as we assume ships are brighter than their surroundings. Secondly, by assuming each detection has a fixed number of votes $\mathcal{V} = 1$ ensures we need not alter this minimum based on ship size/frequency in any of the SAR images due to practical processes such as sliding window techniques, instead relying on the AdaBoost training to deal with hard-to-classify samples. Finally, by making use of a machine learning method adaptability is increased because new sources of SAR imagery could be dealt with by retraining the classifier.

5.5.3.4 Fast Contrast Stretching

The original implementations of the Haar-like classifier [128, 129] used a fast contrast stretching algorithm to ensure samples are uniform when presented to the classifier. The method presented here makes no use of contrast stretching due to the peculiarities present in SAR imagery. In the originals, the types of images presented to the system [132] constitute gray-scale imagery that remains relatively consistent between images and their dynamic ranges all fall within the same range, more-or-less. SAR imagery is completely different in that ships near the nadir will often have different backscatter values compared to those far away, often with a very large dynamic range. Original testing indicated that using contrast stretching to normalize these differences negatively affected performance. This is likely due to the property that while visually appearing similar, the values ships have compared to false alarms such as azimuthal/range ambiguities differs enough to be detected by the classifier. It was concluded that these backscatter values inherent to ships are being used as additional information by the classifier to improve detection accuracy and therefore any sort of contrast stretching was removed.

5.6 CONCLUSION

In this chapter two methods for ship detection in SAR imagery were introduced. The first method, SA CFAR Threshold Selection, extends the conventional CA-CFAR method to allow for per-pixel thresholding. To select the correct thresholds across a SAR image the proposed method uses an auxiliary data set of historic ship positions. This *a-priori* data, in combination with the optimization procedure of SA, allows the method to choose thresholds which could allow for more effective detection of ships at sea in SAR imagery. The chapter also introduced a machine learning-centric ship detection method known as Haar-like feature cascade classification. This method uses an adaptive set of ship-like features which are robust to changes in rotation, and translation and scale to describe SAR ships. These features were fed into a binary tree cascade classifier which tries to identify ships from non-ships. The AdaBoost training method selects the best features from the overcomplete Haar-like feature set and also creates and intelligently orders the cascade to improve detection efficiency.

CHAPTER 6 DATASET DESCRIPTION

6.1 CHAPTER OVERVIEW

A robust dataset needs to be created to properly evaluate any new method. By ensuring the dataset is of a high quality, the results and analysis derived can be better understood and better interpretations of the strengths and weaknesses of a method can be extracted. During the creation of the dataset, the extents of the data need to be thoroughly documented and tested in order to determine the parameters that work well to circumvent these limitations. This, in turn, can help to derive a deeper understanding of the results various methods obtain given the dataset. The dataset was designed according to the following objectives:

- The dataset needs to be large enough to encompass the most probable scenarios the methods might be expected to operate in.

- The dataset needs to be well documented in terms of all aspects from the data package level to the ground truth positions of ships.

- Errors and sources of error within the dataset need to be well documented in order to identify where and how certain methods fail.

- The dataset needs to be constructed in such a way to accommodate comparative research in various fields, including machine-learning.

This chapter presents a large SAR dataset, covering two separate SAR satellites using three separate resolutions. The dataset comprises of two components - transponder data derived from LRIT and AIS messages and SAR imagery. The first section of this chapter details how the collection of SAR imagery was preprocessed including details on radiometric calibration, georeferencing, warping, landmasking and associated sources of expected errors. The second section details how the ships were extracted and referenced. It also provides a summary of the details related to ships, their positions and how the data is organized for ease of comparison to future methods. The final section of the chapter details the transponder data associated with some of the ship detection and the two ways in which it was used.

6.2 SYNTHETIC APERTURE RADAR DATA

6.2.1 Study area

The geographic extent of the SAR imagery used in this dataset is shown in Figure 6.1. The SAR imagery covers approximately 1.17 million km^2 which includes, approximately, 76% of the South African EEZ and 90% of its territorial waters. The dataset was acquired between 6 October 2014 and 22 July 2015. The dataset contains 1596 ships all across the South African EEZ and nearby waters; the geographical distribution of these ships can be seen in Figure 6.2.

The dataset consists of 46 SAR images covering approximately 76% of South Africa's EEZ across: two sensors (RADARSAT-2 and Sentinel-1A); three resolutions (SCNA $81\,\mathrm{m} \times 30\,\mathrm{m}$, EW GRD High (GRDH) $50\,\mathrm{m} \times 50\,\mathrm{m}$ and EW GRD Medium (GRDM) $93\,\mathrm{m} \times 97\,\mathrm{m}$); and four polarizations (HH, HV, VV, VH). There are 1596 ships (positive samples) across all 46 images, extracted as 21×21 pixel sub-images for this experiment (accommodating a maximum possible ship size of 20 pixels long). The dataset contains over 500 000 possible false alarms but from these a random selection of 3192 21×21 sub-images with no ships within them were used as negative samples. The difference in sample size models what a ship discrimination step would see with a prescreening method such as the one discussed in section 5.3.3.

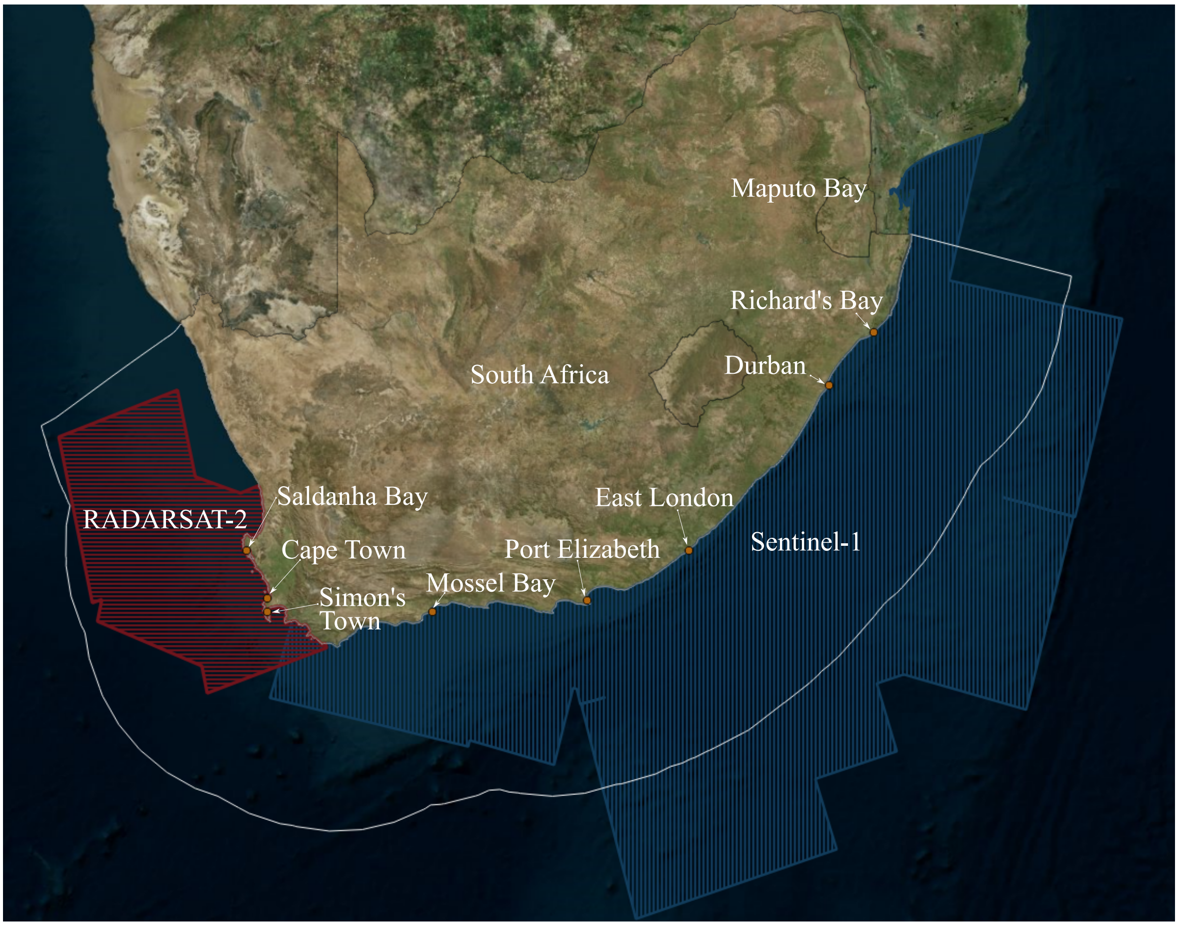

Figure 6.1. A map of South Africa and the extent that the Sentinel-1 and RADARSAT-2 images cover. The white border indicates the South African EEZ. Approximately 80% of the EEZ is covered by the SAR dataset. In addition to this a number of images cover the Maputo Bay area of Southern Mozambique and form part of the dataset.

6.2.2 Sentinel-1

The first freely available imagery from the Sentinel-1 constellation was released on the 6 October 2014, which included two images located over South Africa and were used in an initial research study [7, 6]. All 46 images used in this dataset are from the EW swath acquisition mode with Incidence Angles between 19.0° and 47.0° and a swath width of 400 km. At the time of writing, no SLC imagery over South Africa in EW mode was available, specifically over the EEZ waters of South Africa. All of the data were GRD imagery using either the High (GRDH) or Medium (GRDM) resolution class. GRDH images have a resolution of 50 m × 50 m and pixel spacing of 25 m × 25 m (in range and azimuth respectively). Similarly, GRDM imagery has a resolution of 93 m × 97 m with a 40 m × 40 m pixel spacing. The dataset covers the three of the possible four EW polarization acquisition modes, namely: SDH (HH+HV), SDV (VV+VH) and SSV (VV). There are a total of 22 Sentinel-1 acquisitions, 21 containing two polarization images (either SDH or SDV) and one with a single VV polarizations, for a total of 43 Sentinel-1 images. A summary of the imagery within the dataset is given in Table 6.1.

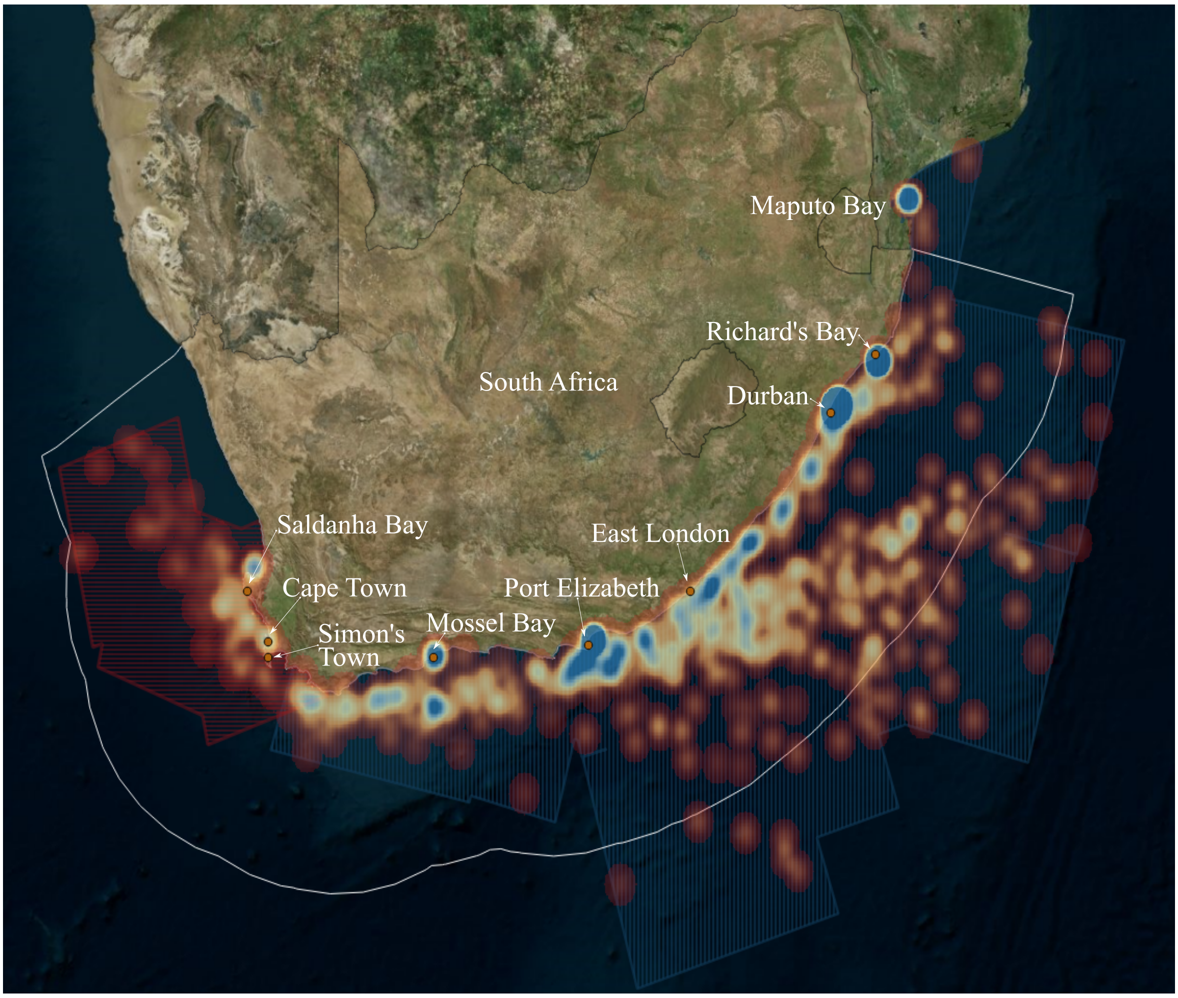

Figure 6.2. A distribution map of all the 1596 ships in the dataset. The Durban, Richard's Bay and Port Elizabeth ports show significantly higher ship density than most of the South African coast. A number of factors cause this including the fact that most of the Sentinel-1 images occur over these areas and because these ports are closer to the South African economic hub, Gauteng.

6.2.3 RADARSAT-2

Three RADARSAT-2 images were acquired near Cape Town, South Africa. All three are ScanSAR Narrow A (SCNA) imagery of the non-SLC type (intensity only). The imagery has a resolution of

Table 6.1. SAR data information per image sensor and polarization where rg means range and az means azimuth.

	Sentinel-1		RADARSAT-2
Attributes	GRDH	GRDM	SCNA
Acquisitions	6	16	3
Images Total	12	31	3
Type	EW	EW	SGF
Incidence Angle (°)	$19.0-47.0$	$19.0-47.0$	$20.0-39.0$
Swath Width (km)	400	400	300
Resolution [rg x az] (m)	50×50	93×97	81×30
Pixel Spacing [rg x az] (m)	25×25	40×40	25×25
Number of Looks [rg x az]	3×1	6×2	2×2

$81\,\mathrm{m}\times30\,\mathrm{m}$ and pixel spacing of $25\,\mathrm{m}\times25\,\mathrm{m}$. The images have a swath width of 300 km and have an incidence angle range of between 20.0° and 39.0°. All three SAR images were acquired in the HH polarization. These images all came in the SAR georeferenced fine (SGF) format which was an intensity only, GRD product. A summary of the RADARSAT-2 imagery is given in Table 6.1.

6.3 SAR DATA PREPROCESSING

The preprocessing steps described here are applied after the conversion from SLC to GRD imagery done by the satellite data providers before the product was distributed to the authors. As satellite providers do not provide access to the SLC data for some types of imagery it can cause processing artifacts which consumers have no control over. The images were used as is from the supplier with only the preprocessing steps described here. The reasoning for this is three-fold. The first is that the imagery is already received with some preprocessing steps applied, such as multilooking, which already degrades the size of the ships inside the image (speckle is reduced at the expense of resolution). Additional measures such as speckle filtering have not been applied to preserve the ships resolution. Secondly, additional preprocessing has been kept to a minimum to ensure that the dataset is consistent for distribution. A user of the dataset should be able to acquire the imagery from the satellite providers and with little effort reproduce the dataset. This helps to create a universal dataset that can be used by multiple users with the knowledge that the preprocessing applied has not affected the creation of the dataset. Finally, the methods developed need to be robust to changes in the input SAR imagery. By using the data as-is the methods should learn to deal with errors that crop up on a variety of different

SAR imagery. Wherever possible, clear errors have been marked in the dataset as false alarms so that the methods' abilities to remove these errors are noted.

6.3.1 Data acquisition and output

Both Sentinel-1 and RADARSAT-2 acquisitions data are received as compressed zip files. The decompressed zip files are fed into a collection of tools (namely either Geospatial Data Abstraction Library (GDAL) or GAMMA based tool-chains) to generate interoperable Geographical Tagged Image File Format (GeoTIFF) files and associated Extended Markup Language (XML) meta-data files. Each acquisition and polarization within (for Sentinel-1 images with multiple popularizations per acquisition) are processed independent from one another. The final output of the preprocessing steps is a geocoded GeoTIFF per polarization for a consistent data access strategy.

6.3.2 Radiometric calibration

The first step of the dataset preprocessing is the conversion from digital numbers into normalized Radar Cross Section (RCS) values using Radiometric Calibration [133, 61]. To perform geographical parameter extraction radiometric calibration needed for comparisons between objects across acquisitions. The Sentinel-1 products provides an updated Look Up Table (LUT) for its Level-1 products defined as

$$A_{\sigma} = \sqrt{\frac{A_{\mathrm{DN}}^{2} K}{\sin(\rho)}} \tag{6.1}$$

where A_{DN} is an unsigned 16 bit LUT which defines the scaling from internal SLC to GRD product, K is the single calibration constant for all final products and ρ is the local incidence angle [61]. Finally, the average backscatter coefficient $\sigma^{0}(i)$ [134] at digital number $\mathrm{DN}(i)$ is

$$\sigma^{0}(i) = \frac{E\{\mathrm{DN}(i)\}^{2}}{A_{\sigma}^{2}} \tag{6.2}$$

where $E\{\mathrm{DN}(i)\}$ is the mean pixel amplitude digital number values over a small area (typically 3×3), taken directly from the measurement (GeoTIFF) file. A similar procedure is followed for RADARSAT-2 radiometric calibration. For a complete overview of radiometric calibration in SAR see [133].

6.3.3 Georeferencing and warping

The next preprocessing step involves georeferencing the input SAR image. This assigns real-word coordinates to each pixel of the image using Ground Control Points (GCPs). These GCPs are inherent within the GeoTIFFs in both Sentinel-1 and RADARSAT-2. More precise estimations of these pixel longitudes and latitudes can be acquired using each satellite's orbital state vector meta-data [57] but for the purpose of this study the ones provided with the GeoTIFF files were deemed sufficient given that the dataset is comprised of medium resolution imagery and the corrections should not make a significant impact to detection locations within reasonable error tolerances (less than the MMU of 2 pixels).

To provide a uniform access format all of the images are then warped to be north-facing (geocoded) images. For the case of this study all images were warped to the World Geodetic System 1984 or "WGS84" projection. This was selected due to being the same datum used for Global Positioning System (GPS) coordinates which align with transponder-based acquisitions used in the dataset later on.

One important aspect to note is that georeferencing images might require interpolation when the image is resampled. The simplest method, nearest neighbor, was used as the resampling method to reduce the amount of alterations done to pixels values but other resampling methods such as bilinear, cubic, cubic spline and Lanczos resampling are available [71]. These methods resample the pixel value using varying types of weighted neighborhoods which might affect the final pixel value and were avoided to keep the data as consitient as possible.

6.3.4 Land masking

The final step of preprocessing is to remove any land within the image. The complexity of the land removal step is based on the needs of the dataset and can range from simple landmasking using a shapefile to advanced coastline extraction procedures [135, 62, 136, 57]. To reduce the effects of small georeferencing errors and ships too close to the shore a buffer of 1 km was used to extend a conventional coastline shapefile. This aligns with the fact that any ships close enough to the coast can be detected using terrestrial transponder-/radar-based systems and the necessity for highly accurate SAR detections that near to the cost is reduced.

6.3.5 Sources of error

As mentioned previously, some image providers do typically not give access to the RAW data or SLC data for wide-swath imagery over South Africa and instead make derived products accessible to researchers and organizers. The following is a non-exhaustive list of possible errors due to the out-of-scope conversion from RAW to SLC to GRD imagery handled by the satellite providers:

- To get to square pixels within GRD imagery, the SLC imagery needs to be sampled at different rates in the range and azimuthal directions. The conversion to these square pixels for GRD products can cause actual ships sizes to be larger or smaller than their actual footprint in the original SLC imagery.

- Azimuthal and range processing can cause artifacts discussed in section 3.11 such as smeering, land-object ghosts and SAR ship ghosts. These can distort sea-clutter and ships alike which may present a problem for methods not tuned to remove these errors automatically.

- There is a trade off between the reduction of sidelobes and main-target resolution. Sidelobe reduction often occurs via apodization which in turn reduces the main sidelobe resolution [54] and is fixed for GRD products such as GRDM, GRDH and SCN imagery.

For the data creation step of the dataset the above errors have been manually eliminated to the best of the author's abilities. During testing using the results of each method is also scrutinized to identify which methods fail to remove these types of errors automatically. Initial results indicate that most errors occur due to misaligned land masking, followed by errors due to GRD conversions and finally the most difficult errors to remove are the ones related to ships such as ship size and copies of the ship appearing as ghosts but these are also the fewest.

6.4 SAR SHIP REFERENCING

6.4.1 Ship definition

In SAR intensity imagery covering the ocean, a ship is defined as any object that is sufficiently brighter than its surrounding ocean backscatter [3, 18, 64]. For the sake of simplicity, and due to the resolution of the SAR imagery for this dataset, it was assumed that a ship is an area of ocean that has higher backscatter than its neighbors and also each ship was least 2 pixels in length (its MMU). Ships that are smaller than these dimensions are beyond the scope of this dataset and would be better analyzed using higher resolution SAR imagery. This definition, therefore, ignores single pixels with high backscatter due to speckle noise. The intent of this dataset is to cover most areas of the EEZ and thus wider swath widths are necessary which in turn reduces the available resolution of the dataset. To this end, any objects that do not meet these criteria are deemed non-ships or ocean clutter and are defined as false positive areas of interest.

Each ship within the dataset has four associated images, namely a ship patch, reference patch, ship sub-image and reference sub-image as shown in Figure 6.3. Patches are images which cover a large area of pixels (101×101) centered on the ship. Sub-images are smaller images (21×21) with little to no other information but the ships found at the center of the image. The large size of the patches ensure ships of all possible sizes are captured within the image and the sub-image's smaller size is based on statistical evaluations of all ships present in the dataset. Patch images provide local context to evaluate where the ship is (near a harbor, far out at sea, within a crowd of other ships). This context is important to help identify why detection errors may occur relative to various features around the ship, especially errors from SAR preprocessing such as smeering, sidelobes and ghosts. Finally, by providing these larger images around the ship the need to scan the large SAR images is reduced when reprocessing/re-evaluation is required. Sub-images are smaller images around the ship designed to emulate machine learning datasets such a the MNIST [137] or CIFAR-10 and CIFAR-100 datasets [138].

6.4.2 Reference images

For the purpose of this study, a reference image is a binary image which indicates "true" for pixels most likely associated with the ship at the center and "false" for all other pixels. Reference images

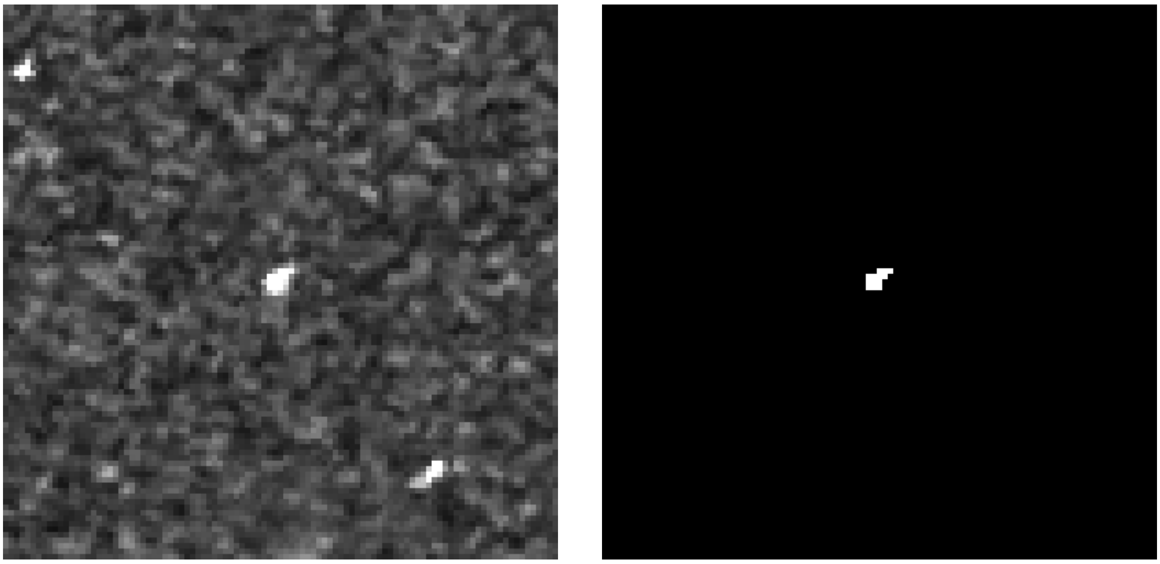

Ship patch Reference patch

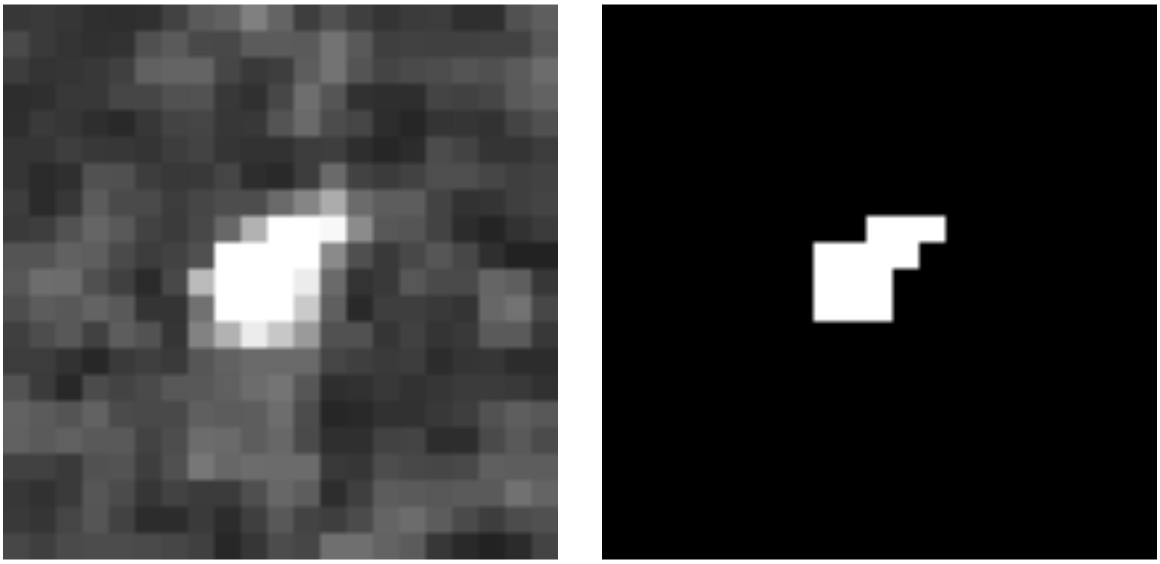

Ship sub-image Reference sub-image

Figure 6.3. The four main types of sub-images in the dataset. Notice how the ship patch area provides local context as it shows two other ships within the image. The ship sub-image only contains the ship at the center. The reference patch and image only highlight the center ship's pixels as one and the rest of the pixels are set to zero.

sizes were set to match the same size as the SAR ship patches and sub-images (101×101 and 21×21 respectively).

To effectively identify ships within the SAR imagery and then to reference them correctly the following procedure was taken:

1. Each of the 46 SAR images were scanned and targets of high backscatter are identified using both the basic GeoTIFF and a contrast stretched version (which enhances darker areas and darkens brighter, near-nadir areas of the SAR image). Each potential bright area's latitude and longitude was recorded. This process was repeated twice for each image to ensure no potential bright target areas were missed.

2. For each potential target, a patch of the SAR image centered on the target was extracted. For each target the patch was re-examined using the context provided by the patch and marked as either a ship or not. Known geographical features such as islands, sea-platforms, rough sea areas were used to eliminate targets with high backscatter that were in fact false alarms.

3. Another identification step occurred by matching ships across polarizations. Ships that appeared within one pixel (25m or 40m depending on sensor resolution) for a single acquisition were deemed the same ship across different polarizations. Ships that did not match across polarizations were still kept if they matched the criteria as discussed above.

4. For each identified ship patch an associated reference patch was created by setting every pixel likely to be a ship pixel to one and the rest to zero. It should be noted that any other potential ships or objects not at the center were ignored within each reference patch.

5. Each reference patch was analyzed to determine the ship's centroid, length and width. For each centroid a 21×21 sized sub-image was extracted from the ship and reference patches to create the ship and reference sub-images.

6. A final stage of ship identification matched the identified centers of the SAR ships against a dataset of known AIS positions. The exact details of the AIS referencing is discussed in section 6.5.2.

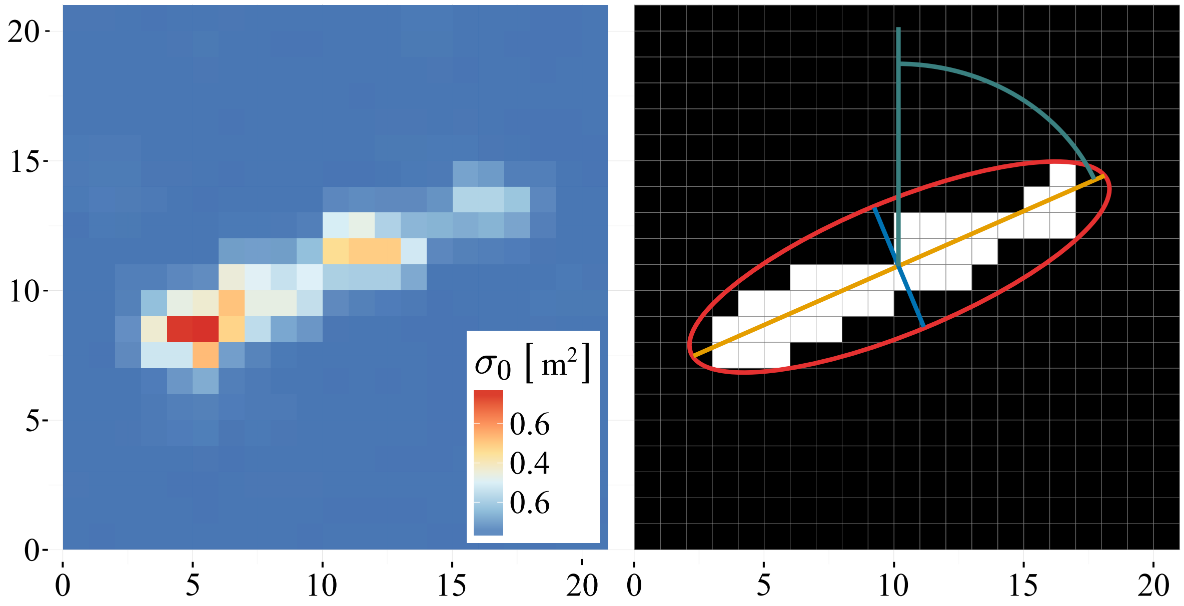

Figure 6.4. A radiometrically correct SAR ship sub-image and its associated reference sub-image (ship number 160 of 1596). The image also shows the four main attributes of the reference image, namely the ship's centroid $\mathbf{C}$, major axis length $\mathbb{L}_{\text{maj}}$, the minor axis length $\mathbb{L}_{\text{min}}$ and ship orientation or heading ω extracted using the Minimum-Volume Enclosing Ellipsoid.

6.4.3 Ship attributes

For each reference patch, a list of attributes are extracted. These attributes provide valuable information to help guide the design of detection methods. For the purpose of this study, four attributes are calculated namely the ship's centroid $\mathbf{C}$, major axis length $\mathbb{L}_{\text{maj}}$, the minor axis length $\mathbb{L}_{\text{min}}$ and ship orientation or heading ω. Within the dataset itself, it is possible to extract more attributes but for the sake of brevity this study only discusses these four.

The ship's centroid is the location of the center of mass of the reference image. Given a finite set $\mathbb{S}$ of k reference points with a "true" value such that $\mathbb{S} = \{\mathbf{P_{1,2}}, \dots, \mathbf{P_k}\}$ in $\mathbb{R}^2$ where $\mathbf{P_1} = (x_1, y_1)$ is the first point's x and y coordinates, the centroid $\mathbf{C} = (x_{\text{centroid}}, y_{\text{centroid}})$ of the reference image can be calculated as [139]

$$\mathbf{C} = \frac{\mathbf{P_1} + \mathbf{P_2} + \cdots + \mathbf{P_k}}{k}. \tag{6.3}$$

To calculate the other three ship attributes the Minimum-Volume Enclosing Ellipsoid (MVEE) can be used [140]. For the sake of completeness it should be stated that the method is defined for higher dimensionalities but for the case of the 2-D reference images the method actually calculates a minimum-area enclosing ellipsoid. As defined in [140], a full-dimensional ellipsoid $\mathcal{E}_{Q,\mathbf{C}}$ in $\mathbb{R}^2$ is specified by a 2×2 symmetric positive-definite matrix Q with center $\mathbf{C}$ is defined as

$$\mathcal{E}_{Q,\mathbf{C}} = \left\{ \mathbf{P} \in \mathbb{R}^2 : (\mathbf{P} - \mathbf{C})^T Q (\mathbf{P} - \mathbf{C}) \leq 1 \right\}. \tag{6.4}$$

The area of this ellipsoid is therefore calculated as $\text{Area}\left(\mathcal{E}_{Q,\mathbf{C}}\right) = \eta\, \det Q^{-1/2}$ where η is the area of the unit ball in $\mathbb{R}^2$ and det is the determinant applied to Q [140]. The MVEE of a set of points $\mathcal{S}$ is defined as $\text{MVEE}\left(\mathcal{S}\right)$ and will satisfy the following

$$(1/2)\text{MVEE}\left(\mathcal{S}\right) \subseteq \text{conv}\left(\mathcal{S}\right) \subseteq \text{MVEE}\left(\mathcal{S}\right). \tag{6.5}$$

The notation $\text{conv}\left(\mathcal{S}\right)$ is the convex hull of $\mathcal{S}$ and the left-hand side ellipsoid is scaled by $1/2$ around its center. Assuming $\mathcal{S}$ is the set of vertices for the full-dimensional polytope $\mathcal{P} \subseteq \mathbb{R}^2$ (the reference ship shape), then $\text{MVEE}\left(\mathcal{S}\right)$ yields a rounded approximation of $\mathcal{P}$. For exact details on the calculation of the MVEE, see [140].

The major axis length $\mathbb{L}_{\text{maj}}$ is the approximate length of the ship and can be calculated by finding the furthest two points that lie on the MVEE. A ship's approximate width, $\mathbb{L}_{\text{min}}$, is calculated as the line perpendicular to the major axis. The ship's heading ω is calculated as the angle between the major axis length and north at 0°. The attributes for a single reference sub-image are shown on the right in Fig. 6.4.

6.4.4 Dataset organization

The purpose of creating such a dataset as described above is to facilitate repeatable, verifiable experiments within a fixed and known extent of data. To this end this dataset has been split into two organizational structures, namely the SAR images themselves with associated ship positions used for the process of ship prescreening and a collection of sub-images and patches with associated metadata for ship discrimination and analysis. Splitting the dataset up may help to identify methods that perform well in one task but may not necessarily perform well for the other task. Splitting the ship detection process into separate entities for prescreening and discrimination therefore allows for greater focus on each task [3, 4]. The following sections describe the two data organizational structures which help facilitate the creation and evaluation of methods for each task.

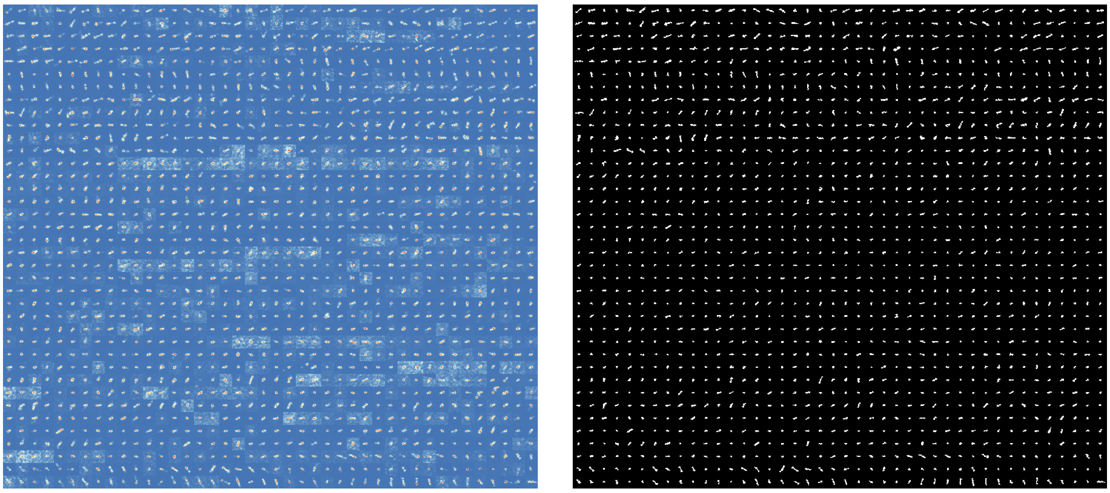

(a) SAR unity scaled ship **(b)** SAR reference ships

Figure 6.5. All 1596 ship (a) and reference (b) sub-images within the dataset. These cover the two satellites at three resolutions. Each ship sub-image has been normalized so that the brightest point is at unity for display purposes. Each reference sub-image is analyzed using the MVEE to calculate attributes such as SAR ship length, width and orientation.

6.4.4.1 Prescreening dataset

Almost all ship detection literature uses a known collection of ship positions to determine performance. These are created using either a referencing procedure similar to section 6.4 [3, 50] or by using the AIS matched ships only and ignoring all other detections [127]. For this dataset, a comma-separated text file is stored with each SAR image and contains the positions of all the ships identified within that image. Each row within this text-file provides the ship's position in Latitude/Longitude coordinates and geocoded image-specific row/columns coordinates. This representation helps when comparing ship detection methods which only provide detected ship positions and helps simplify SAR-AIS ship matching. This format can allow for comparisons between methods that output ship positions as results but for a more refined discrimination system the dataset is also split up using SAR sub-images, as discussed next.

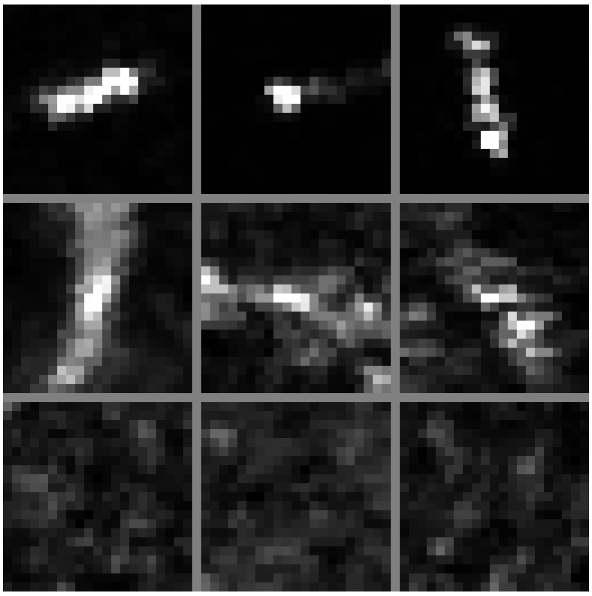

Figure 6.6. Nine sample sub-images from the SAR dataset. The rows consist of positive (ships) [top row], ship-likes false positives [middle row] and ocean clutter false positives [bottom]. The first two columns are Sentinel-1 GRDH and GRDM examples and the last column contains examples from RADARSAT-2 SCNA imagery.

6.4.4.2 Discrimination dataset

While the above data organization is sufficient for comparing most ship detection systems, a more refined, rigid structure is necessary to compare machine learning methods. Many machine learning datasets are available but arguably the MNIST dataset [137] is the most famous and widely-used benchmark machine learning dataset. The fixed size, center-aligned handwritten digits dataset was constructed to allow for fair analysis between methods on a fixed, accessible dataset. To mimic this, the SAR dataset has also organized into a collection of SAR ships and false alarms sub-images similar to MNIST's own 24×24 sized sub-images. The ship identification procedure described above found 1596 ships within the 46 SAR images. Each ship appears at the center of a 21×21 sub-image for consistent comparisons between ships across resolutions and sensors. The entire collection of 1596 SAR ship sub-images with associated reference sub-images shown in Figure 6.5. Details of how these ships are distributed across polarizations, resolutions and sensors is shown in Table 6.2. This table also details the number of hard matched AIS ships, a process is described in section 6.5.2.

False alarms are errors in detection where ship detection methods identify brighter areas incorrectly

Table 6.2. Reference ship distribution per image sensor and polarization.

Sensor	Sentinel-1 (GRDM)				Total	Sentinel-1 (GRDH)				Total	RADARSAT-2 (SCNA)				Total	Combined Total
Polarization	HH	HV	VV	VH		HH	HV	VV	VH		HH	HV	VV	VH		
Total SAR images	0	0	15	16	**31**	4	4	2	2	**12**	3	0	0	0	**3**	**46**
Total Ships	0	0	466	551	**1017**	131	149	93	106	**479**	100	0	0	0	**100**	**1596**
Total AIS Matches	0	0	185	213	**398**	44	46	3	3	**96**	0	0	0	0	**0**	**494**

as ships. For every image a very low global threshold was run over the image and all detections that were not ships were marked as false alarms. This was repeated for all images and generated a total of approximately 500 000 false alarms across the 46 SAR images. Of these a selection of 3192 samples were randomly selected as the false alarm subset to create a dataset of false positives which contains ship ghosts, SAR smearing artifacts, land-object ghosts and nadir (brighter) sea clutter. This is two times as many false positive samples as the number of identified SAR ship examples and represents the distribution of false positives to true positives that should be encountered with careful prescreening threshold design and selection, as described in [4]. For each false alarm a 21×21 SAR sub-image was extracted to match that of the SAR ship sub-images. Both the ship and false sub-images were combined with the patch and reference images, ship attributes and AIS matches into a single ship discrimination dataset containing the bulk of the information required for advanced discrimination method design and evaluation. Figure 6.6 shows a sample of 9 sub-images containing ships and false positives from this dataset.

6.5 TRANSPONDER DATA

The SAR dataset is supplemented by a collection of transponder data using the LRIT and AIS transponder systems. Historical LRIT data has been used in a manner similar to [17] to create a ship distribution map as described in [3]. A more recent AIS dataset is also used to create a ship matching dataset which was used to identify AIS matched ships across all 46 SAR images, both described next.

6.5.1 Ship distribution map

The first method proposed in this study requires a map of ship positions to identify where thresholds can be adjusted for during the SA manifold adaptation [3]. The ship distribution map only requires latitude and longitude points of the ships, so any source of ship positional information can be used such as AIS, SAT-AIS or LRIT data. LRIT data was the original data used in the first study [3] but has been extended here to include an expanded distribution map thanks to the AIS positions available.

The first ship distribution map used in the original method included approximately 450 000 ship latitude and longitude coordinates, recorded over the time period of 2011/03 to 2012/03 off the coast of South Africa. All 12 months of transponder data were used to generate the ship distribution map

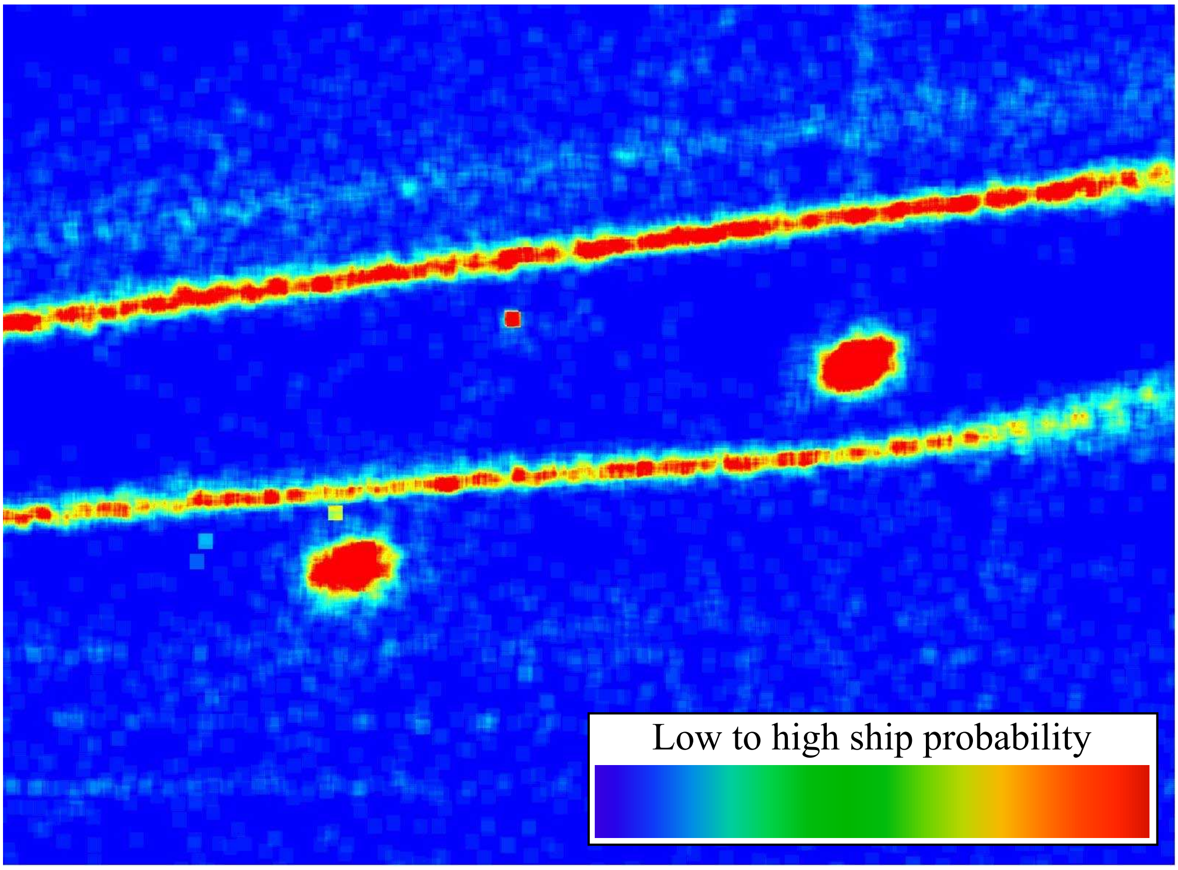

Figure 6.7. A section of the ship distribution map generated using all 12 month's LRIT data within the given geographic region. The image shows the ship distribution map off the coast of South Africa, near Mossel Bay (34.1833° S, 22.1333° E). It is interesting to note that two shipping lanes are clearly visible as well as two platforms. This is due to the fact that thousands of ship positions were collected along those lines, indicating a large number of traversals over those points.

and it was assumed this would sufficiently model the average movement of ships within the image's geographical limits. If enough ship positions were collected over a number of years, a daily, weekly or even monthly ship distribution map for a given region could be generated but for the sake of simplicity all ship positions were combined to create a single distribution map. It should be noted that this was extended to approximately 2 450 000 points using the additional, more recent AIS positions. It was assumed that the original LRIT ship distribution map and the extended version are both indicative of the average ship's movements off of the coast of South Africa. A small sub-image of a ship distribution map off of the South African coast is shown in Figure 6.7.

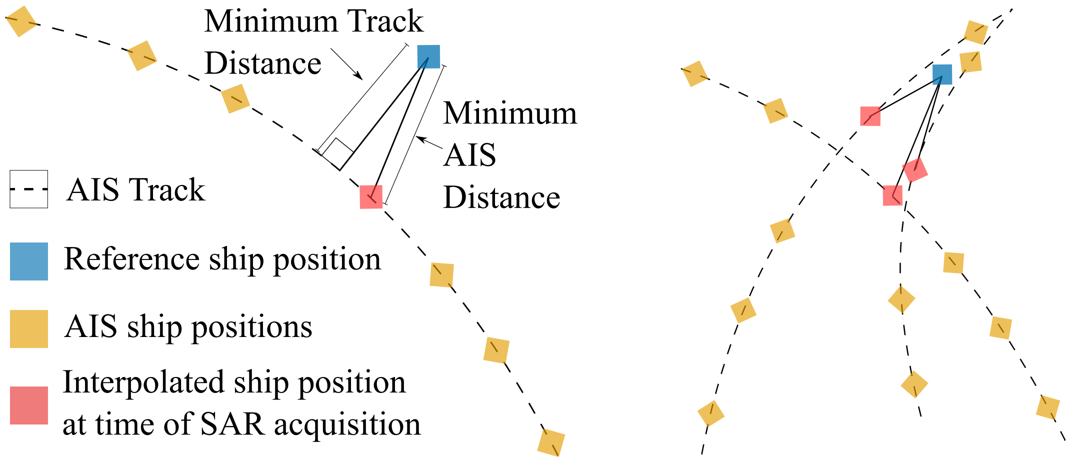

(a) Hard SAR-AIS match

(b) Soft SAR-AIS match

Figure 6.8. Two subfigures showing the different between a hard (a) and soft (b) AIS match. Note that both (a) and (b) use the symbols defined in (a). When a single AIS tracks aligns within a reference ship patch image matches and the track distance, time difference and AIS distance were below the specified minimums a match was recorded. For multiple AIS tracks within the reference patch image area and within the specified parameters a soft match was assigned to the target. Only hard matches were considered in this dataset.

6.5.2 AIS ship identification

The dataset of AIS points that covered and intersected with the SAR dataset includes approximately 2 million satellite and coastal AIS messages obtained from the 6th October 2014 to the 22 July 2015 and covers the majority of South Africa's EEZ.

The last step of the referencing procedure is the matching of transponder-based ship positions to that of the ships within SAR image and this is a vital component in ship detection literature [127, 57, 50, 92]. The process concerns itself with matching the centroid latitudes and longitudes of SAR ships to positions received from the ships themselves. The primary problem with matching AIS to SAR ships is a temporal one. AIS messages may or may not line up with SAR acquisition times and so it is rare that all ships in a SAR image transmit an AIS message at the same time the image was taken by the satellite. To combat this AIS tracks are built using the history of the ship's AIS messages and positions to build a map of the likely area a ship was at any given moment.

For this dataset, all AIS messages 12 hours before and after a SAR acquisition were used to build AIS tracks. An AIS track is a collection of AIS messages built-up over time to indicate the history of a ship and will have either an interpolated AIS position at the time of a SAR acquisition or a fixed AIS message at that time. An interpolated AIS position is the estimated position of a ship at the SAR time of acquisition. This position is created using the time and position of the last AIS message before and first AIS message after a SAR acquisition. If a SAR ship had a single AIS message (interpolated or fixed) within 500m of its position it was deemed to have a hard AIS match as shown in Figure 6.8 (a). If more than one AIS position existed for a single SAR ship and therefore multiple nearby tracks within the 500m window then a ship was said to have a soft AIS match as shown in Figure 6.8 (b). For this dataset, only hard matches were considered to ensure that SAR-AIS matches were of the highest quality with little to no matching ambiguities.

Across all 1596 identified SAR ships only 494 ships were matched to AIS messages. Of these 494, 437 of them were unique matches whereas the additional 57 were AIS matches for the same ship across different polarizations. Unfortunately, the AIS dataset available did not cover any of the RADASAT-2 images near Cape Town harbor and therefore only Sentinel-1 GRDM and GRDH images had AIS coverage (see Table 6.2 for more details). This is an interesting result and it implies that even for a large SAR dataset only approximately 27% of all ships had a matched AIS detection. This could be due to the stringent AIS hard matching but makes another case for SAR imagery as a supplemental source of ship monitoring.

CHAPTER 7 RESULTS AND DISCUSSION

7.1 CHAPTER OVERVIEW

This chapter will present the results and discussion pertaining to the two methods introduced in this thesis. The chapter will provide the metrics against which typical ship detection methods are tested, the results over the dataset described in the previous chapter and an overview in terms of general performance for the two methods. This chapter will also discuss some of the considerations that need to be understood to contextualize the performance. The chapter will be closed with a conclusion that can be drawn from these results.

7.2 METRICS FOR PERFORMANCE

One of the problems with the detection of ships in SAR imagery is a need for a strict agreement among the different performance metrics and their usage in different papers. Across a number of recent studies there exists a multitude of ways to report results, with few similarities between the methods [50, 63, 115, 111, 58, 106, 73]. In addition, the way in which performance is measured varies from study to study and the results need to be critically evaluated before presenting methods as better or worse [118]. In [106], the authors state that they use AIS ship transponder information to verify detections. The authors go on to state how SAR ship detections that do not have matching transponder information are excluded [106]. While this can be used to give a general idea of performance for the ship detector, it completely negates the usefulness of SAR imagery which can circumvent ships that switch off their transponders [17] and could fail to detect any potential ships in an image if useful AIS data is not acquired. In [50], the authors provide a much more comprehensive set of ground truth data including both visually inspected and AIS matched ships but fail to describe the total number of

	Pred. Ship	**Pred. Sea**
Actual Ship	TP	FP
Actual Sea	FN	TN

Figure 7.1. The confusion matrix template. The column headings are the “Predicted as ship” and “Predicted as sea” whereas the row headings are “is an actual ship” and “is actually sea”. This means that TN reads as “Predicted as sea and is actually sea” and similarly for all the other combinations.

false alarms not related to ambiguities their ship detection method incurs. The nomenclature and exact usage of performance metrics becomes important when comparing various methods across different studies and so the following section will describe the exact performance metrics and the statistics used to describe the performance adequately across a large SAR dataset.

7.2.1 Confusion Matrix

Results presented in most ship detection studies can be fully described by a confusion matrix. The confusion matrix is defined by four values, known as True Positive (TP), False Positive (FP), False Negative (FN) and True Negative (TN). The value TP is the number of detections that were correctly labeled as ships whereas FP are the detections incorrectly labeled as ships (sea pixels grouped and labeled as ships). False negatives are the number of detections that were incorrectly flagged as sea pixels whereas TN are the number of sea pixels correctly labeled as sea pixels. The total number of detections is TP+FP+FN+TN. The values in the confusion matrix are arranged as shown in Figure 7.1.

The confusion matrix indicates which category most of the detections are occurring, what problems a detector might be having and if its doing an acceptable job of separating ships from the ocean. One issue with using a confusion matrix to describe results is that a confusion matrix should be defined per image per method per parameter. This can become cumbersome to interpret when there are for instance, 46 SAR images, 4 or more methods, with multiple parameters per method. To this end we introduce three metrics which can help to summarize a confusion matrix’s results. Two are in ship detection literature and one of them helps to overcome some interpretation issues. It should be noted that in ship detection literature TN includes the total number of pixels tested so that FAR results align with other results in literature and a ship/false positive is only counted once despite containing multiple pixels.

7.2.2 Detection Accuracy and False Alarm Rate

Most ship detection literature uses values derived from the confusion matrix to summarize results. The first is the Detection Accuracy (DA) which is the number of correct detections versus the total number of ships. DA is expressed as percentage of the actual number of ships in the image such that $\mathrm{DA} = \left(\frac{\mathrm{TP}}{\mathrm{TP+FN}}\right) * 100$. A $\mathrm{DA} = 100\%$ indicates all ships in an image were detected and correctly identified as ships whereas $\mathrm{DA} = 0\%$ means no ships were identified correctly. False Alarm Rate (FAR) from the confusion matrix refers to the ratio of incorrectly identified to actual sea pixels such that $\mathrm{FAR} = \frac{\mathrm{FP}}{\mathrm{FP+TN}}$. The FAR value is usually described as values ranging from 0 to 1. A $\mathrm{FAR} = 0$ represents zero incorrectly labeled sea pixels whereas $\mathrm{FAR} = 1$ means every sea pixel was incorrectly labeled as a ship. Good detectors on typical SAR images have $FAR \approx 10^{-7}$ to 10^{-9} however this is dependent on how many total pixels are tested. It is good practice to note the total number of detections to give context to how well the detector is doing. A detector might appear to have an excellent FAR rate of 10^{-9} but if the total number of pixels tested is 10^{13} then the detector is identifying approximately 10^{4} false positives (which may or may not be acceptable depending on the evaluation situation). This is not a problem when using the confusion matrix as the number of pixels is apparent but does become a problem when using FAR to summarize the detectors performance across a number of images. Any FAR results given in this study will state the number of pixels (or average thereof) tested against, rounded to the nearest whole number.

7.2.3 Matthews Correlation Coefficient

In almost all SAR ship detection literature DA and FAR is used to describe the performance of a ship detector in one form or another [18, 17, 74, 3, 4, 75]. One issue that was identified during research was that some situations may require high DA with no regard to FAR whereas in other situations a low FAR was more important to the development and assessment of the method. Ideally, DA would be 100% and FAR would 0 but real-world situations demand a trade-off between these two (most notable due to the Neyman-Pearson criterion for binary detections [130]) and some way to objectively identify whether one trade-off is “better” than the other. To do this the Matthews Correlation Coefficient (MCC) [141], often used in machine learning literature, is introduced as a recommended metric for performance evaluation of SAR ship detectors. The MCC can be defined from the confusion matrix as

$$\mathrm{MCC} = \frac{\mathrm{TP} \times \mathrm{TN} - \mathrm{FP} \times \mathrm{FN}}{\sqrt{(\mathrm{TP}+\mathrm{FP}) \times (\mathrm{TP}+\mathrm{FN}) \times (\mathrm{TN}+\mathrm{FP}) \times (\mathrm{TN}+\mathrm{FN})}}. \tag{7.1}$$

MCC values are defined such that $\mathrm{MCC} \in \{-1.0, 1.0\}$ which range from perfectly decorrelated (-1.0) to perfectly correlated (1.0) with a value in the center (0.0) indicating no correlation/random detections. The MCC is particularly useful to SAR ship detection literature as it takes all factors in the confusion matrix into account equally. It is also unbiased by data with skewed classes [141]. This last point is of particular importance to SAR ship detection because while there may be on average 20 ships in an image, the detector tests millions of sea pixels and thus the ship detections problem is actually a highly class-imbalanced problem which means DA and FAR do not objectively count equally towards performance descriptions and the MCC helps to alleviate this discrepancy.

7.2.4 Moments

In addition to performance metrics defined in terms of the confusion matrix we need to measure these for multiple images and in this sense we can use statistics to summarize these values. The mean is often used to describe the average or expected performance across the whole range of tested values. The variance gives us an indication of how far the performance is spread across the range of values which determines how much from the mean, both positively and negatively, the detector will perform for any given situation. Finally, we also report on the skewness of the results to provide a description on the distribution of variance. Negatively skewed results indicate that the detector will more consistently provide results above the mean than below and vice versa for positively skewed results. For instance, some usage scenarios might require the DA be more often as good as or better than the mean DA and so a negatively skewed DA result might be better whereas a FAR with a close to zero skew would indicate the mean FAR is more or less the final expected performance of the detector.

7.2.5 Receiver Operating Characteristic Curve

The Receiver Operating Characteristic (ROC) curve describes the performance of a binary classification task under some variation of one (or more) of its parameters, but can be extended to more than two classes [130]. As the chosen parameter is varied the performance of the system changes and the ROC curve reports the results. An ROC curve is constructed with the methods true positive rate performance on the y-axis and the false positive rate performance on the x-axis. Curves closer to the top left corner indicate better performers with those closer to the diagonal worse. A common metric used in conjunction with ROC curves is the Area-Under-Curve (AUC) value. An AUC = 1 is a perfect discriminator while a discriminator with AUC = 0.5 is essentially selecting results randomly [130].

7.3 PARAMETER SELECTIONS

For every method developed and tested against has a number of method parameters that can be adjusted. Each of these have varying degrees of effect on the performance of the ship detection system. Table 7.1 details the full list of parameters, which are fixed and which are adjusted for the ROC curve in section 7.4.3.

7.3.1 CFAR Variants

There are 3 CFAR variants tested in this thesis, namely the two common ones CA-CFAR and GO-CFAR [64] as well as the non-flat version (abbreviated as CA-CFAR NF) described in section 5.3.3 and [3]. They all three mainly rely on the threshold T_C and less so on the guard and clutter window sizes, S_G and S_C respectively. This is because the variation in the window sizes will be accounted for due to the variable calculation of μ_C with the related fixed threshold T_C [64, 18]. Variations in S_G and S_C affect the values of μ_C but these can be accounted for by varying T_C (as is done in the results). For the case of the non-flat CA-CFAR Manifold, the threshold is linearly decreased from $T_C^{min} = 1.0$ along the nadir of the image to T_C^{max} at the end of the swath. This is because ships are relatively brighter at the end of the swath and thus should be under greater scrutiny (i.e. higher threshold should still allow bright ships through at the end of the swath) whereas ships near the swath cannot always be much brighter than the bright nadir returns. T_C^{min} can also be varied but setting it at 1.0 gives a good indication of the minimum expected performance of the detector given the worst (lowest) case threshold.

7.3.2 Newest Ship Detection Methods

The rest of the methods tested are the novel methods developed in this thesis or those that have shown good results on SAR imagery in previous studies and could be replicated. The CA-CFAR SA Manifold

Table 7.1. List of parameters for the methods tested, including the fixed and varied parameters. Note that SAR_{max} is typically either 255 for 8-bit images or 65536 for 16-bit SAR images but can be reduced to $\text{SAR}_{\text{max}} = 20$ which will cover almost all situations and reduce processing time. Also note that $S_{\text{ROI}} = 1$ for all CFAR methods tested and methods marked with a "*" indicate novel methods described in this thesis.

Methods	**List of Parameters**	**Fixed Parameters**	**Variable Parameter Range**
CA-CFAR [64]	T_C, S_G, S_C	$S_G = 17, S_C = 15$	$T_C \in [1,5]$ (low), $T_C \in (5, \text{SAR}_{\text{max}}]$ (high)
GO-CFAR [64]	T_C, S_G, S_C	$S_G = 17, S_C = 15$	$T_C \in [1,3]$ (low), $T_C \in (3, \text{SAR}_{\text{max}}]$ (high)
*CA-CFAR NF [3]	$T_C^{\text{min}}, T_C^{\text{max}}$, S_G, S_C	$T_C^{\text{min}} = 1.0$, $S_G = 17, S_C = 15$	$T_C^{\text{max}} \in (1, \text{SAR}_{\text{max}}]$
*CA-CFAR SA [3]	T_C, S_G, S_C $N, \Delta D$	$T_C = 1.0, S_G = 17$, $S_C = 15, \Delta D \in [0, 10]$	$N \in [1, 1 \times 10^4]$
HAAR Upright [128]	DA_{train}, $\text{FAR}_{\text{train}}$, L, f_j	$\text{DA}_{\text{train}} = 95\%$, $\text{FAR}_{\text{train}} = 10 \times 10^{-3}$, $f_j \, \text{where} \, j = 1 \dots 111160$	$L \in [1, 10]$
HAAR Full [129]	DA_{train}, $\text{FAR}_{\text{train}}$, L, f_j	$\text{DA}_{\text{train}} = 95\%$, $\text{FAR}_{\text{train}} = 10 \times 10^{-3}$, $f_j \, \text{where} \, j = 1 \dots 155060$	$L \in [1, 10]$
*CHAAR Upright [4]	S_G, S_C, T_C DA_{train}, $\text{FAR}_{\text{train}}$, L, f_j	$S_G = 17, S_C = 15, T_C = 1.0$, $\text{DA}_{\text{train}} = 95\%$, $\text{FAR}_{\text{train}} = 10 \times 10^{-3}$, $f_j \, \text{where} \, j = 1 \dots 111160$	$L \in [1, 10]$
*CHAAR Full [4]	S_G, S_C, T_C DA_{train}, $\text{FAR}_{\text{train}}$, L, f_j	$S_G = 17, S_C = 15, T_C = 1.0$, $\text{DA}_{\text{train}} = 95\%$, $\text{FAR}_{\text{train}} = 10 \times 10^{-3}$, $f_j \, \text{where} \, j = 1 \dots 155060$	$L \in [1, 10]$
SVM Classifier [94]	S_G, S_C, T_C f_j, γ, α	$S_G = 17, S_C = 15$, $f_j \, \text{where} \, j = 1 \dots 14$, $\alpha = 1.0$	$T_C \in [1, \text{SAR}_{\text{max}}]$, $\gamma \in [1 \times 10^{-1}, 1 \times 10^{1}]$
Mod. Otsu's [69]	$\text{Min}_{\text{num}}, \text{Max}_{\text{num}}$, $\text{Min}_{\text{size}}, \text{Max}_{\text{size}}$	$\text{Min}_{\text{num}} = 2, \text{Max}_{\text{num}} = 135$, $\text{Min}_{\text{size}} = 1$	$\text{Max}_{\text{size}} \in (1, 20]$
H-dome [6]	$\sigma_L, \mathcal{O}, d$	$\sigma_L = 1.0, d = 5$	$\mathcal{O} \in [0.9 * \text{SAR}_{\text{max}}, 1.0 * \text{SAR}_{\text{max}}]$

Adaptation method (abbreviated as CA-CFAR SA) had only one variable, the number of iterations N, which was varied with the other variables remaining fixed as described in [3]. Similarly, for all Haar-like variants the length of the final cascade affects the performance most critically and was varied between 1 and 10 [128, 129, 4]. Longer cascade lengths could be tested, but previous results show that lengths longer than 5 show degraded performance and lengths greater than 5 are shown here for completeness [4]. The CA-CFAR Haar-like feature cascaded classifier for ship detection method has been abbreviated as CHAAR for all the results [4]. The methods were tested against the original Haar-like classifiers (abbreviated as HAAR), with both upright and full (rotated + upright) features tested. They were also tested against a Modified Otsu's method built specifically for ship detection [69], an OC-SVM ship detector based on features extracted per sample [94] and an H-dome ship detector [6]. The Modified Otsu's method had a few parameters that could be adjusted, with the maximum ship size determining how groupings were made and the others determined as per the original paper [69, 3, 4]. The SVM classifier used a CFAR variant as prescreening with a variable threshold T_C and SVM classifier with γ which was varied (γ is the inverse of the radius of influence of samples selected by the model as support vectors). Finally, the H-dome methods parameters were chosen as those described in the paper [6], with the h-dome size parameter $\mathcal{O}$ parameter varied between 90% and 100% of the maximum SAR value within each image.

7.4 RESULTS

The results section is divided into three subsections: an overview describing the average performance, a subsection which describes performance variations in terms of training data redundancy and ROC curves to describe performance under parameter variations and a single image example with all the confusion matrices and in-depth look at specific results.

7.4.1 Overall

It should be noted that wherever results include stochastic components the method was tested using a k-fold cross validation technique with $k = 5$ [130]. The entire dataset of 1596 positive (ship) and 3192 negative (sea clutter) samples were randomized and split into 5 (roughly) equal sized groups. The methods were then trained with 4 of the groups and tested with the other and this was repeated 5 times

Table 7.2. Mean DA, FAR and MCC results for the different systems tested across 5-fold cross validations with a total of 1596 ships in total tested with an average number of pixels being approximately 300×10^6. The values in brackets are the variance and skewness values, respectively.

Method	**DA**	**FAR**	**MCC**
CA-CFAR Low	$100.0\,(0.00, \text{N/A})$	$8.825 \times 10^{-07}\,(5.952 \times 10^{-07}, 1.13)$	$0.41\,(0.03, -1.42)$
CA-CFAR High	$64.99\,(1.17, 0.39)$	$2.857 \times 10^{-07}\,(1.879 \times 10^{-07}, 1.11)$	$0.43\,(0.04, -0.29)$
GO-CFAR Low	$95.62\,(1.64, -0.45)$	$8.825 \times 10^{-07}\,(5.954 \times 10^{-07}, 1.13)$	$0.39\,(0.08, -0.57)$
GO-CFAR High	$81.39\,(1.75, -0.50)$	$8.800 \times 10^{-07}\,(5.959 \times 10^{-07}, 1.14)$	$0.34\,(0.15, 0.55)$
CA-CFAR NF	$100.0\,(0.00, \text{N/A})$	$2.350 \times 10^{-07}\,(1.110 \times 10^{-07}, 0.46)$	$0.64\,(0.07, 1.07)$
CA-CFAR SA	$87.51\,(1.40, 1.46)$	$5.644 \times 10^{-08}\,(4.307 \times 10^{-08}, 1.17)$	$0.80\,(0.04, 0.20)$
HAAR Upright	$55.62\,(1.79, 0.09)$	$6.833 \times 10^{-09}\,(3.073 \times 10^{-09}, 0.72)$	$0.72\,(0.01, 0.78)$
HAAR Full	$56.79\,(2.54, 0.65)$	$1.217 \times 10^{-08}\,(1.112 \times 10^{-08}, 1.39)$	$0.71\,(0.02, -0.42)$
CHAAR Upright	$88.71\,(1.97, 0.18)$	$1.940 \times 10^{-08}\,(7.533 \times 10^{-09}, 0.42)$	$0.89\,(0.01, -0.95)$
CHAAR Full	$84.89\,(3.28, -0.50)$	$9.553 \times 10^{-08}\,(8.082 \times 10^{-08}, 1.26)$	$0.81\,(0.06, -0.42)$
SVM	$88.68\,(1.61, 0.06)$	$1.197 \times 10^{-07}\,(1.639 \times 10^{-07}, 1.25)$	$0.66\,(0.09, -0.15)$
Mod. Otsu	$91.76\,(1.39, -0.10)$	$3.344 \times 10^{-07}\,(2.884 \times 10^{-07}, 1.12)$	$0.52\,(0.19, -0.15)$
H-dome	$92.44\,(0.68, -0.53)$	$4.078 \times 10^{-07}\,(2.990 \times 10^{-07}, 1.20)$	$0.41\,(0.05, -0.62)$

by replacing the testing group with one of the other 4 groups. Results presented then represent the average performance across the 5 test results including standard deviation and skewness values.

The results of the overall comparison is shown in Table 7.2 and Figure 7.2. The table shows the three main forms of performance metrics used in determining ship detector performance. These show the results of using the best performing parameters shown in Table 7.1. There were 5 methods that performed above 90% DA including CA-CFAR Low, CA-CFAR NF, GO-CFAR Low, the Modified Otsu's and H-Dome. The first two achieved 100% across all k-fold and was to be expected as these methods highlight every ship, with little regard for the amount of false alarms generated. Similarly, the other three methods scored above 90% but all of them had at least 2.3×10^{-7} false alarms which translates to approximately 72 false alarms for a typical SAR image with 300 million sea pixels. All 5 of these methods show smallest variances in DA because they were all designed to hit these goals of consistent ship detection with more false alarms. Of the 5, the methods with a skew value were all negative indicating that the results are more likely to be above the mean. These 5 methods all showed MCC results in the range of 0.39 – 0.64, with the CA-CFAR NF showing the best MCC of 0.64 across the 5-folds. This shows that a low MCC value is obtained when the FAR is high, even if the DA is 100%.

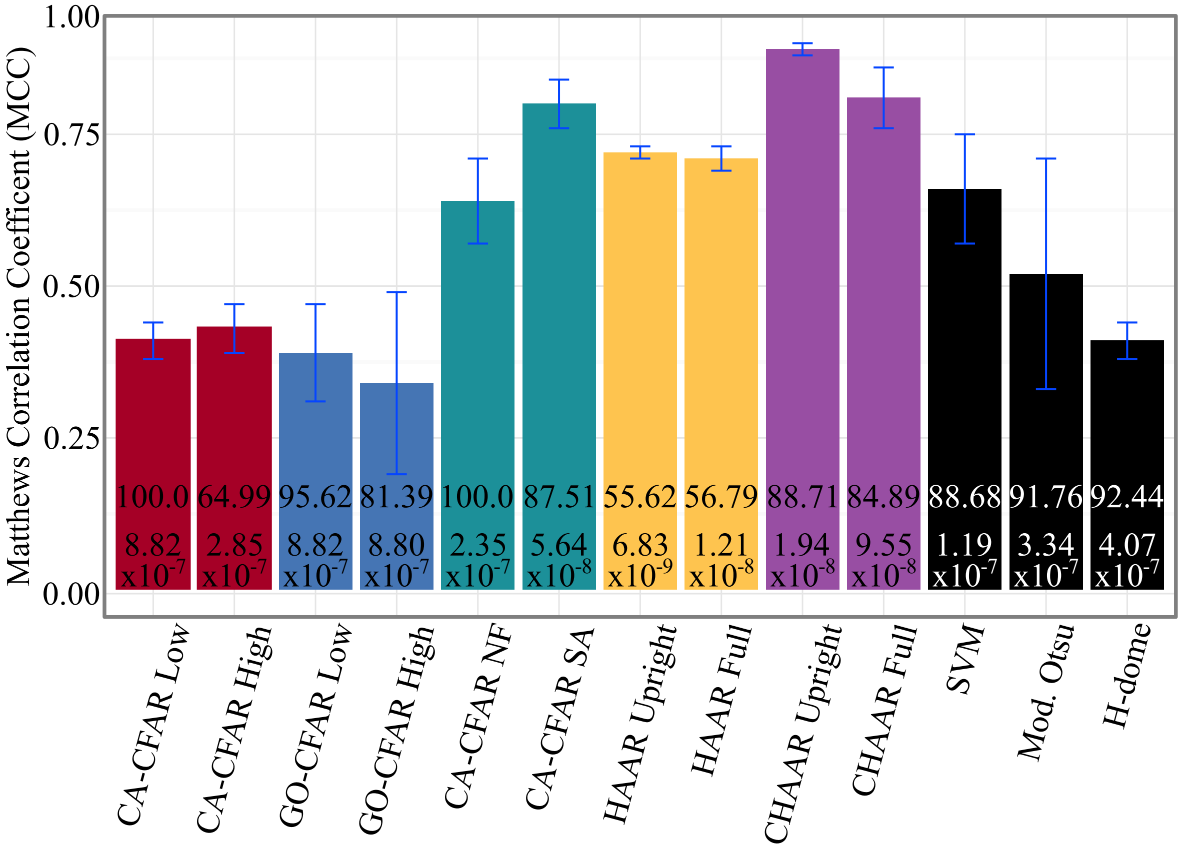

Figure 7.2. The figure shows a bar graph of the MCC values from Table 7.2 for each ship detection method. The error bars are the variances shown in the table and the numbers are the mean DA (top) and FAR (bottom).

If we move towards methods with better FAR we see a drop of approximately 11-16% in average DA across the 5-fold cross validation scheme. The CA-CFAR SA, CHAAR Upright, CHAAR Full and SVM methods all had DAs of above 84% but yielded at least twice as better FAR compared to the methods discussed above. Specifically, the CHAAR Upright method achieved an 88.71% accuracy with an average FAR of 1.940×10^{-8}, almost an order of magnitude better than the SVM which had 4% better DA. Similarly, the CA-CFAR SA achieved a mean DA of 87.51% yet had a FAR twice as good as the SVM method. Interestingly, only the CHAAR Full had a negative DA skewness value with the rest showing positive DA skewness indicating that the four other methods have results below the mean but their best-case results are above the mean. Again, except for the CHAAR Full, all the methods had DA variances below 2.0 so the performances for the best parameters seemed quite stable. The FARs for these 5 methods ranged from 1.197×10^{-7} to 1.940×10^{-8}, all with variances of less than 1.639×10^{-7}. These 5 methods also all had positive skewness which indicates that the FAR results were below the mean with a few select samples being higher. This is a positive result because FARs below the reported value means improved results and is not unexpected as these methods were designed to improve discrimination thereby lowering FAR. Finally, the 4 methods had MCC values ranging from 0.66 – 0.89 with the CHAAR Upright having the best MCC of all the methods tested as shown in Figure 7.2. The CA-CFAR SA had a positive MCC skewness, whereas the rest all had negative skewness with the CHAAR method having the lowest skewness of the three at -0.95.

The four other methods not discussed above were the CA-CFAR High, GO-CFAR High, HAAR Upright and HAAR Full. These four methods either failed to have an acceptable DA (HAAR Full and Upright score around 55%) or the drop in DA did not yield acceptable drops in FAR (CA-CFAR High and GO-CFAR High). These are included for discussion purposes but do not meet an acceptable level of ship detection performance in most cases. It is interesting to note that the MCC values are in the 0.70 range for the HAAR Upright and HAAR Full methods because they have significantly lower FARs compared to the other methods.

7.4.2 Performance Variations

The methods tested in Table 7.2 represent the best case scenarios for all the methods tested. While this does give a good indication of what average the performance of the methods might be especially when using 5-fold cross validation, variance and skewness, a more complete performance description can be made. To do this the methods were also tested to see how their performance varies when adjusting their most influential parameters as well how each method performed when the amount of testing data is varied.

7.4.2.1 Receiver Operating Characteristic Curve

As mentioned in section 7.2.5, we can determine the performance of the various methods by varying a parameter as set out in Table 7.1. Figure 7.3 shows the ROC curves for the 13 methods tested in this thesis. Only a small fraction of the possible 18.4×10^9 pixels across the 46 images would ever be seen by the ship discrimination methods presented here. This is because the ship prescreening method (generally CA-CFAR) would eliminate the majority of potential false alarms, even with a low threshold. The false positive rate of the ROC curve shown here is more indicative of the sub-images

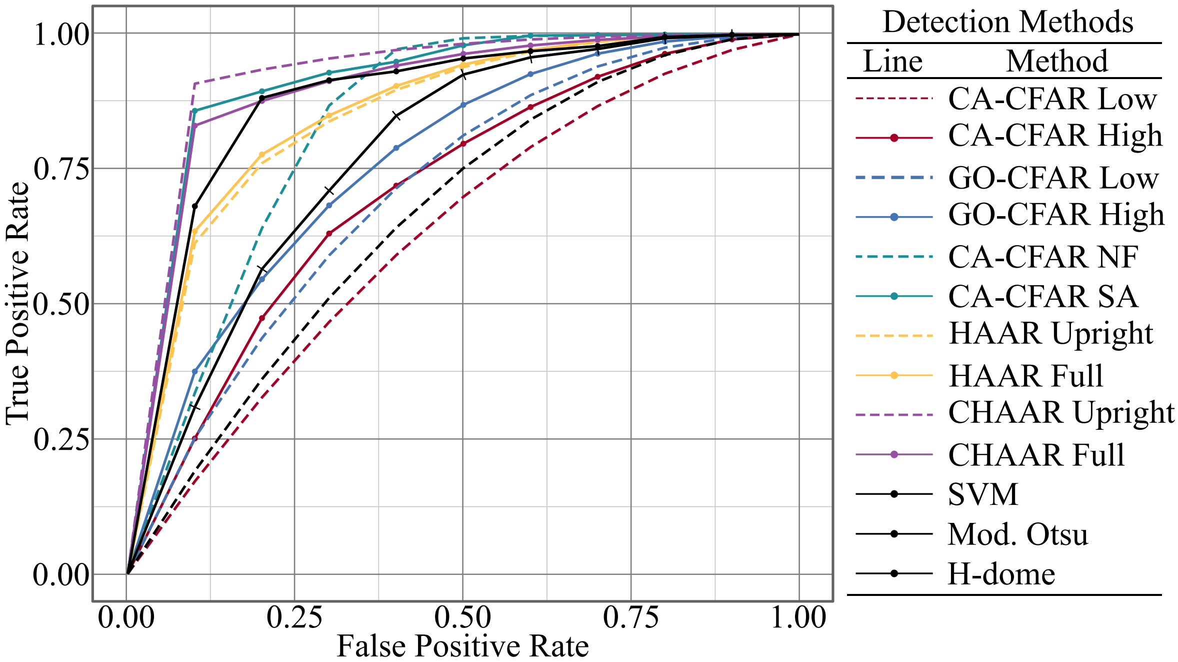

Figure 7.3. ROC curves for the 13 methods under test. The table to the right shows the method's line shape and what AUC it scored. This False Positive Rate is scaled for display purposed compared to the results in Table. 7.2. The parameters varied are shown in Table 7.1.

that the ship discrimination stage would see and thus the false positive rates differ from per-pixel classifiers and are scaled from 0 to 1 for display purposes. Variant of a single method had the same line color but different shapes. The last three methods were colored black but are not necessarily related. Closest to the diagonal is the CA-CFAR Low method with an AUC of 0.6311, indicating the lowest performing method across all the methods tested. The method with the highest AUC is the CHAAR Upright method with an AUC of 0.9235. The CA-CFAR and GO-CFAR follow similar patterns with the GO-CFAR doing better with a higher threshold. The CA-CFAR NF breaks this smoothly varying behavior and has a larger AUC than either the CA-CFAR or GO-CFAR methods. The HAAR and CHAAR methods largely follow the same curve pattern with the Upright version doing better in the CHAAR case and the Full version doing better in the HAAR case.

7.4.2.2 Redundancy

These tests aim to identify what is the minimum acceptable amount of data necessary to train the various methods and how each method performs when a minimum amount of training data is not

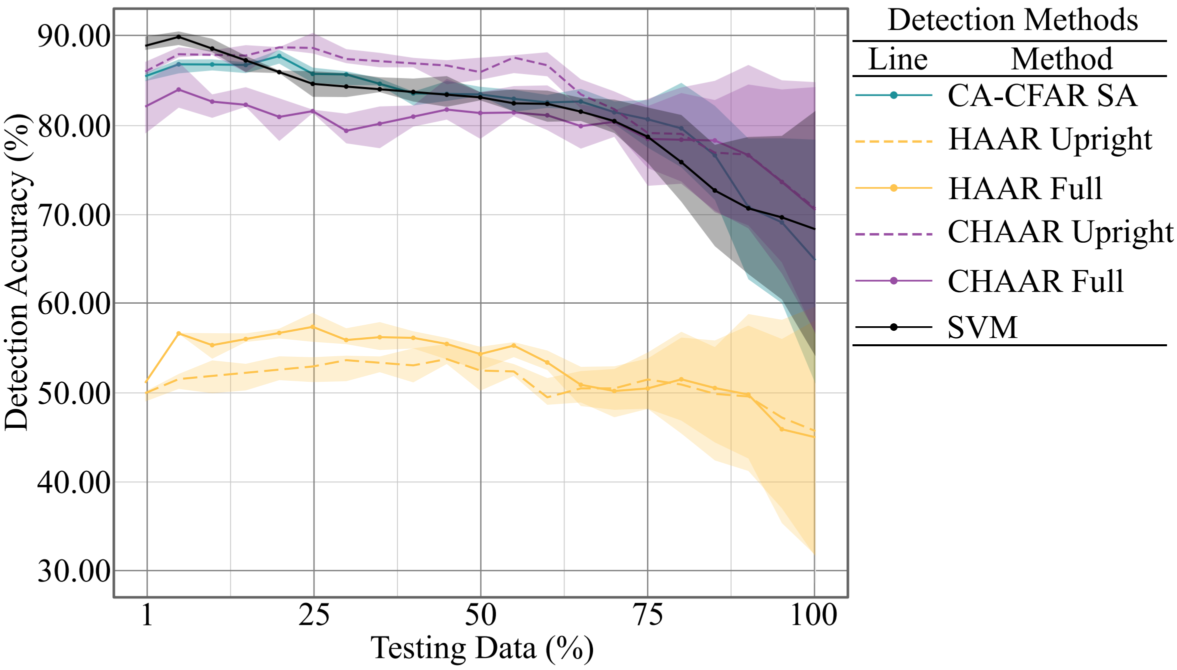

Figure 7.4. Redundancy curve for DA using all the stochastic methods.

present. The methods' parameters were fixed with the best performing parameters and the amount of data used for testing was varied from 1% to 100% The results for the DA, FAR and MCC metrics are shown in Figure 7.4, 7.5 and 7.6, respectively. It should be noted that only methods with stochastic components were considered for this section as the other methods did not use any data to train their systems and thus varying the amount of testing data had little to no effect on their performance. That is, a CA-CFAR system would perform similarly given one or twenty test images (assuming the correct parameters were chosen).

For Figure 7.4 all methods start with slightly lower DAs. This is largely due to overfitting because at 1% testing data the systems are given 99% of the data to train on where they are unlikely to learn the intrinsic patterns of the data but rather the data itself. These patterns are repeated in the FAR and MCC redundancy curves shown in Figure 7.5 and 7.6.

In Figure 7.4 the HAAR variants are significantly lower and approaches random when the available testing data is set to 60% or above. This indicates that below this amount of data these methods would not likely to be trained correctly which sets a minimum on the amount of data necessary. The other methods converge on similar DAs, even with a small amount of training data. This is likely due to the other methods being based on the low threshold CA-CFAR and an improvements or decreases

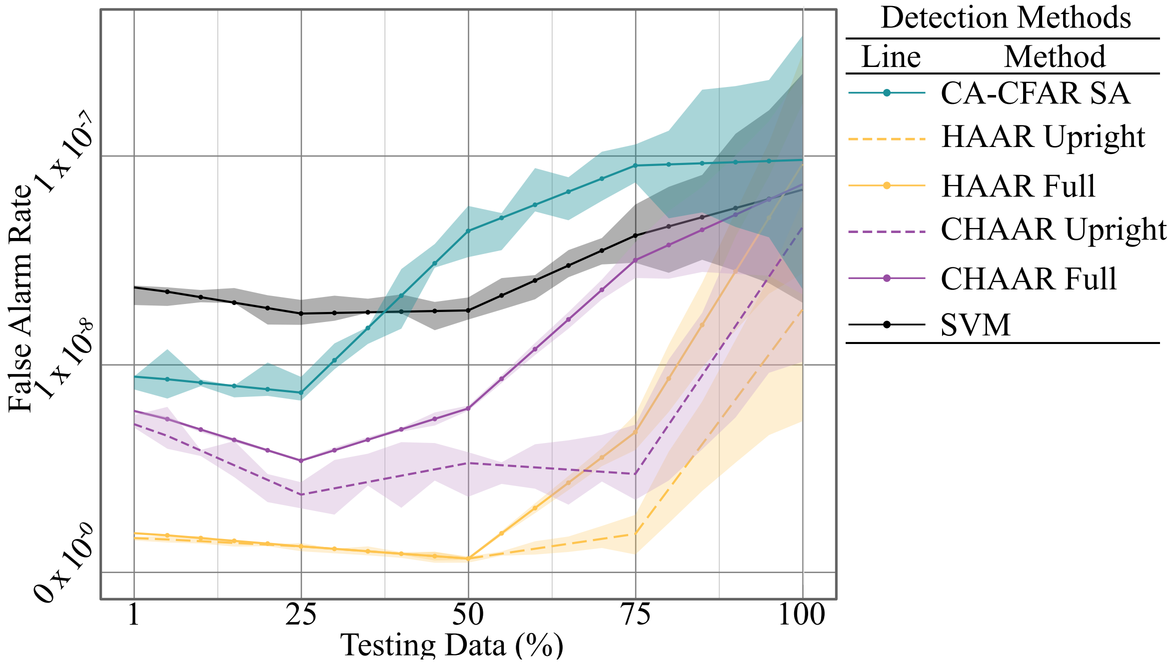

Figure 7.5. Redundancy curve for FAR using all the stochastic methods.

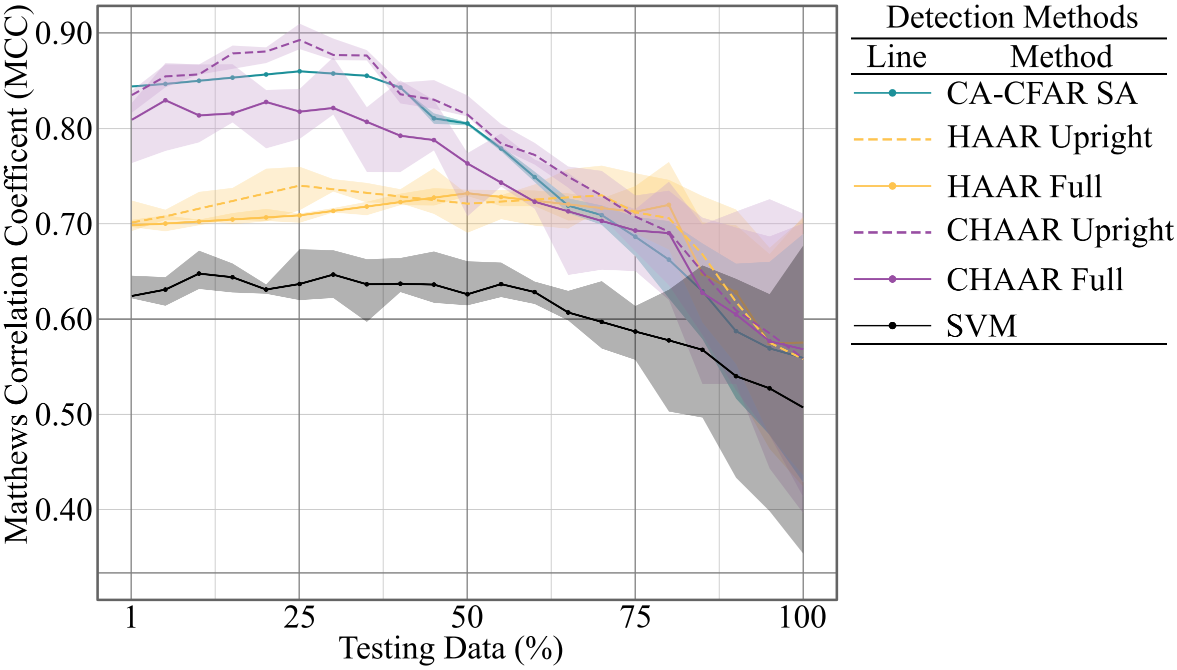

Figure 7.6. Redundancy curve for MCC using all the stochastic methods.

Table 7.3. This table shows the confusion matrices values TP, FP, FN and TN in a simplified format with each method's associated DA, FAR and MCC for the specific SAR image Figure 7.7. The MCC values for each method are plotted in Figure 7.8.

Name	**TP**	**FP**	**FN**	**TN**	**DA**	**FAR**	**MCC**
CA-CFAR Low	55	322	0	314218025	100.0	1.02×10^{-6}	0.381
CA-CFAR High	36	120	19	314218227	65.45	3.82×10^{-7}	0.388
GO-CFAR Low	53	180	2	314218167	96.36	5.73×10^{-7}	0.468
GO-CFAR High	45	110	10	314218237	81.81	3.50×10^{-7}	0.487
CA-CFAR NF	55	54	0	314218293	100.0	1.72×10^{-7}	0.710
CA-CFAR SA	48	12	7	314218335	87.27	3.82×10^{-8}	0.835
HAAR Upright	30	2	25	314218345	54.54	6.37×10^{-9}	0.715
HAAR Full	31	6	24	314218341	56.36	1.91×10^{-8}	0.687
CHAAR Upright	49	5	6	314218342	89.09	1.59×10^{-8}	0.899
CHAAR Full	48	24	7	314218323	87.27	7.64×10^{-8}	0.762
SVM	50	37	5	314218310	90.90	1.18×10^{-7}	0.722
Mod. Otsu	50	40	5	314218307	90.90	1.27×10^{-7}	0.710
H-dome	50	188	5	314218159	90.90	5.98×10^{-7}	0.437

with less training data works with or against the base CA-CFAR method (which also accounts for the large variance in results at 99% training data). Similar results are found in Figure 7.5 and 7.6. Lastly, the larger FAR across most of Figure 7.5 for the SVM method contributes to its low MCC score in Figure 7.6 however, the variances and decrease in MCC is less pronounced than either CHAAR variants.

7.4.3 Single Image Analysis

An examination of the methods on a single image was taken and shown in Figure 7.7. This experiment demonstrates how the above general performance indicators translate to a specific image and how various methods perform in terms of centroid placement While not every method is shown in Figure 7.7 for brevity, a confusion matrix for the results of the 13 methods tested with their best parameters is shown in Table 7.3 and Figure 7.8.

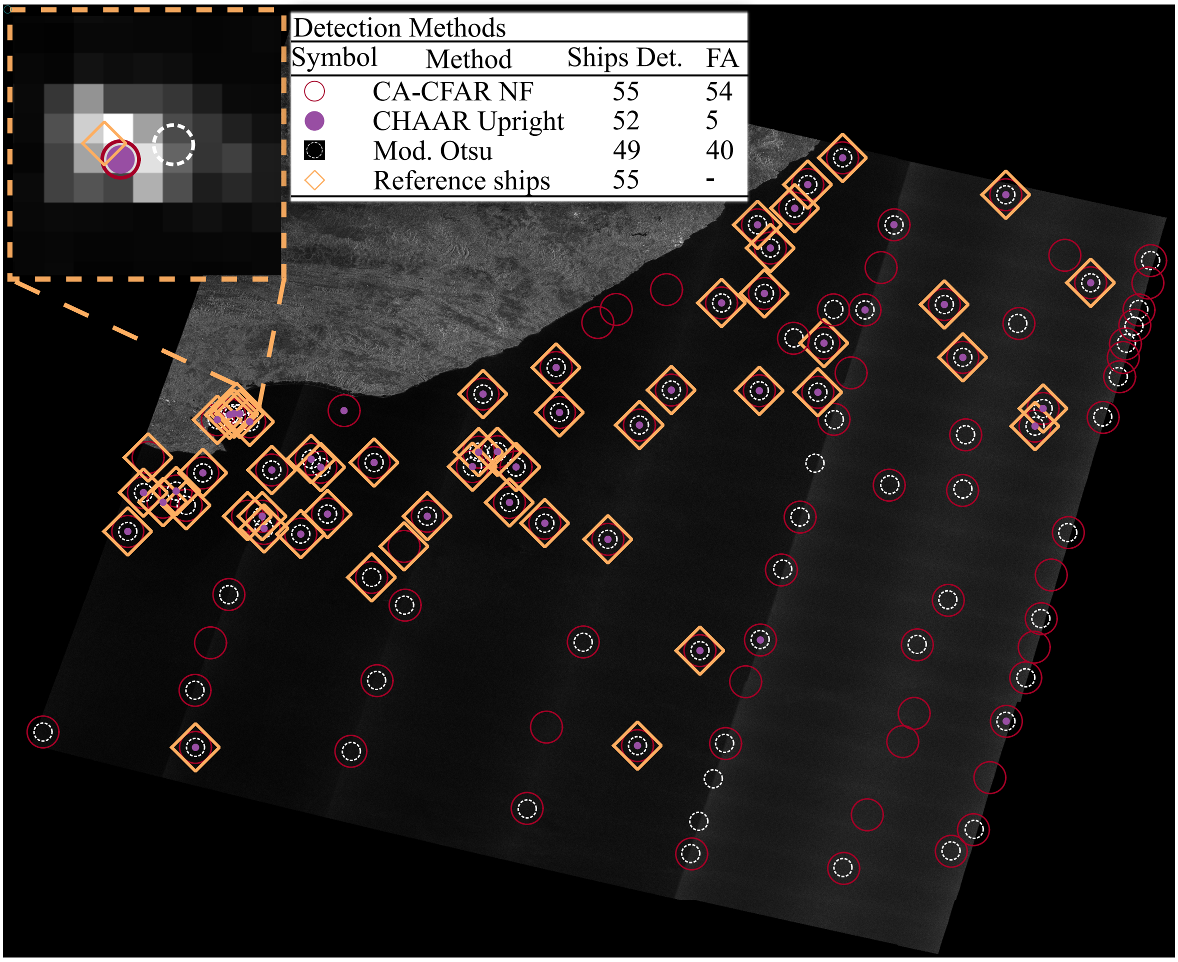

Detection Methods

Symbol	Method	Ships Det.	FA
○	CA-CFAR NF	55	54
●	CHAAR Upright	52	5
◙	Mod. Otsu	49	40
◇	Reference ships	55	-

Figure 7.7. Sentinel-1 GRDM VV image between Port Elizabeth and East London, South Africa (33°57′29″S 25°36′00″E). The image shows 55 reference ships and the detection results of the CHAAR, CA-CFAR NF and Modified Otsu's method. The CHAAR has significantly lower number of false alarms (5 vs. 40 for the Mod. Otsu's) with only three missed detections. The cutout also shows the sub-pixel positional accuracy of the proposed ship detection method.

Figure 7.7 shows a Sentinel-1 GRDM VV image taken on the 25th June 2015 near Port Elizabeth, South Africa. The figure shows 55 reference ships (diamonds icons) spread across the image and the results of applying the CA-CFAR NF (red circle), CHAAR Upright (purple dot) and Modified Otsu's method (white circle) to this image. The CA-CFAR NF missed none of the ships where the Modified Otsu's missed two ships and the CHAAR method missed three. However, the CA-CFAR NF and Modified Otsu's detected 54 and 40 false alarms, respectively, whereas the CHAAR detected 5. A number of the false alarms occur in line with the azimuth direction. As the Sentinel-1 imagery is composed of 5 subwaths that are pieced together to form the entire SAR image the divide between

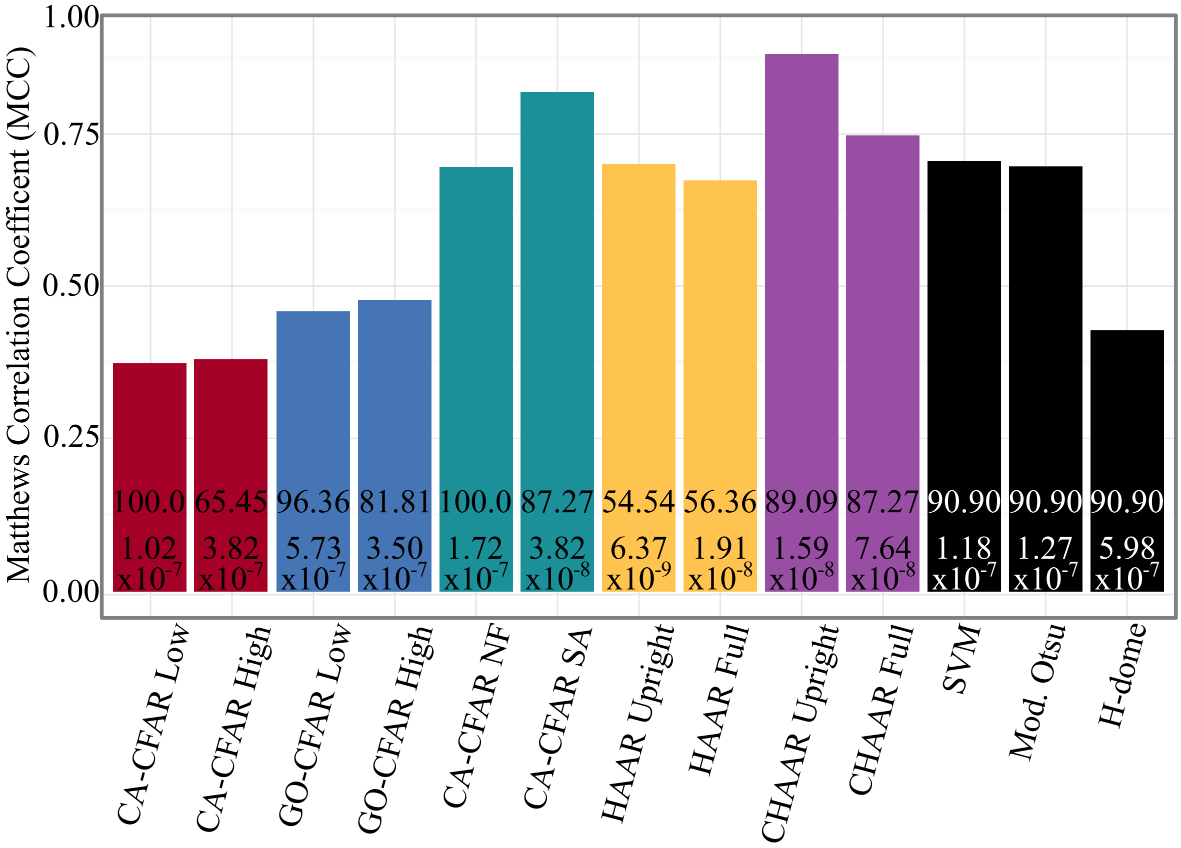

Figure 7.8. The figure shows a bar graph of the calculated MCC, DA and FAR values from the confusion matrices values shown in Table 7.3 for each ship detection method. The values inside each bar represent the DA (top) and FAR (bottom).

each subswath has higher backscatter than further down in the subswath creating visible strips in the SAR imagery. Unless the methods are set to a) high thresholding values or b) specifically designed to reduce false alarms the divides represent a major change in SAR pixel value which can manifest as ships. This is evident with the number of detections along these subswath lines. In general, the more advanced methods circumvent these errors by using either machine learning or size-based filtering to identify these as false alarms.

To get a better perspective of how exactly these results compare for all the methods, Table 7.3 lists all of the tested method's confusion matrices values for this image. These are summarised as MCC, DA and FAR values in Figure 7.8. The confusion matrices provide a description of the difference between a FAR of 10^{-7} and 10^{-9} as well as giving exact understanding to how many ships are missed by each method. When using a low-threshold CA-CFAR we see about 322 false alarms (FAR of

8.82×10^{-7}) but by applying the HAAR-like cascade classifier to this the number of false alarms are reduced to around 5 and 24 (FAR of 1.94×10^{-8} and 9.55×10^{-8}, respectively) for the Upright and Full CHAAR variants. This massive reduction in false alarms is precisely why the HAAR-like classifier was chosen (the standard HAAR methods had 2 and 6 false alarms, respectively). The SVM, while built to maintain a high detection accuracy, failed to provide better DA in this example compared to the CHAAR or CA-CFAR SA method whereas the Modified Otsu's did provide the same or better detection accuracy, at the cost of a relatively large number of false alarms.

In addition to the above, the small cutout in the top left corner of Figure 7.7 shows the positional accuracy for a single example ship. The Modified Otsu's suffers with regards to positional accuracy with an average pixel error of 1.78 versus 0.68 for the CA-CFAR and CHAAR methods. This is likely due to the global threshold approach of the Modified Otsu's method compared to the local, adaptive threshold provided by the CA-CFAR and CHAAR methods. The global approach highlights more pixels which moves the mean centroid further away from the reference (diamond) position. The CA-CFAR NF and CHAAR share the same positional accuracy because both use the CA-CFAR method as the initial detection and therefore position.

7.5 DISCUSSION

A difficult task in ship detection literature is understanding what an acceptable trade-off between DA and FAR is. At what reduction in FAR makes a method with a DA of 85% acceptable versus another method with a 95% DA? The answer to these types of questions is largely based on the application scenario in which the ship detection method is to applied to. Some require very high DA whilst others require a low FAR. To try and understand results in the more general case (without a specific application in mind) the MCC (and AUC) is introduced to objectively measure what is an acceptable trade-off. The simple CFAR (CA-CFAR/GO-CFAR) methods clearly had the best DA at low threshold values but their corresponding FAR were at least an order of magnitude higher than the other methods. This indicates that these methods cannot be used on their own to detect ships with a low number of false alarms for the given SAR dataset, irrespective of the parameters used. On the other hand, the standard HAAR methods have an excellent FAR reduction but at the cost of severe DA degradation. The strengths of both of these methods are used in the proposed CHAAR method and the results show that by combining the CA-CFAR and Haar-like cascade classifier performance is improved over either method. Similarly, by extending the simple CA-CFAR method and incorporating external knowledge (historical ship positions) the CA-CFAR SA method performed nearly as well as the CHAAR Upright method for the various metrics provided. Both the CA-CFAR SA and CHAAR Upright methods had a drop in maximum DA from 100% to 87.51% and 88.71%, respectively. These drops in DA were considered acceptable given the average FAR improvement of 15 times and 45 times better for the CA-CFAR SA and CHAAR Upright methods, respectively. While this might not satisfy every system requirement the study found that the smaller trade off in DA is significantly off-set by the large difference in FAR. Objectively, the MCC value confirms this assessment as both CHAAR and the CA-CFAR SA methods have higher MCC values than the other methods tested. Finally, the novel methods' performances were the least sensitive to parameter adjusts shown in the ROC curve.

7.5.1 Additional Considerations

7.5.1.1 Current ship detection methods limitations

CFAR variants may perform adequately on single images with specific parameters but general performance is lacking, as is shown in the ROC curves for these methods in Figure 7.3.

Methods such as the original HAAR-like classifiers' performance is hindered as they it sees too many windows by using a sliding window technique. This means the number of detects necessary ($\mathcal{V} > 1$) needs to be increased whic sets a hard threshold on the number of ships that pass through all $\mathcal{L}$ stages. In many cases these ships are incorrectly identified as false alarms thereby lowering the DA significantly. The original HAAR-like methods were tested against smaller imagery and were not built to balance ship positives and false positive removal on images thousands of times larger and with a highly skewed class distribution. The original methods also perform contrast stretching as discussed in section 5.5.3.4 and this does not align well with the high dynamic range present in radiometrically calibrated SAR imagery.

Finally, the other methods have reduced performance because of the focus on maintaining high detection accuracies. While necessary for specific contexts in general the increase of false alarms leads to worse detectors. The SVM classifies samples by hand-picked features which do not necessarily translate to both good DA and FAR. The Modified Otsu's method relied on a global thresholding approach which significantly increases the number of false alarms, particularly along subswath lines in Sentinel-1 imagery. The discrimination based upon ship feature size is largely dependent upon the expected ship sizes but beyond that no further intelligent identification of false alarms is created. The H-dome method applies a CFAR-like local-based thresholding approach but mostly relies on the relative brightness to isolate false alarms which is why its performance is not significantly better than simpler CA-CFAR methods across a range of images. In fact, this method would be better suited as in initial thresholding method rather than a full ship detection method.

7.5.1.2 CA-CFAR Non-flat advantages

The CA-CFAR NF method provides similar performance as a low threshold CA-CFAR but does so with fewer false alarms. This indicates the introduced per-pixel thresholding extension to CA-CFAR is a reasonable improvement over other CA-CFAR methods if an good selection is made for the threshold manifold across the image. This is confirmed in Figure 7.3 where it can be seen that the CA-CFAR NF has a higher AUC than any of the CFAR methods due to its corner value being higher than those methods. The method excels in one regard because it is a simple extension to the well known and widely used CA-CFAR method. This extension can be applied to almost any CFAR variant, especially if the fixed threshold approach is used. If the fixed preselected required P_{fa} is specified (i.e. clutter distribution characterization during each step of the processing) then this method just changes that single specified P_{fa} to a P_{fa} that varies on a per-pixel basis. While not examined here, this does lend to the possibility of using more advanced non-flat manifolds to decrease the threshold and increase it exponentially along the swath width whereas the CA-CFAR NF method tested here is a linearly increasing threshold from T_C^{min} to T_C^{max}).

7.5.1.3 Simulated Annealing Manifold Adaptation advantages

The CA-CFAR SA method has the benefit that it works based on factor external to the SAR image (relies on transponder data) so that more information before detections seem to improve the end result (improvement compared to previous results on the ASAR imagery in the journal paper [3]. This method shows excellent performance because it does not require training in the traditional sense and its performance is partially dependent on the AIS dataset which independent of the SAR imagery. SA is an exhaustive search strategy so could likely improve as the quality and quantity of the transponder data gets better. The original paper published with ASAR data and the current results on RADARSAT-2/Sentinel-1 imagery show a performance improvement of about 5% for DA and FAR which due to increased the amount of data and and changes in processing of the LRIT and AIS data using hard/soft AIS ship matching.

7.5.1.4 CA-CFAR Haar-like cascade classifier advantages

The CHAAR method performs well due to a number of factors. The first is that it leverages the well-established SAR prescreening method CA-CFAR and the significant false alarm rate removal of HAAR methods. The AdaBoost training method used selects samples and features that are important at the same time as it builds and intelligently orders the cascade which allows the method to retain good samples further down the cascade and quickly discard easy-to-discriminate samples earlier on. AdaBoos also affords the ability to avoid other feature reduction techniques and does so without the same computational requirements of other methods. Furthermore, not requiring a minimum number of detects (i.e. fixed $\mathcal{V} = 1$) means the CHAAR methods have one fewer parameter that significantly affects their performance and should allow it to be more adaptive such that $\mathcal{V}$ need not be varied for different image conditions as is the case of the original HAAR methods. This along with the flexibility afforded by machine learning methods by retraining on new samples means the method is both flexible and likely more future proof than most of the other methods.

The CHAAR methods are slower to train but offer much better operational performance (see Table 7.4). This is because it leverages an optimized CA-CFAR method plus rapid feature extraction which can take approximately 200 operations per sample, many times faster than either CA-CFAR SA, HAAR or SVM methods. This is further improved if using the Upright only features set as the integral image feature extraction only needs to be performed for the Upright features.

Finally, the redundancy tests show that approximately 60% of the current dataset is necessary to correctly train the system to achieve the performances listed here for the CHAAR methods. This means that with each image having, on average, 35 ships in it we would require approximately 27 SAR images to train the method (or just under 1000 ships). Fewer than this limit and the method is not guaranteed to have the same performance. Contrastingly, the method only requires this many images and datasets larger than that (or operational systems) should at least maintain the average performance

Table 7.4. The average and worst training and operational run times in seconds for three of the methods tested.

Method	Training Runtime (average) (s)	Training Runtime (worst) (s)	Operational Runtime (average) (s)	Operational Runtime (worst) (s)
CA-CFAR SA	20	60	5000	100000
CHAAR Upright	1800	3600	1	180
SVM	900	1800	5	180

listed here for many more images assuming this dataset is a representative sample of the expected population of SAR imagery.

7.5.1.5 CA-CFAR Non-flat Disadvantages

The CA-CFAR NF method fails in some regard because it indiscriminately accepts and rejects false alarms based only on the current value, local clutter value and local threshold. This is a similar reasoning to why GO-/CA-CFAR methods cannot be the only discrimination step. Furthermore, to apply the CA-CFAR NF extension to other CFAR implementations they need to respect a per-pixel thresholding scheme and as such most implementations need to be adjusted slightly to make use of the variable fixed threshold which may not be a desirable property.

7.5.1.6 Simulated Annealing Manifold Adaptation disadvantages

The two largest downside of using the CA-CFAR SA approach is its reliance on the density of the ship positional (AIS/LRIT) data and its testing or operational runtime performance. Without the AIS and LRIT data the method devolves into an overly complicated CA-CFAR NF method with a random manifold for per-pixel thresholds which may or may not perform adequately. When examining Figures 7.4, 7.5 and 7.6 the amount of testing data is changing the amount of positional data used during operation. The method performs well up to about 70% AIS then rapid declines as the positional data decreases. This affects the sparsity of the ship in the ship distribution map which means more ships are not typical shipping lanes and thus their influence on each step of the SA becomes less which compounds at at every step.

Fewer than 1000 steps produces a CA-CFAR SA ship detector akin to a random detector so the number of steps has a strong effect on the ship detection method. Conversely, many steps are required to improve ship detection accuracy and this comes with a significant increase in operational runtime (see Table 7.4). In practice these large operational run times lead to scenarios which took hours to process a single SAR image and this process is repeated if a single SAR acquisition has multiple polarizations (Sentinel-1).

As the SA adapts the manifold it accepts the next generated manifold based on either an improvement in performance or having a value above the Boltzmann probability. By applying the Boltzmann principle to the method it allows the system to accept solutions that are not necessary optimal using at the current step which can lead to more optimal solutions at further steps. This manifests as an attempt to reset out of local minima. One issue with this, however, is that if the accepted solution is found to be severely lacking in performance many steps later then the current method has no way of resetting back a previously accepted solution. One alternative could be to store a list of accepted solutions and revert to those when the results do not improve well over a number of rounds. This, however, would increase the computational cost of the method further still which may be an undesirable solution.

7.5.1.7 CA-CFAR Haar-like cascade classifier disadvantages

Despite all of the advantages the CHAAR method presents it does come with a few disadvantages. The goal of the CHAAR method is to improve its training performance with the hope that this generalizes well to the testing data. Given a long enough training time it could perfectly discriminate the entire testing dataset but would do so at severe ovefitting that might not be visible even using variance-bias trade-off techniques such as k-fold cross validation to reduce ovefitting. Stated otherwise, theoretically it could learn to perfectly classify all samples in the training dataset with a long enough cascade but at the expense of reducing the generalization performance by assuming the dataset is a perfect representation of the real world data (obviously it is not). Furthermore, it requires a precise setup for training (fixed input image sizes, a large amount of both positive and negative samples which also applies to the HAAR method). This is a method between traditional features which are directly engineered by users (such as the ship rotation, size, etc used by the SVM method tested) and a machine generated feature set as is seen in Deep Learning [88]. The full feature set is overcomplete which means blindly using the full CHAAR could result in degraded performance. That many features are can be difficult to automatically using other techniques such as PCA. This is because the uprights feature of length $N = 111160$ require hundreds of gigabytes of memory to fit in, for instance, and SVD-PCA and currently there is a large reliance on the AdaBoost training procedure for the method to work.

7.5.1.8 Cascade complexity and necessity of rotated features.

The length of cascades $\mathcal{L}$ was varied to obtain the ROC curves for the HAAR Upright, HAAR Full, CHAAR Upright and CHAAR Full methods in Figure 7.3. The best performing cascade configurations had five strong learners $\mathcal{L} = 5$ with the number of weak learners per stage $l = 1, \ldots, 5$ was $S_l = \{1,3,1,2,94\}$ and $S_l = \{1,5,3,8,45\}$ for the HAAR and CHAAR, full and upright-only configurations, respectively. Note how the first stages of both cascade configurations have a single weak learner in the first step. This helps improve computational complexity by discarding the vast majority of false alarms early on in the cascade thereby reducing the number of overall steps required to classify an image. Using approximately half the number of weak learners in the final stage (45 vs 94) the upright-only configurations were able to outperform the full Haar-like feature cascade configurations for both the HAAR and CHAAR methods. This is likely due to the feature space of the full Haar-like feature set being 39.49% greater than that of the upright-only feature set which indicates a search space to locate salient features during AdaBoost training. This increase in feature space seems to improve the training performance hence the more complicated last stage of the configurations but this training performance does not perform as well on testing data. This implies some overfitting inherent to the full Haar-like feature set that does not occur with the upright-only feature set and is also likely the reason why performance decreases for cascades where $\mathcal{L} > 5$.

The second HAAR method [129] proposes using the same framework for object detection as the original HAAR method [128] but supplements the upright features with an the extended set of Haar-like features including rotated features. These features are proposed in order to better describe faces using Haar-like features and the original paper authors note an improvement in performance in their tests for these objects. The results here have shown that applying these original methods as-is produces sub-optimal results for ship detection in medium resolution SAR imagery. The results seem to indicate that not only are these rotated features not necessary their inclusion into the cascade classifier doubles the complexity of the stages with decreased accuracy. Even with the CA-CFAR prescreening step the number of operations for ship detection using a cascade classifier can be reduced by half by heeding this finding. In combination with the CA-CFAR the number of total operations to detect ships is significantly reduced compared to other methods. It should be noted that this is a novel aspect of applying the newly method to SAR imagery for ship detection.

7.5.1.9 Performance contextualization

The 5-7% performance decrease in DA for the proposed ship detection methods translates to roughly 5 missed ships per image on average but at the cost of significantly improved FAR. It is important to note the specific operational application of each method and whether that is an acceptable trade-off or not. For example a typical usage scenarios where the reduced number of false alarms is especially important is a tactical interception scenario. Let us take the differences between an SVM ship detection based system and a CHAAR Upright method as shown in Figure 7.7 as an example. The SVM system would identify one more ship than the CHAAR Upright method but at the cost of more than seven times the number of false alarms. If an interception team were to be sent out for every true and false positie, the total cost for the interception campaign would be much higher for the SVM-based system. The SVM-based ship detection system would send the interception team to 37 different incorrect ship locations versus the CHAAR Upright system which would only send the interception team to 5. This is an important consideration when selecting which method is preferred overall.

The methods were tested across various polarizations but the final performance did not significantly differ depending on polarization. The largest effect different polarizations had was the number of ships presented to the system. The cross-polarization imagery of Sentinel-1 typically had 5-10 more ships per image on average than the co-polarized versions. The percentage differences in DA, FAR and MCC between the imagery was minimal, however. The difference between a pixel with resolution of 25 m and 40 m made little difference in performance, especially for methods trained agnostically across the dataset (i.e. HAAR/CHAAR variants).

Most of the methods incurred errors due to three main sources: a) errors near the nadir; b) errors near land and/or caused by bright objects on land; and c) errors near bright ships which create their own copies which are misclassified as ships. The errors near the nadir were largely reduced by increasing thresholds such as that of CA-CFAR NF or by using the more advanced methods which discriminate on other features such as CHAAR. Errors near the nadir occur because the brightness values there are much higher due to the increase number of returns at the nadir position. Errors due to the effects of b) can be reduced by using repeat pass/multi acquisitions, as discussed before, or by using domain knowledge (ie operator in the loop). Most of these errors were removed by using a buffer on the land shape file but errors where bright copies of land objects were made in the range direction were filtered out by size and relative brightness. The final error of ship copies are the hardest to remove and requires a combination of "macro" views of the ship check along ships intersections if there are very similar doubles, by using classifiers specifically built to identify and finally by estimating likely copy positions using the PRF inherent in the SAR imagery metadata.

7.6 CONCLUSION

This chapter described the performance of 13 methods tested across the dataset detailed in the previous chapter, including the novel methods presented in Chapter 5. This chapter detailed the performance metrics used, including the MCC which helps to interpret the two competing performance metrics of DA and FAR. The methods were tested with their best performing parameters, variations in the most influential parameters, variations in the amount of training/testing data and finally on a single image for real-world implication testing. The two proposed methods, namely the CHAAR Upright and CA-CFAR SA, had the best and second best performances of all the methods tested across the general metrics MCC and AUC with acceptable DA performances which were compensated for by significantly improved FAR versus the other methods.

The CA-CFAR NF method achieves high DA with reduced FAR compared to the common CA-CFAR methods yet is low complexity extension to these methods and can be readily applied to many current implementations of CFAR. Given enough ship distribution information, the CA-CFAR SA method provides significant FAR reductions with acceptable DAs but does so at a high operational computational cose. The CHAAR Upright method builds upon the CA-CFAR method by including a Haar-like cascade classifier to produce results that are a balanced trade-off between a small loss of DA, a large improvement to FAR and a significantly better operational computational cost system. Furthermore, it was shown that the full set of Haar-like features are not necessary to create a high performance ship detection system and their inclusion reduces the speed and efficacy of the proposed methods.

The chapter contextualized the performance and showed that a reduction of two orders of magnitude FAR results in hundreds of fewer ships in the final output. Finally, the chapter described some of the advantages and disadvantages of the methods presented as well as how and where most of the errors in the results occurred.

CHAPTER 8 CONCLUSION

8.1 STUDY OVERVIEW

Surveillance of a country's EEZ forms an integral part of MDA. The EEZ represents a major source of income and protecting it from illegal activities is necessary to prevent other countries from exploiting their EEZ. Traditionally, the EEZ has been monitored using transponder-based systems which rely on compliance of the ship's operators. If the transponders on-board are intentionally or unintentionally disabled then tracking these ships becomes a difficult task. Furthermore, certain types of transponder systems have a limited tranmission range significantly smaller than the extent of the EEZ which means many of these transponder systems need to be supplemented with other monitoring methods to successfully track ships.

To this end remote sensing from airborne and spaceborne platforms have been used to supplement traditional transponder-based systems. Satellites equipped with EM sensors periodically observe areas to provide monitoring coverage. Of the various remote sensing techniques available, SAR has arisen as an excellent source of monitioring oceans due to its ability to penetrate cloud cover as an active sensor regardless of time of day. Another motivation is the highly spectral reflectance of the ships to the SAR operating wavelengths when compared to the diffuse reflection of water. A large amount of research has gone into improving ship detection in SAR imagery. The focus has recently been on higher resolution SAR imagery. Since the release of free lower resolution free SAR imagery from ESA's Sentinel-1/Copernicus initiative new focus has been on developing methods for this data. This can be seen as a bid to aid higher resolution SAR ship detection work by providing a wide area coverage and allowing the specification of detection reports which can direct high resolution tasking efforts. For this study, the free freely available SAR data was combined with other SAR data to create a 46 SAR image dataset that spanned across two sensors, three resolutions and four polarizations.

The thesis detailed SAR theory, some of its applications and the various benefits and expected errors that are associated with ship detection in SAR imagery. Furthermore, it was shown that results and how they are interpreted in SAR ship detection can vary significantly and as such comparing different methods across studies (without a single widely accessible dataset) becomes a complex task. In a perfect detection scenario the ship detection systems would have perfect DA with a zero FAR. In practise, a trade off between DA and FAR which leverage the number of false identified ships versus the number of correctly identified ships is necessary. In some applications it is imperative that all ships are identified whereas other applications require that the number of possible targets are reduced. However, for the general case objectively balancing DA and FAR becomes a difficult concept and this thesis highlighted a well-known machine learning confusion metric known as the MCC value to help alleviate this problem.

In this thesis two different ship discrimination methods to the SAR ship detection community were proposed. The first, “Manifold adaptation for Constant False Alarm Rate ship detection” makes use of pre-existing transponder data in combination with an extension to the conventional CA-CFAR method and Simulated Annealing. This method allows for per-pixel thresholding variations and makes use of auxiliary transponder data to help guide the creation of threshold manifolds which are used to threshold the input SAR image. This iterative procedure of threshold manifold generation does come at a significantly increased computational burden. Despite this, the method can effectively discriminate ships from false alarms with a mean DA of 87.51%, FAR of 5.644×10^{-8} and MCC value of 0.80. A second method based on machine learning techniques known as the “Haar-like feature cascade classifiers for ship discrimination” was also introduced. This method combined a low-threshold simple CA-CFAR prescreening step with an advanced cascade classifier trained on the SAR dataset. The method uses rapid integral calculations to extract features and then an carefully ordered cascade classifier discriminates between ships and false alarms. The features are scale, rotation and translation invariant and can be rapidly calculated even for the approximately 100 000 features per sub-image. The method improved upon the originals by specializations such as avoiding contrast stretching and sliding window voting techniques. The method performed best of all the methods tested with a mean DA of 88.71, FAR of 1.940×10^{-8} and MCC of 0.89 but had a strong reliance on the AdaBoost training process and the amount of training presented to it. Both of these methods were compared against 11 other methods across a range of tests including k-fold cross validation, ROC curve and AUC evaluation, variable amount of testing data to evaluate redundancy and single image analysis.

8.2 RESEARCH OBJECTIVES AND ANSWERS

At the onset of the study a few key research questions were identified. These are addressed as follows:

1. What current ship detection method can be improved to increase overall ship detection in medium resolution SAR imagery? Three main contributions were made in this thesis. The first was that additional data was used during the detection stage. A novel method which makes use of historic transponder data was proposed. The method extends on the conventional CA-CFAR prescreening step to allow for more varied threshold specifications on a per-pixel basis. The second was improvement of existing methods that operate on medium resolution imagery. Most SAR ship detection research focuses on higher resolution data because of the similarity between ships and SAR artifacts in medium resolution image which can be mitigated when using many more pixels to describe ships in high resolution SAR imagery. Methods specifically tailored to work on these higher resolutions were often directly applied to work on lower resolution imagery. As such this thesis addressed this problem by introducing two methods that helped to build upon previous lower resolution method to deal with the smaller ships present in current SAR imagery and make use of machine learning techniques. The third contribution was the creation of an dataset which could help to provide objective evaluations across SAR ship detection studies.

2. Can operational ship detection be accomplished by utilizing machine learning and related methods? Across the various tests performed in this thesis it was proved that by utilizing various machine learning methods state-of-the-art ship detection methods could be created that balanced training time with excellent computational and detection performance. Specifically, by leveraging the usefulness of the simple CA-CFAR method and template feature extraction and training the CA-CFAR-based Haar-like cascade classifier was shown to be the best performing method across a number of metrics and scenarios.

3. Are the current performance metrics used for ship detection results sufficient to underline performance differences between methods in a meaningful manner across different datasets? The thesis demonstrated that while sufficient to describe the performance of the system the typical metrics of DA and FAR vary widely in their interpretation across studies. Where some studies

would completely disregard ships without transponder data, others would highlight detection accuracies without detailing false alarm rates, especially across multiple images. Furthermore, as mentioned above, balancing DA and FAR becomes difficult for the general case and the thesis introduced the MCC metric to the SAR ship detection community to help objectively select what trade-offs between the two are acceptable. Due to the fact that the MCC takes all the confusion matrix factors into account it can be used to identify methods which perform well in the general case and was specifically designed for heavily skewed class distributions, as is the case with SAR ship detection.

8.3 CONTRIBUTIONS

The following publications have emanated from this study:

- Journal Articles:
    - C. P. Schwegmann, W. Kleynhans, and B. P. Salmon, “Manifold Adaptation for Constant False Alarm Rate Ship Detection in South African Oceans,” IEEE Journal of Selected Topics in Applied Earth Observations and Remote Sensing, vol. 8, no. 7, pp. 3329 - 3337, July 2015.
    - C. P. Schwegmann, W. Kleynhans, and B. P. Salmon, “Synthetic Aperture radar Ship Detection Using Haar-Like Features,” IEEE Geoscience and Remote Sensing Letters, vol. 14, no. 2, pp. 154 - 158, Feb. 2017.
- Main Author International Conference Papers:
    - C. P. Schwegmann and W. Kleynhans, “Synthetic aperture radar for maritime domain awareness: Ship detection in a South African context,” in African Association of Remote Sensing of the Environment (AARSE), Oct. 2014, pp. 257 - 265.
    - C. P. Schwegmann, W. Kleynhans, and B. P. Salmon, “Simulated Annealing CFAR Threshold Selection for South African Ship Detection in ASAR imagery,” in IEEE Inter-

national Geoscience and Remote Sensing Symposium (IGARSS), July 2014, pp. 561 - 564.

  - C. P. Schwegmann, W. Kleynhans, and B. P. Salmon, “Ship Detection in South African oceans using SAR, CFAR and a Haar-like Feature Classifier,” in IEEE International Geoscience and Remote Sensing Symposium (IGARSS), July 2014, pp. 557 - 560.

  - C. P. Schwegmann, W. Kleynhans, B. P. Salmon, and L. Mdakane, “Ship detection in Sentinel-1 imagery using the H-dome transformation,” in IEEE International Geoscience and Remote Sensing Symposium (IGARSS), July 2015, pp. 3710 - 3714.

  - C. P. Schwegmann, W. Kleynhans, B. P. Salmon, and L. Mdakane, “A CA-CFAR and localized wavelet ship detector for Sentinel-1 imagery,” in IEEE International Geoscience and Remote Sensing Symposium (IGARSS), July 2015, pp. 3707 - 3710.

  - C. P. Schwegmann, W. Kleynhans, B. P. Salmon, L. W.Mdakane, and R. G. V. Meyer, “Very deep learning for ship discrimination in Synthetic Aperture radar imagery,” in IEEE International Geoscience and Remote Sensing Symposium (IGARSS), July 2016, pp. 104 - 107.

  - C. P. Schwegmann, W. Kleynhans, B. P. Salmon, L. W.Mdakane, and R. G. V. Meyer, “Ships as salient objects in Synthetic Aperture radar imagery,” in IEEE International Geoscience and Remote Sensing Symposium (IGARSS), July 2016, pp. 6898 - 6901.

- Co-Author International Conference Papers:

  - W. Kleynhans, B. P. Salmon, C. P. Schwegmann and V. Seotlo, “Ship Detection in South African oceans using a combination of SAR and historic LRIT data,” in IEEE International Geoscience and Remote Sensing Symposium (IGARSS), July 2013, pp. 1521 - 1524.
  - B. P. Salmon, W. Kleynhans, C. P. Schwegmann, and J. C. Olivier, “Proper comparision among methods using a Confusion Matrix,” in IEEE International Geoscience and Remote Sensing Symposium (IGARSS), July 2015, pp. 3057 - 3060.

- W. Kleynhans, B. P. Salmon, C. P. Schwegmann, and L. Mdakane, "Use of Sentinel-1 data for vessel detection in South African oceans: Early results," in IEEE radar Conference, Oct. 2015, pp. 431 - 434.

In addition to the above, the results of this research has directly fed into a SAR ship detection platform currently being developed at the Council for Science and Industrial Research related to the "Oceans and Coasts Vessel Tracking Tool".

8.4 FUTURE WORK

The CHAAR method represents a combination of classical machine learning by selecting a fixed set of features but also sides with the more modern approach of letting the training of the system determine which of the overcomplete feature set is necessary to correctly discriminate ships. The machine learning community has recently been inundated with research into the newest machine learning technique known as deep learning. Instead of manually selecting features, these new machine learning techniques create their own features unlikely to be created using classical feature engineering methods. This places the onus of selecting salient features on the network and leaves the architecture composition up to the researcher. While posting initial high performance results Deep Learning methods need to be thoroughly investigated to determine if these new techniques are able to successfully discriminate ships in a wide variety of SAR imagery. Furthermore, additional avenues for Deep Learning research include high quality ship classification as the classification of optical imagery was the primary driver behind the development of Deep Learning.

8.5 CLOSING

This thesis detailed two novel methods that showed improved performance when compared to current state-of-the-art methods across a number of metrics. Each of these methods have their own advantages and disadvantages and their usage and designed goals might not necessarily align with all specifications for all systems. This means care needs to be taken before blindly selecting either as the final stage in the an MDA system.

REFERENCES

[1] G. Galdorisi and R. Goshorn, “Bridging the Policy and Technology Gap: A Process to Instantiate Maritime Domain Awareness,” in *Proceedings of MTS/IEEE OCEANS 2005*, Sep. 2005, pp. 1–8.

[2] P. M. Mather, *Computer Processing of Remotely-Sensed Images: An Introduction*, 3rd ed. New York, NY: John Wiley and Sons, 2004.

[3] C. Schwegmann, W. Kleynhans, and B. P. Salmon, “Manifold Adaptation for Constant False Alarm Rate Ship Detection in South African Oceans,” *IEEE Journal of Selected Topics in Applied Earth Observations and Remote Sensing*, vol. 8, no. 7, pp. 3329–3337, Jul. 2015.

[4] C. Schwegmann, W. Kleynhans, and B. Salmon, “Synthetic Aperture Radar Ship Detection Using Haar-Like Features,” *IEEE Geoscience and Remote Sensing Letters*, vol. 14, no. 2, pp. 154–158, Feb. 2017.

[5] C. P. Schwegmann, W. Kleynhans, B. P. Salmon, L. W. Mdakane, and R. G. V. Meyer, “Ships as salient objects in Synthetic Aperture Radar imagery,” in *IEEE International Geoscience and Remote Sensing Symposium (IGARSS)*, Jul. 2016, pp. 6898–6901.

[6] C. P. Schwegmann, W. Kleynhans, B. P. Salmon, and L. Mdakane, “Ship detection in Sentinel-1 imagery using the H-dome transformation,” in *IEEE International Geoscience and Remote Sensing Symposium (IGARSS)*, Jul. 2015, pp. 3710–3714.

[7] ——, “A CA-CFAR and localized wavelet ship detector for Sentinel-1 imagery,” in *IEEE International Geoscience and Remote Sensing Symposium (IGARSS)*, Jul. 2015, pp. 3707–3710.

[8] National Security Affairs, “Maritime Security Policy,” National Security Affairs, Washington, DC, Tech. Rep. NSPD-41/HSPD-13, Dec. 2004.

[9] Bruce Mitchell (eds.), *Resource and Environmental Management in Canada: Addressing Conflict and Uncertainty*, 1st ed. Don Mills, Ontario: Oxford University Press, 2004.

[10] D. J. Agnew *et al.*, “Estimating the Worldwide Extent of Illegal Fishing,” *Public Library of Science ONE*, vol. 4, no. 2, pp. 1–8, Feb. 2009.

[11] S. Moolla, “Contextualising Illegal, Unregulated and Unreported fishing of Marine Resources in South African Waters,” Institute for Security Studies South Africa, New Muckleneuk, Pretoria, Tech. Rep. N/A, Jan. 2009.

[12] E. Shahbazian and G. Rogova, *Human Systems Integration to Enhance Maritime Domain Awareness for Port/Harbour Security*, 1st ed. Amsterdam, Netherlands: IOS Press, 2010.

[13] P. C. Office, “Securing an Open Society: Canada’s National Security Policy,” Canadian Government, Ottawa, Canada, Tech. Rep. CP22-77/2004E-PDF, Apr. 2004.

[14] N. Wegge, “Small state, maritime great power? Norway’s strategies for influencing the maritime policy of the European Union,” *Marine Policy*, vol. 35, no. 3, pp. 335–342, May 2011.

[15] South African Navy, “Maritime Doctrine for the SA Navy,” South African Navy, Department: Defence, Cape Town, South Africa, Tech. Rep. SANGP 100, Oct. 2006.

[16] South African Government. (2012) Oceans Economy. [Online]. Available: http://www.gov.za/sites/www.gov.za/files/images/oceans-economy-leaflet.pdf

[17] W. Kleynhans, B. P. Salmon, C. P. Schwegmann, and V. Seotlo, “Ship Detection in South African oceans using a combination of SAR and historic LRIT data,” in *IEEE International*

Geoscience and Remote Sensing Symposium (IGARSS), Jul. 2013, pp. 1521–1524.

[18] D. J. Crisp, “The State-of-the-Art in Ship Detection in Synthetic Aperture Radar Imagery,” DSTO Information Sciences Laboratory, Edinburgh, South Australia, Tech. Rep. DSTO-RR-0272, May 2004.

[19] P. Silveira, A. Teixeira, and C. G. Soares, “Use of AIS Data to Characterise Marine Traffic Patterns and Ship Collision Risk off the Coast of Portugal,” *Journal of Navigation*, vol. 66, no. 6, pp. 879–898, Nov. 2013.

[20] International Maritime Organization, *Electronic SOLAS Consolidated Edition*, 1st ed. Reading, MA: International Maritime Organization, 2014.

[21] J. T. Watson and A. C. Haynie, “Using Vessel Monitoring System Data to Identify and Characterize Trips Made by Fishing Vessels in the United States North Pacific,” *Public Library of Science ONE*, vol. 11, no. 10, pp. 1–20, Oct. 2016.

[22] S. Jennings and J. Lee, “Defining fishing grounds with vessel monitoring system data,” *ICES Journal of Marine Science: Journal du Conseil*, vol. 69, no. 1, pp. 51–63, Jan. 2012.

[23] G. Høye, T. Eriksen, B. J. Meland, and B. Narheim, “Space-based AIS for global maritime traffic monitoring,” *Acta Astronautica*, vol. 62, no. 2, pp. 240–245, Jan. 2008.

[24] T. Eriksen, G. Høye, B. Narheim, and B. J. Meland, “Maritime traffic monitoring using a space-based AIS receiver,” *Acta Astronautica*, vol. 58, no. 10, pp. 537–549, May 2006.

[25] H. Heiselberg, “A Direct and Fast Methodology for Ship Recognition in Sentinel-2 Multispectral Imagery,” *Remote Sensing*, vol. 8, no. 12, pp. 1–11, Dec. 2016.

[26] F. Katsilieris, P. Braca, and S. Coraluppi, “Detection of malicious AIS position spoofing by exploiting radar information,” in *International Conference on Information Fusion (FUSION)*, Jul. 2013, pp. 1196–1203.

[27] W. Kleynhans, B. P. Salmon, C. P. Schwegmann, and L. Mdakane, "Use of Sentinel-1 data for vessel detection in South African oceans: Early results," in *IEEE Radar Conference*, Oct. 2015, pp. 431–434.

[28] A. Pearce and C. Pattiaratchi, "Applications of satellite remote sensing to the marine environment in Western Australia," *Journal of the Royal Society of Western Australia*, vol. 80, no. 1, pp. 1–14, Mar. 1997.

[29] W. Kleynhans, J. C. Olivier, K. J. Wessels, B. P. Salmon, F. van den Bergh, and K. Steenkamp, "Detecting Land Cover Change Using an Extended Kalman Filter on MODIS NDVI Time-Series Data," *IEEE Geoscience and Remote Sensing Letters*, vol. 8, no. 3, pp. 507–511, May 2014.

[30] L. Naidoo, R. Mathieu, R. Main, W. Kleynhans, K. Wessels, G. P. Asner, and B. Leblon, "The assessment of data mining algorithms for modelling Savannah Woody cover using multi-frequency (X-, C- and L-band) synthetic aperture radar (SAR) datasets," in *IEEE International Geoscience and Remote Sensing Symposium (IGARSS)*, Jul. 2014, pp. 1049–1052.

[31] C. P. Schwegmann, W. Kleynhans, and B. P. Salmon, "Simulated Annealing CFAR Threshold Selection for South African Ship Detection in ASAR imagery," in *IEEE International Geoscience and Remote Sensing Symposium (IGARSS)*, Jul. 2014, pp. 561–564.

[32] J. C. Landy, D. Isleifson, A. S. Komarov, and D. G. Barber, "Parameterization of Centimeter-Scale Sea Ice Surface Roughness Using Terrestrial LiDAR," *IEEE Transactions on Geoscience and Remote Sensing*, vol. 53, no. 3, pp. 1271–1286, Mar. 2015.

[33] C. Oliver and S. Quegan, *Understanding Synthetic Aperture Radar Images*, 1st ed. Rayleigh, NC: SciTech Publishing, 2004.

[34] J. Barnum, "Ship detection with high-resolution HF skywave radar," *IEEE Journal of Oceanic Engineering*, vol. 11, no. 2, pp. 196–209, Apr. 1986.

[35] C. K. Liang, S. Mills, B. I. Hauss, and S. D. Miller, "Improved VIIRS Day/Night Band Imagery With Near-Constant Contrast," *IEEE Transactions on Geoscience and Remote Sensing*, vol. 52,

no. 11, pp. 6964–6971, Nov. 2014.

[36] M. L. Imhoff, P. Johnson, W. Holford, J. Hyer, L. May, W. Lawrence, and P. Harcombe, "BioSARTM: an inexpensive airborne VHF multiband SAR system for vegetation biomass measurement," *IEEE Transactions on Geoscience and Remote Sensing*, vol. 38, no. 3, pp. 1458–1462, May 2000.

[37] J. V. Zyl and Y. Kim, *Synthetic Aperture Radar Polarimetry*, 1st ed. New York, NY: John Wiley and Sons, 2011.

[38] K. Ouchi, "Recent Trend and Advance of Synthetic Aperture Radar with Selected Topics," *Remote Sensing*, vol. 5, no. 2, pp. 716–807, Feb. 2013.

[39] A. Hein, *Processing of SAR Data: Fundamentals, Signal Processing, Interferometry*, 1st ed. Berlin, Germany: Springer, 2004.

[40] H. Akliouat, Y. Smara, and L. Bouchemakh, "Synthetic aperture radar image formation process: application to a region of North Algeria," in *ESA ENVISAT Symposium*, Jul. 2007, pp. 23–27.

[41] J. Marquez-Martinez, J. Mittermayer, and M. Rodriguez-Cassola, "Radiometric resolution optimization for future SAR systems," in *IEEE International Geoscience and Remote Sensing Symposium (IGARSS)*, Sep. 2004, pp. 1738–1741.

[42] M. D. Graziano, M. D'Errico, and E. Razzano, "Constellation analysis of an integrated AIS/remote sensing spaceborne system for ship detection," *Advances in Space Research*, vol. 50, no. 3, pp. 351–362, Aug. 2012.

[43] S. Rane, P. Boufounos, A. Vetro, and Y. Okada, "Low complexity efficient raw SAR data compression," in *SPIE Algorithms for Synthetic Aperture Radar Imagery*, Apr. 2011, pp. 80 510W–80 510W–11.

[44] H. Maitre (eds.), *Processing of Synthetic Aperture Radar Images*, 1st ed. New York, NY: John Wiley and Sons, 2008.

[45] K. Tempfli, N. Kerle, G. C. Huurneman, and L. L. F. Janssen, *Principles of Remote Sensing An introductory textbook*, 1st ed. Enschede, The Netherlands: The International Institute for Geo-Information Science and Earth Observation (ITC), 2009.

[46] L. Gagnon and A. Jouan, “Speckle filtering of SAR images: a comparative study between complex-wavelet-based and standard filters,” *Proceedings of SPIE*, vol. 3169, no. 1, pp. 80–91, Oct. 1997.

[47] M. R. de Leeuw, “Performance evaluation of sevarl adaptive speckle filters for SAR imaging,” in *Anais XIV Simposio Brasileiro de Sensoriamento Remoto*, Jul. 2009, pp. 7299–7305.

[48] X. Zhou, N. Chang, and S. Li, “Applications of SAR Interferometry in Earth and Environmental Science Research,” *Sensors*, vol. 9, no. 3, pp. 1876–1912, Mar. 2009.

[49] J. Engelbrecht and M. R. Inggs, “Detection and monitoring of surface subsidence associated with mining activities in the Witbank Coalfields, South Africa, using differential radar interferometry,” in *IEEE International Geoscience and Remote Sensing Symposium (IGARSS)*, Jul. 2011, pp. 1596–1599.

[50] D. Velotto, M. Soccorsi, and S. Lehner, “Azimuth Ambiguities Removal for Ship Detection Using Full Polarimetric X-Band SAR Data,” *IEEE Transactions on Geoscience and Remote Sensing*, vol. 52, no. 1, pp. 76–88, Jan. 2014.

[51] C. Santamaria and H. Greidanus, “Ambiguity discrimination for ship detection using Sentinel-1 repeat acquisition operations,” in *IEEE International Geoscience and Remote Sensing Symposium (IGARSS)*, Jul. 2015, pp. 2477–2480.

[52] H. Greidanus, P. Clayton, M. Indregard, G. Staples, N. Suzuki, P. Vachoir, C. Wackerman, T. Tennvassas, J. Mallorqui, N. Kourti, R. Ringrose, and H. Melief, “Benchmarking operational SAR ship detection,” in *IEEE International Geoscience and Remote Sensing Symposium (IGARSS)*, Sep. 2004, pp. 4215–4218.

[53] H. Greidanus and N. Kourti, “Findings of the DECLIMS project - Detection and Classification

of Marine Traffic from Space," in *Proceedings of SEASAR - Advances in SAR Oceanography from ENVISAT AND ERS Missions*, Jan. 2006, pp. 1–9.

[54] H. C. Stankwitz, R. J. Dallaire, and J. R. Fienup, "Nonlinear apodization for sidelobe control in SAR imagery," *IEEE Transactions on Aerospace and Electronic Systems*, vol. 31, no. 1, pp. 267–279, Jan. 1995.

[55] J. Statsny *et al.*, "A novel adaptive synthetic aperture radar ship detection system," in *Proceesinds of MTS/IEEE OCEANS*, Sep. 2011, pp. 1–7.

[56] I. I. Lin, L. K. Kwoh, Y. Lin, and V. Khoo, "Ship and ship wake detection in the ERS SAR imagery using computer-based algorithm," in *IEEE International Geoscience and Remote Sensing Symposium (IGARSS)*, Jul. 2016, pp. 6898–6901.

[57] H. Greidanus and C. Santamaria, "First Analyses of Sentinel-1 Images for Maritime Surveillance," European Commission Joint Research Centre (JRC), Brussels, Belgium, Tech. Rep. 978-92-79-44715-0, Oct. 2014.

[58] A. Marino and I. Hajnsek, "Ship Detection With TanDEM-X Data Extending the Polarimetric Notch Filter," *IEEE Geoscience and Remote Sensing Letters*, vol. 12, no. 10, pp. 2160–2164, Oct. 2015.

[59] R. K. Raney, *Principles and Applications of Remote Sensing (Manual of Remote Sensing)*, 3rd ed. New York, NY: John Wiley and Sons, 1998, ch. 2.

[60] M. Beauchemin, K. P. B. Thomson, and G. Edwards, "Optimization of the Gamma-Gamma MAP filter for SAR image clutters," *International Journal of Remote Sensing*, vol. 17, no. 5, pp. 1063–1067, Sep. 1996.

[61] European Space Agency (ESA), "Sentinel-1 Radiometric Calibration of Products," European Space Agency (ESA), Paris, France, Tech. Rep. ESA-EOPG-CSCOP-TN-0002, May 2015.

[62] Z. Liu, F. Li, N. Li, R. Wang, and H. Zhang, “A Novel Region-Merging Approach for Coastline Extraction From Sentinel-1A IW Mode SAR Imagery,” *IEEE Geoscience and Remote Sensing Letters*, vol. 13, no. 3, pp. 324–328, Mar. 2016.

[63] X. Leng, K. Ji, K. Yang, and H. Zou, “A Bilateral CFAR Algorithm for Ship Detection in SAR Images,” *IEEE Geoscience and Remote Sensing Letters*, vol. 12, no. 7, pp. 1536–1540, Jul. 2015.

[64] K. El-Darymli, P. McGuire, D. Power, and C. Moloney, “Target detection in synthetic aperture radar imagery: a state-of-the-art survey,” *Journal of Applied Remote Sensing*, vol. 7, no. 1, pp. 071 598–071 598, Mar. 2013.

[65] J. M. de Nicolas, D. Mata-Moya, M. P. Jarabo-Amores, N. del Rey-Maestre, and J. L. Barcena-Humanes, “Neural network based solutions for ship detection in SAR images,” in *International Conference on Digital Signal Processing (DSP)*, Jul. 2013, pp. 1–6.

[66] D. Stagliano, A. Lupidi, and F. Berizzi, “Ship detection from SAR images based on CFAR and wavelet transform,” in *Tyrrhenian Workshop on Advances in Radar and Remote Sensing (TyWRRS)*, Sep. 2012, pp. 53–58.

[67] F. Bi, F. Pang, B. Zhu, and L. Chen, “A cascaded false-alarm elimination method for accurate ship detection in SAR images,” in *IET International on Radar Conference*, Sep. 2013, pp. 1–4.

[68] J. R. A. Morillas, I. C. GarcÄśa, and U. Zolzer, “Ship detection based on SVM using color and texture features,” in *IEEE Intelligent Computer Communication and Processing (ICCP)*, Sep. 2015, pp. 343–350.

[69] M. Messina, M. Greco, L. Fabbrini, and G. Pinelli, “Modified Otsu’s algorithm: A new computationally efficient ship detection algorithm for SAR images,” in *Tyrrhenian Workshop on Advances in Radar and Remote Sensing (TyWRRS)*, Sep. 2012, pp. 262–266.

[70] J. Y. Ji, J. M. Zhang, and X. Zhang, “A new CFAR ship target detection method in SAR imagery,” *acta Oceanologica Sinica*, vol. 29, no. 1, pp. 12–16, Jan. 2010.

[71] R. C. Gonzalez and R. E. Woods, *Digital Image Processing*, 3rd ed. Upper Saddle River, NJ: Prentice Hall, 2008.

[72] N. Otsu, “A Threshold Selection Method from Gray-Level Histograms,” *IEEE Transactions on Systems, Man, and Cybernetics*, vol. 9, no. 1, pp. 62–66, Jan. 1979.

[73] D. Velotto, C. Bentes, B. Tings, and S. Lehner, “Comparison of Sentinel-1 and TerraSAR-X for ship detection,” in *IEEE 5th Asia-Pacific Conference on Synthetic Aperture Radar (APSAR)*, Sep. 2015, pp. 3282–3285.

[74] W. An, C. Xie, and X. Yuan, “An Improved Iterative Censoring Scheme for CFAR Ship Detection With SAR Imagery,” *IEEE Transactions on Geoscience and Remote Sensing*, vol. 52, no. 8, pp. 4585–4595, Aug. 2014.

[75] M. Stasolla, J. J. Mallorqui, G. Margarit, C. Santamaria, and N. Walker, “A Comparative Study of Operational Vessel Detectors for Maritime Surveillance Using Satellite-Borne Synthetic Aperture Radar,” *IEEE Journal of Selected Topics in Applied Earth Observations and Remote Sensing*, vol. 9, no. 6, pp. 2687–2701, Jun. 2016.

[76] M. Richards, *Fundementals of Radar Singal Processing.*, 1st ed. New York, NY: McGraw-Hill, 2005.

[77] P. Lombardo, M. Sciotti, and L. M. Kaplan, “SAR prescreening using both target and shadow information,” in *IEEE Radar Conference*, May 2001, pp. 147–152.

[78] G. Schwartz, M. Alvarez, A. Varfis, and N. Kourti, “Elimination of false positives in vessels detection and identification by remote sensing,” in *IEEE International Geoscience and Remote Sensing Symposium (IGARSS)*, Jul. 2001, pp. 116–118.

[79] P. P. Gandhi and S. A. Kassam, “Analysis of CFAR processors in homogeneous background,” *IEEE Transactions on Aerospace and Electronic Systems*, vol. 24, no. 4, pp. 427–445, Jul. 1988.

[80] P. Iervolino, R. Guida, and P. Whittaker, “A novel ship-detection technique for Sentinel-1 SAR data,” in *IEEE 5th Asia-Pacific Conference on Synthetic Aperture Radar (APSAR)*, Sep. 2015, pp. 797–801.

[81] P. P. Gandhi and S. A. Kassam, “Optimality of the cell averaging CFAR detector,” *IEEE Transactions on Information Theory*, vol. 40, no. 4, pp. 1226–1228, Jul. 1994.

[82] J. M. de Nicolas, P. Jarabo-Amores, N. del Rey-Maestre, P. G. del Hoyo, and J. L. Barcena-Humanes, “Robustness of a Generalized Gamma CFAR ship detector applied to TerraSAR-X and Sentinel-1 images,” in *IEEE International Conference on Computer as a Tool (EUROCON)*, Sep. 2015, pp. 1–6.

[83] C. Wang, M. Liao, and X. Li, “Ship detection in SAR Image Based on the Alpha-stable Distribution,” *Sensors*, vol. 8, no. 8, pp. 4948–4960, Aug. 2008.

[84] G. Gao, “A Parzen-Window-Kernel-Based CFAR Algorithm for Ship Detection in SAR Images,” *IEEE Geoscience and Remote Sensing Letters*, vol. 8, no. 3, pp. 557–561, May 2011.

[85] X. Leng, K. Ji, S. Zhou, X. Xing, and H. Zou, “An Adaptive Ship Detection Scheme for Spaceborne SAR Imagery,” *Sensors*, vol. 16, no. 9, pp. 1–22, Sep. 2016.

[86] M. Tello, C. Lopez-Martinez, and J. J. Mallorqui, “A novel algorithm for Ship Detection in SAR imagery based on the Wavelet Transform,” *IEEE Geoscience and Remote Sensing Letters*, vol. 2, no. 2, pp. 201–205, Apr. 2005.

[87] J. M. de Nicolas, D. Mata-Moya, M. P. Jarabo-Amores, N. del Rey-Maestre, and V. M. Pelaez-Sanchez, “Comparative study of ship detection techniques in TerraSAR-X images,” in *European Microwave Conference (EuMC)*, Oct. 2014, pp. 1836–1839.

[88] C. P. Schwegmann, W. Kleynhans, B. P. Salmon, L. W. Mdakane, and R. G. V. Meyer, “Very Deep Learning for Ship Discrimination in Synthetic Aperture Radar Imagery,” in *IEEE International Geoscience and Remote Sensing Symposium (IGARSS)*, Jul. 2016, pp. 104–107.

[89] S. Wang, M. Wang, S. Yang, and L. Jiao, “New Hierarchical Saliency Filtering for Fast Ship Detection in High-Resolution SAR Images,” *IEEE Transactions on Geoscience and Remote Sensing*, vol. 55, no. 1, pp. 351–362, Jan. 2017.

[90] B. Hou, X. Chen, and L. Jiao, “Multilayer CFAR Detection of Ship Targets in Very High Resolution SAR Images,” *IEEE Geoscience and Remote Sensing Letters*, vol. 12, no. 4, pp. 811–815, Apr. 2015.

[91] L. Zhai, Y. Li, and Y. Su, “Inshore Ship Detection via Saliency and Context Information in High-Resolution SAR Images,” *IEEE Geoscience and Remote Sensing Letters*, vol. 13, no. 12, pp. 1870–1874, Dec. 2016.

[92] G. Margarit, J. A. B. MilanÃľs, and A. Tabasco, “Operational Ship Monitoring System Based on Synthetic Aperture Radar Processing,” *Remote Sensing*, vol. 1, no. 3, pp. 375–392, Sep. 2009.

[93] H. Leung, N. Dubash, and N. Xie, “Detection of small objects in clutter using a GA-RBF neural network,” *IEEE Transactions on Aerospace and Electronic Systems*, vol. 38, no. 1, pp. 98–118, Jan. 2002.

[94] X. Yang, F. Bi, Y. Yu, and L. Chen, “An effective false-alarm removal method based on OC-SVM for SAR ship detection,” in *IET International Radar Conference*, Oct. 2015, pp. 1–4.

[95] X. Su, G. Yang, and H. Sang, “Ship Detection in Polarimetric SAR Based on Support Vector Machine,” *Research Journal of Applied Sciences, Engineering and Technology*, vol. 4, no. 18, pp. 3448–3454, Sep. 2012.

[96] H. Dai, L. Du, Y. Wang, and Z. Wang, “A Modified CFAR Algorithm Based on Object Proposals for Ship Target Detection in SAR Images,” *IEEE Geoscience and Remote Sensing Letters*, vol. 13, no. 12, pp. 1925–1929, Dec. 2016.

[97] L. L. Li and J. K. Wang, “SAR image ship detection based on Ant Colony Optimization,” in *International Congress on Image and Signal Processing (CISP)*, Oct. 2012, pp. 1100–1103.

[98] V. Wismann, “Radar signatures of mineral oil spills measured by an airborne multi-frequency radar and the ERS-1 SAR,” in *IEEE International Geoscience and Remote Sensing Symposium (IGARSS)*, Aug. 1993, pp. 940–942.

[99] H. Huhnerfuss *et al.*, “Classification of sea slicks by multifrequency radar techniques: New chemical insights and their geophysical implications,” *Journal of Geophysical Research*, vol. 99, no. C5, pp. 9835–9845, May 1994.

[100] G. Franceschetti *et al.*, “SAR raw signal simulation of oil slicks in ocean environment,” *IEEE Transactions on Geoscience and Remote Sensing*, vol. 40, no. 9, pp. 1935–1949, Sep. 2002.

[101] M. Migliaccio, A. Gambardella, F. Nunziata, M. Shimada, and O. Isoguchi, “The PALSAR Polarimetric Mode for Sea Oil Slick Observation,” *IEEE Transactions on Geoscience and Remote Sensing*, vol. 47, no. 12, pp. 4032–4041, Dec. 2009.

[102] M. Migliaccio, F. Nunziata, C. E. Brown, B. Holt, X. Li, W. Pitchel, and M. Shimada, “Polarimetric synthetic aperture radar utilized to track oil spills,” *Eos, Transactions American Geophysical Union*, vol. 93, no. 16, pp. 161–162, Apr. 2012.

[103] A. S. P. Pavlakis and S. Alexandry, “On the optimization of spaceborne SAR capacity in oil spill detection and the related hydrodynamic phenomena,” *Spill Science Technology Bulletin*, vol. 3, no. 1-2, pp. 33–40, Mar. 1996.

[104] W. M. Moon *et al.*, “RADARSAT-2 and Coastal Applications: Surface Wind, Waterline, and Intertidal Flat Roughness,” *Proceedings of the IEEE*, vol. 98, no. 5, pp. 800–815, May 2010.

[105] L. W. Mdakane, W. Kleynhans, and C. P. Schwegmann, “Using an active contour method to detect bilge dumps from SAR imagery,” in *IEEE International Geoscience and Remote Sensing Symposium (IGARSS)*, Jul. 2016, pp. 5015–5018.

[106] R. Pelich, N. Longepe, G. Mercier, G. Hajduch, and R. Garello, “Performance evaluation of Sentinel-1 data in SAR ship detection,” in *IEEE International Geoscience and Remote Sensing Symposium (IGARSS)*, Jul. 2015, pp. 2103–2106.

[107] A. Renga and A. Moccia, “Ship Velocity Estimation by Doppler Centroid Analysis of focused SAR Data,” in *IEEE International Geoscience and Remote Sensing Symposium (IGARSS)*, Jul. 2014, pp. 1809–1812.

[108] P. W. Vachon, J. Wolfe, and H. Greidanus, “Analysis of Sentinel-1 Marine Applications Potential,” in *IEEE International Geoscience and Remote Sensing Symposium (IGARSS)*, Jul. 2012, pp. 1734–1737.

[109] P. Potin, B. Rosich, J. Roeder, and P. Bargellini, “Sentinel-1 Mission Operations Concept,” in *IEEE International Geoscience and Remote Sensing Symposium (IGARSS)*, Jul. 2014, pp. 1465–1468.

[110] European Space Agency (ESA). (2014) Sentinel-1 Observation Scenario. [Online]. Available: https://sentinel.esa.int/web/sentinel/missions/sentinel-1/observation-scenario

[111] C. Bentes, D. Velotto, and S. Lehner, “Analysis of Ship size Detectablilty over different TerraSAR-X Modes,” in *IEEE International Geoscience and Remote Sensing Symposium (IGARSS)*, Jul. 2014, pp. 5137–5140.

[112] M. Chabot *et al.*, “RADARSAT-2 System Operations and Performance,” in *IEEE International Geoscience and Remote Sensing Symposium (IGARSS)*, Jul. 2014, pp. 994–997.

[113] R. Pelich, N. Longepe, G. Mercier, G. Hajduch, and R. Garello, “âĂIJShip Detection in SAR medium resolution imagery for Martime Surveillance: Algorithm Validation using AIS Data,” in *IEEE International Geoscience and Remote Sensing Symposium (IGARSS)*, Jul. 2014, pp. 3690–3693.

[114] ——, “Refocusing of Ship Signatures and Azimuth Speed Estimation based on FRFT and SAR SLC imagery,” in *IEEE International Geoscience and Remote Sensing Symposium (IGARSS)*, Jul. 2015, pp. 3699–3702.

[115] P. W. Vachon, C. Kabatoff, and R. Quinn, “Operational Ship Detection in Canada using RADARSAT,” in *IEEE International Geoscience and Remote Sensing Symposium (IGARSS)*,

Jul. 2014, pp. 998–1001.

[116] J. Yin and J. Yang, “Ship Detection by using the M-chi and M-delta Decompositions,” in *IEEE International Geoscience and Remote Sensing Symposium (IGARSS)*, Jul. 2014, pp. 2738–2741.

[117] S. Song and J. Yang, “Ship Detection in Polarmetric SAR images via Tensor Robust Principle Component Analysis,” in *IEEE International Geoscience and Remote Sensing Symposium (IGARSS)*, Jul. 2015, pp. 3152–3155.

[118] B. P. Salmon, W. Kleynhans, C. P. Schwegmann, and J. C. Olivier, “Proper comparision among methods using a Confusion Matrix,” in *IEEE International Geoscience and Remote Sensing Symposium (IGARSS)*, Jul. 2015, pp. 3057–3060.

[119] C. P. Schwegmann, W. Kleynhans, and B. P. Salmon, “Ship Detection in South African oceans using SAR, CFAR and a Haar-like Feature Classifier,” in *IEEE International Geoscience and Remote Sensing Symposium (IGARSS)*, Jul. 2014, pp. 557–560.

[120] S. Sivanandam and S. Deepa, *Digital Functions and Data Reconstruction Digital-Discrete Methods*, 1st ed. New York, NY: Springer, 2013.

[121] J. Flemming. (2015) Highway Networks with TensorFlow. [Online]. Available: https://medium.com/jim-fleming/highway-networks-with-tensorflow-1e6dfa667daa

[122] J. B. Tenenbaum, V. de Silva, and J. C. Langford, “A Global Geometric Framework for Nonlinear Dimensionality Reduction,” *Science*, vol. 290, no. 1, pp. 2319–2323, Dec. 2000.

[123] S. Kirkpatrick, C. D. Gelatt, and M. P. Vecchi, “Optimization by Simulated Annealing,” *International Journal of Applied Earth Observation and Geoinformation*, vol. 220, no. 4598, pp. 671–680, May 1983.

[124] L. Ingber, “Simulated annealing: Practice versus theory,” *Mathematical and Computer Modelling*, vol. 18, no. 11, pp. 29–57, Dec. 1993.

[125] S. Sivanandam and S. Deepa, *Introduction to Genetic Algorithms*, 1st ed. Heidelberg, Berlin: Springer-Verlag, 2008.

[126] K. Shojaee, H. G. Shakouri, and M. B. Taghadosi, *Simulated Annealing, Theory with Applications: Importance of the Initial Conditions and the Time Schedule in the Simulated Annealing*, 1st ed. Croatia: Sciyo, 2010.

[127] R. Pelich, N. Longepe, G. Mercier, G. Hajduch, and R. Garello, “Performance Evaluation of Sentinel-1 Data in SAR Ship Detection,” in *IEEE International Geoscience and Remote Sensing Symposium (IGARSS)*, Jul. 2015, pp. 2103–2106.

[128] P. Viola and M. Jones, “Rapid object detection using a boosted cascade of simple features,” in *IEEE Conference on Computer Vision and Pattern Recognition (CVPR)*, Apr. 2001, pp. I–511–I–518 vol.1.

[129] R. Lienhart and J. Maydt, “An extended set of Haar-like features for rapid object detection,” in *IEEE International Conference on Image Processing (ICIP)*, Sep. 2002, pp. I–900–I–903 vol.1.

[130] R. O. Duda, P. E. Hart, and D. G. Stork, *Pattern Classification*, 2nd ed. New York, NY: Wiley-Interscience, 2001.

[131] R. E. Schapire, *Nonlinear Estimation and Classification*, 1st ed. New York, NY: Springer New York, 2003.

[132] H. A. Rowley, S. Baluja, and T. Kanade, “Neural network-based face detection,” *IEEE Transactions on Pattern Analysis and Machine Intelligence*, vol. 20, no. 1, pp. 23–38, Jan. 1998.

[133] D. Small, “Flattening Gamma: Radiometric Terrain Correction for SAR Imagery,” *IEEE Transactions on Geoscience and Remote Sensing*, vol. 49, no. 8, pp. 3081–3093, Aug. 2011.

[134] K. El-Darymli, P. McGuire, E. Gill, D. Power, and C. Moloney, “Understanding the significance of radiometric calibration for synthetic aperture radar imagery,” in *IEEE 27th Canadian Conference on Electrical and Computer Engineering (CCECE)*, Jul. 2014, pp. 104–107.

[135] F. Baselice and G. Ferraioli, “Unsupervised Coastal Line Extraction From SAR Images,” *IEEE Geoscience and Remote Sensing Letters*, vol. 10, no. 6, pp. 1350–1354, Nov. 2013.

[136] M. T. Alonso, C. Lopez-Martinez, J. J. Mallorqui, and P. Salembier, “Edge Enhancement Algorithm Based on the Wavelet Transform for Automatic Edge Detection in SAR Images,” *IEEE Transactions on Geoscience and Remote Sensing*, vol. 49, no. 1, pp. 225–235, Jan. 2011.

[137] Y. LeCun, L. Bottou, Y. Bengio, and P. Haffner, “Gradient-based learning applied to document recognition,” *Proceedings of the IEEE*, vol. 86, no. 11, pp. 2278–2324, Nov. 1998.

[138] A. Krizhevsky, “Learning multiple layers of features from tiny images,” Department of Computer Science, Toronto, Canada, Tech. Rep. Tech. Rep. 001, May 2006.

[139] M. H. Protter and C. B. Morrey, *College calculus with analytic geometry*, 3rd ed. Boston, MA: Addison-Wesley, 1970.

[140] P. Kumar and A. Yildirim, “Minimum-Volume Enclosing Ellipsoids and Core Sets,” *Journal of Optimization Theory and Applications*, vol. 126, no. 1, pp. 1–21, Jul. 2005.

[141] B. Matthews, “Comparison of the predicted and observed secondary structure of T4 phage lysozyme,” *Biochimica et Biophysica Acta (BBA) - Protein Structure*, vol. 405, no. 2, pp. 442–451, Oct. 1975.